
**Thickness retrieval and emissivity modeling
of thin sea ice at L-band for SMOS satellite observations**

Vom Fachbereich für Physik und Elektrotechnik
der Universität Bremen

zur Erlangung des akademischen Grades eines
Doktors der Naturwissenschaften (Dr. rer. nat.)
vorgelegte Dissertation

von
Dipl.-Phys.
Marcus Huntemann

Eingereicht am:

8. September 2015

Tag des Promotionskolloquiums:

18. November 2015

1. Gutachter: Prof. Dr. Justus Notholt
2. Gutachter: Prof. Dr. Peter Lemke

this page intentionally left blank

Abstract

In this study we have developed an empirical retrieval for thickness of young and first-year ice during the freeze up period for the L-band passive microwave radiometer Microwave Imaging Radiometer with Aperture Synthesis (MIRAS) on the Soil Moisture and Ocean Salinity (SMOS) satellite. The retrieval is based on intensity and polarization difference using the incidence angle range of 40° to 50° and is validated using data from airborne EM-Bird, Moderate-resolution Imaging Spectroradiometer (MODIS) thermal imagery, and self consistency checks for ice thicknesses up to 50 cm with an error of 30 % on average. In addition, we modeled the microwave emission for Arctic first-year ice using the sea ice version of the Microwave Emission Model of Layered Snowpacks (MEMLS). The sea ice conditions used as input for MEMLS were generated using a thermodynamic energy balance model (based on the Crocus model) driven by reanalysis data from European Centre for Medium-Range Weather Forecasts (ECMWF). From unexpected features in the modeled microwave emission and disagreements with the empirically trained SMOS retrieval several shortcomings of the energy balance model and MEMLS were identified and corrected. The corrections include a treatment of mismatch of layer definition between the energy balance model and MEMLS, an adaptation of the reflection coefficient for lossy media in MEMLS, and several smaller corrections. For comparison, two simple models ignoring volume scattering, one incoherent and one coherent, were set up and were found to be able to reproduce the results of the more complex MEMLS model on average. With the simple models, the effects of thin coherent layers, the snow cover, the interface roughness and three different dielectric mixture models for sea ice were explored. It was found that the choice of the mixture model is essential for the relation of sea ice thickness to brightness temperatures in L-band, suggesting sea ice thickness sensitivities from few centimeters to several meters for salinity conditions of the global oceans. The interface properties, especially at the sea ice bottom, were found to be a major uncertainty source when modeling the microwave emission of thin sea ice. In addition, the variability in snow depth, the interface roughness, and the ice surface salinity and temperature were found to have a similar influence on the resulting brightness temperatures, with a strong effect on horizontally (up to 30 K) and weak effect on vertically polarized radiation (up to 10 K) for temperatures below 260 K. A model for simulating coherent microwave emission for thickness distributions of ice and snow was prepared to overcome weaknesses from the single thickness coherent and incoherent models. Comparison to the incoherent model showed that for realistic snow depth distributions obtained from Operation IceBridge (OIB) coherence effects can change the brightness temperatures on the scale of a SMOS footprint up to 10 K in horizontal polarization. These findings suggest that the retrieval for the thickness of thin sea ice with satellite based L-band sensors yield higher uncertainties than expected from earlier studies.

Contents

Abstract	i
1 Introduction and motivation	1
2 Fundamentals	5
2.1 Radiative transfer and microwave emission of sea ice	5
2.2 Sea ice properties and empirical formulations	8
2.2.1 Ice growth and ice thickness	8
2.2.2 Salinity and brine inclusions	9
2.2.3 Ice temperatures in thermodynamic equilibrium	10
2.2.4 Dielectric constant and refractive index	10
2.3 The SMOS mission and data products	15
2.3.1 The radiometer MIRAS	15
2.3.2 Coordinate transformation	16
2.3.3 Data quality and external influences	17
2.3.4 Other L-Band radiometers onboard satellites	18
3 Empirical sea ice thickness retrieval	19
3.1 Retrieval development	19
3.1.1 Training data and region	21
3.1.2 Fit functions	23
3.1.3 Uncertainty estimation	27
3.2 Comparison and validation approaches	27
3.2.1 MODIS thermal imagery ice thickness estimates	28
3.2.2 EM-bird airborne measurements	30
3.2.3 Day-to-day differences – plausibility check	31
3.3 A sea ice thickness product	34
3.3.1 Operational implementation and data distribution	34
3.3.2 Users and applications for thin sea ice data	35
3.3.3 Conclusions and remarks	36

4	Emissivity modeling	39
4.1	Ice atmosphere interaction — an energy balance model	39
4.1.1	Initial conditions and assumptions	40
4.1.2	Precipitation and snow cover on sea ice	43
4.1.3	Review of energy contributions	45
4.1.4	Comparison to CFDD based model	46
4.2	Sea ice emissivity from MEMLS	46
4.2.1	Original temperature profile	49
4.2.2	Linearized temperature profile	50
4.2.3	Comparison with empirical retrieval from SMOS	52
4.3	Model modifications	54
4.3.1	Brine salinity	55
4.3.2	Limit of ice thickness during the growth phase	55
4.3.3	Sea water salinity as input parameter	57
4.3.4	Reflectivity of the ice-water interface	57
4.3.5	Influence of maximum layer thickness	58
4.3.6	Correction of dielectric mixture models	61
4.3.7	Handling of thin coherent layers	61
4.4	Sensitivity studies	68
4.4.1	Sensitivity to salinity	69
4.4.2	Sensitivity to snow on sea ice	72
4.4.3	Ice surface temperature and penetration depth	74
4.5	Summary of performed modeling	75
5	Follow-up on data and modeling studies	79
5.1	Techniques for SMOS data representation	79
5.1.1	Binning method	81
5.1.2	Exponential fit function	84
5.1.3	Fresnel fit function	87
5.1.4	Comparison of fit accuracy and data consistency	89
5.1.5	Fit performance in RFI conditions	94
5.1.6	Physical discussion of the multilayer Fresnel fit	95
5.2	Revision of modeling	101
5.2.1	Radiation within the ice (incoherent model)	103
5.2.2	Interface roughness effects	108
5.2.3	Origin of polarization effects	111
5.2.4	Layer thickness for an incoherent radiation model	114
5.2.5	Coherence effects and thickness modes	115
5.2.6	An ensemble emission model	118

5.2.7	MEMLS versus simple models	125
6	Conclusions	127
A	Appendix	135
A.1	Dielectric constant of brine	135
A.2	Collection of dielectric mixture models	136
A.2.1	Random needle inclusions	137
A.2.2	Spherical inclusions	137
A.2.3	Vertically oriented needle inclusions	137
A.3	Empirical model for dielectric constant of sea ice after Vant	137
A.4	Dielectric constant of snow	138
A.5	Tables for empirical formulas	138
	List of acronyms	141
	Bibliography	145

1 | Introduction and motivation

Sea ice is an essential climate component and observations of its formation, evolution, and decay are important for understanding and predicting climate change [Stocker et al., 2013]. In particular, the sensitive interplay of the albedo feedback and the thermal insulating effects is balancing and stabilizing the Arctic and Antarctic ecosystem in a yearly cycle. Thus, the observations of sea ice is of major interest for climate modeling and prediction and can be achieved using a variety of satellite remote sensing techniques.

Sea ice coverage has been observed since 1972 using several microwave radiometers, namely the Electrically Scanning Microwave Radiometer (ESMR) (1972-1977), Scanning Multi-channel Microwave Radiometer (SMMR) (1978-1987), Special Sensor Microwave Imager (SSM/I) (1987-present), Advanced Microwave Scanning Radiometer - Earth Observing System (EOS) (AMSR-E) (2002-2012) and Advanced Microwave Scanning Radiometer 2 (AMSR2) (2012-present). Passive microwave observations of sea ice work in cloudy conditions providing a daily coverage of the Arctic and Antarctic region and are therefore well suited for operational monitoring of sea ice.

For sea ice thickness, many satellite-based remote sensing techniques were employed. Methods for active instruments, like radar and laser altimeters use the sea ice free board for ice thickness estimation. They commonly provide monthly coverage of the Arctic and Antarctic areas and have higher accuracy in the regime of thick ice >1 m [Kwok and Cunningham, 2008, Laxon et al., 2013]. Observations in the near infrared work in cloud free areas providing high spatial resolutions of about 1 km. Near infrared observations are suitable for retrieving thickness of thin sea ice less than 1 m relying on a heat balance equation [Yu and Rothrock, 1996, Mäkynen et al., 2013]. Also, the satellite-based passive microwave observations turned out to carry information on ice thickness of thin sea ice

[Martin, 2005, Tamura et al., 2007].

The microwave emissivity of sea ice has been narrowed down to a few essential physical properties like sea ice thickness, salinity, temperature, snow depth, grain size, and density. However, the importance of each quantity is varying with the wavelength within the microwave regime [Tonboe et al., 2011, Fuhrhop et al., 1998].

Since 2009 the European Space Agency (ESA) Soil Moisture and Ocean Salinity (SMOS) mission has been observing the Earth at 1.4 GHz (L-band) from a sun synchronous dusk-dawn orbit [Kerr et al., 2001]. At this low microwave frequency, the emission is sensitive to ice thickness changes up to 50 cm and even more at ice of less saline waters like the Baltic Sea [Kaleschke et al., 2010]. Several approaches have been made in order to model the SMOS brightness temperatures over sea ice using a broad diversity of thermodynamic and microwave emission models [Heygster et al., 2009, Kaleschke et al., 2013]. With more SMOS data available, more possibilities for validation and empirical training came up. Two algorithms for retrieval of sea ice thickness of thin sea ice during the Arctic freeze up, were initially developed independently in the University of Hamburg and the University of Bremen using disjunct data from the SMOS from different observation angle regimes [Kaleschke et al., 2012, Tian-Kunze et al., 2014, Huntemann et al., 2014]. In addition to sea ice thickness, other potentials of SMOS data have been investigated like sea ice concentration [Mills and Heygster, 2011a] and snow thickness on multiyear ice [Maaß et al., 2013, 2015a].

The objective of this work is twofold; firstly, to develop and validate an empirical sea ice thickness retrieval for the SMOS satellite. Secondly, to model the emissivity of first-year ice and its snow cover for comparison to the empirical retrieval to understand the relevant physical processes.

This document is outlined as follows.

In Chapter 2 we introduce the radiative transfer in sea ice and the basic physical sea ice properties relevant for microwave remote sensing. Additionally, different dielectric mixture models for brine inclusions of sea ice are presented and a brief introduction to the SMOS mission and corresponding data is given.

Chapter 3 introduces an empirically trained retrieval based on SMOS data in the incidence angle range of 40° to 50° . Also, several comparisons and consistency checks are performed to validate the sea ice thickness retrieval.

Chapter 4 will introduce a chain of atmospheric, thermodynamic and microwave emission models. This model chain is used to simulate a large amount of sea ice profiles and properties for connection to characteristic microwave signatures of first year ice in L-band. In addition, several modifications made to the thermodynamic and microwave emission model are described in detail and finally the modeled results for various environmental

conditions are compared to the empirical retrieval from SMOS.

In Chapter 5 we introduce three different approaches for a more compact representation of SMOS data for sea ice applications using the relation between brightness temperatures and incidence angle. One approach, a physical fit function based on the Fresnel equations is discussed in more detail. In order to provide a more intuitive access to understanding the microwave emission of sea ice, we discuss incoherent and coherent approaches for the most relevant contributions to the brightness temperatures like the dielectric properties and the small scale roughness of sea ice. Moreover, a combined coherent emission model will be used to estimate the effect of thin layers causing coherence effects with ice thickness and snow thickness distributions on the scale of a SMOS footprint.

The findings are summarized, as well as conclusions and an outlook are given in Chapter 6.

2 | Fundamentals

2.1 Radiative transfer and microwave emission of sea ice

Microwave remote sensing of sea ice is based on its dielectric properties. The concept relies on the Planck function which relates the temperature of a medium to its emitted radiation in an approximately linear way within the microwave regime. As a result of this so called *Rayleigh-Jeans-approximation* the emitted radiation can be described as a brightness temperature

$$T_b(p, f) = e(p, f) \cdot T, \quad (2.1)$$

with the emissivity e , the physical temperature T . The emissivity is still dependent on the frequency f and the polarization p of the radiation. This rather simple concept uses the assumption of an infinite half space of the material, so that T is independent of the depth. This is a typical assumption for microwave remote sensing of sea ice with T as surface temperature.

The intensity of the electromagnetic field of a plane wave at the point z can be written as

$$E(z) = E(0) \cdot \exp(-\gamma z), \quad (2.2)$$

where $\gamma = \alpha + i\beta$ with $\alpha = k_0 \|\Im(\sqrt{\epsilon})\|$ as absorption coefficient and $\beta = k_0 \Re(\sqrt{\epsilon})$ as phase constant. k_0 is the wave vector and ϵ is the complex permittivity. Ignoring scattering, the power density is

$$S(z) = S_0 \exp(-\kappa_\alpha z), \quad (2.3)$$

with the power absorption coefficient $\kappa_\alpha = 2\alpha$. The penetration depth into a medium can then be described as

$$\delta_p = 1/\kappa_\alpha. \quad (2.4)$$

Using *Kirchhoff's law* in thermal equilibrium the same amount of radiation is absorbed as it is emitted. The radiation passing without refraction and without scattering through a single layer at uniform temperature can then be described as

$$T_{b,\text{out}} = T_{b,\text{in}} \exp(-\kappa_\alpha d) + T(1 - \exp(-\kappa_\alpha d)), \quad (2.5)$$

with the layer temperature T , the layer thickness d , and the incoming and outgoing radiation, $T_{b,\text{in}}$ and $T_{b,\text{out}}$. The two terms in Equation (2.5) describe the absorption and emission respectively. The absorption factor $\exp(-2\alpha d)$ is quite intuitive; the thicker the medium and the higher the absorption, the more the entered radiation is extinguished and replaced by the emission of the layer. Once the brightness temperature reaches the physical temperature of the layer, absorption and emission are in equilibrium and the emissivity is $e = 1$ for a medium ignoring refraction. Wave propagation without refraction can be assumed in microwave remote sensing of the atmosphere, when the particle size and atmospheric layer boundaries are small compared to the wavelength. However, in remote sensing of the Earth's surface there is at least one distinct boundary. To describe refraction the complex refractive index N is often used instead of the permittivity, with

$$\sqrt{\epsilon} = \sqrt{\epsilon' + i\epsilon''} = N = n' + in'', \quad (2.6)$$

$$\epsilon' = n'^2 - n''^2, \quad (2.7)$$

$$\epsilon'' = 2n'n''. \quad (2.8)$$

Refraction occurs at the border between two media when their refractive index is not equal. If we consider refraction, the emissivity e of Equation (2.1) is determined by the refractive index of the medium. The reflectivity at the interface between two media is described by the Fresnel equations for non magnetic media [Ulaby et al., 1981]:

$$\begin{aligned} r_h &= \frac{N_2 \cos \theta_1 - N_1 \cos \theta_2}{N_2 \cos \theta_1 + N_1 \cos \theta_2}, \\ r_v &= \frac{N_1 \cos \theta_1 - N_2 \cos \theta_2}{N_1 \cos \theta_1 + N_2 \cos \theta_2}. \end{aligned} \quad (2.9)$$

r_h and r_v are the reflection coefficient at horizontal and vertical polarization, N_1 and N_2 are the complex refractive indices of the two media, and θ_1 and θ_2 are the angles of incoming and outgoing radiation. θ_2 can also be expressed through N_1 , N_2 and θ_1 using Snell-Descartes law.

$$N_1 \sin \theta_1 = N_2 \sin \theta_2 \quad (2.10)$$

as

$$\begin{aligned}
r_h &= \frac{N_2 \cos \theta_1 - N_1 \sqrt{N_2^2 - N_1^2 \sin^2 \theta_1}}{N_2 \cos \theta_1 + N_1 \sqrt{N_2^2 - N_1^2 \sin^2 \theta_1}} \\
r_v &= \frac{N_1 \cos \theta_1 - \sqrt{N_2^2 - N_1^2 \sin^2 \theta_1}}{N_1 \cos \theta_1 + \sqrt{N_2^2 - N_1^2 \sin^2 \theta_1}}
\end{aligned} \tag{2.11}$$

The total reflectivity at the interface between plane parallel media with N_1 and N_2 is

$$R_{p1}(\theta_1, N_1, N_2) = \|r_p(\theta_1, N_1, N_2)\|^2. \tag{2.12}$$

We can use the Fresnel Equations (2.11) with Equation (2.5) to account for refraction at the interfaces:

$$T_{b,p,\text{out}} = T_{b,p,\text{in}} \exp(-\kappa_\alpha d) \cdot (1 - R_{p,\text{bot}}) + T(1 - \exp(-\kappa_\alpha d)) \cdot (1 - R_{p,\text{top}}). \tag{2.13}$$

Here the index p stands for the polarization, either h or v , and bot and top address bottom and top of the layer. Equation (2.13) can be used recursively for multi layer structures like sea ice and snow. In first-year ice at 1.4 GHz, volume scattering can be neglected so that Equation (2.13) can server as appropriate incoherent emission model.

Considering the first order of reflecting terms from each layer, the model is sometimes referred to as the Burke model [Burke et al., 1979]. In a multi layer environment, with increasing numbers of layers the model converges towards a model ignoring reflection effects [Maaß et al., 2013]. This limitation can be surpassed by calculating the reflection effects for layer transitions with strong contrast in dielectric properties while ignoring reflection at low dielectric contrast boundaries. A threshold for the dielectric contrast need to be taken into account may be estimated from Equations (2.11) and transitional layers [Yurchak, 2014]. An adaptation of the problem to our application on sea ice is discussed in Section 5.2.1

Another effect can be seen when more layers are involved in a system is coherence which is more pronounced in low frequencies like 1.4 GHz and might influence the sea ice and snow emission to some extent [Mätzler and Wiesmann, 2012]. In case of two or more plane parallel interfaces an electromagnetic plane wave can interfere with its reflected counterpart. This can be expressed by combination of the reflectivities of the layers according to the invariant embedding method [Adams and Denman Eugene D, 1966, Bellman and

Wing, 1975, Mätzler and Wiesmann, 2012] by:

$$r_{\text{comb},n} = \frac{r_n + r_{\text{comb},n-1} \exp(2iP_n)}{1 + r_n r_{\text{comb},n-1} \exp(2iP_n)}, \quad (2.14)$$

where r_n is the Fresnel reflection coefficient between the layer n and layer $n + 1$ from Equation (2.9), $r_{\text{comb},n-1}$ is the combined reflection coefficient the system of $n - 1$ layers below, so that $r_0 = r_{\text{comb},0}$ and P_j is the one way phase difference through layer j given by

$$P_j = 2\pi d_j N_j \cos \theta_j / \lambda, \quad (2.15)$$

with d as the layer thickness and λ the free space wavelength.

Equation (2.14) is recursive and can be applied to any combination water, sea ice, and snow layers to obtain the coherent reflection coefficient of the layer combination. The combined layer power reflectivity is determined by Equation (2.12). This however is not directly an emission model as the emission of each individual layer remains unconsidered. For a simple two interface variant of Equation (2.14) with water, sea ice, and air, an approach by Menashi et al. [1993] is using the average temperature of air and water.

2.2 Sea ice properties and empirical formulations

Sea ice is a quite complex material with many features differing considerably from lake ice due to its composition. It contains a high amount of salt which causes a different formation and aging process compared to lake ice. The differences include a lower freezing temperature of sea ice of about -1.8°C . To model the physical properties of sea ice important to the emissivity several, in part empirical, models have been developed over the years. In this section we will discuss the most important ones for our application. This includes ice thickness, profiles of ice temperature, ice salinity and ice density for growing first year ice. From these quantities the dielectric properties of sea ice can be calculated using mixture models to combine the dielectric properties of the liquid brine inclusions and the solid ice.

2.2.1 Ice growth and ice thickness

An empirical formulation to model the sea ice thickness is using the Cumulative Freezing Degree days (CFDD)[Bilello, 1961, Weeks, 2010, p. 35-39]

$$d_{\text{ice}}[\text{cm}] = 1.33 \cdot (\Theta[^\circ\text{C}])^{0.58} \quad (2.16)$$

where Θ is the daily average temperature difference with respect to the sea water freezing point of -1.8°C and d_{ice} is the ice thickness. Equation (2.16) is a simplification of the more complex heat balance equation [Leppäranta, 1993] with a snow thickness of about

$d_{\text{snow}} = 0.08 \cdot d_{\text{ice}}$. The CFDD ice growth model agrees well with recent measurement of ice thickness at Barrow, Alaska [Petrich and Eicken, 2010]. To increase the temporal resolution and have an idea of the early thin ice stages, a shorter time interval may be used.

2.2.2 Salinity and brine inclusions

One of the major difference of sea ice to lake is its salinity which decreases its freezing temperature from 0°C to about -1.8°C . During the freezing the salt gets rejected from the ice and partly collects in small brine pockets. This brine is more saline than the sea water and stays liquid also at much lower temperatures. During the ice growth phase, the salt entrapped within the ice is a quite stable function of the ice growth. It can be described quantitatively according to Nakawo and Sinha [1981] by

$$S_i = \frac{0.12 \cdot S_w}{0.12 + 0.88 \cdot \exp(-4.2 \cdot 10^4 \cdot v)}, \quad (2.17)$$

with S_w the salinity of the sea water and v the growth rate in cm per day. This formulation is well suited in combination with Equation (2.16) for generating salinity profiles of sea ice. Particularly important for microwave emission is the volume fraction of the brine within the sea ice as the liquid phase presents a strong dielectric contrast with respect to the solid ice. As the brine consists of different chemical compounds, the precipitation of solid salts cannot be described by a simple polynomial function of the temperature because it has steps [Assur, 1960]. Cox and Weeks [1983] propose an empirical function for the brine volume fraction as

$$\frac{V_b}{V} = \left(1 - \frac{V_a}{V}\right) \frac{\rho_i S_{si}}{F_1(T) - (\rho_i) S_{si} F_2(T)}, \quad (2.18)$$

where the density of pure ice $\rho_i = 0.917 - 0.1404 \cdot 10^{-3}T$ in g m^{-3} , T in $^\circ\text{C}$, $F_i(T) = a_i + b_i T + c_i T^2 + d_i T^3$. The coefficients a , b , c , and d based on the phase relations are listed in the appendix in Table A.1 [Cox and Weeks, 1983, Leppäranta and Manninen, 1988]. Another important quantity is the salinity of the brine which is higher the colder the ice, so that in empirical formulations it is often described as a polynomial function of temperature [Assur, 1960]

$$S_b = a + bT + cT^2 + dT^3, \quad (2.19)$$

with T as the temperature and a, b, c and d as temperature dependent coefficients which are listed in the appendix in Table A.2.

2.2.3 Ice temperatures in thermodynamic equilibrium

The temperature profile within the ice is of major importance for emission modeling as the dielectric constant of the ice depends on temperature. A thermodynamic equilibrium solution for the ice surface temperature was used by Maaß et al. [2013], Tian-Kunze et al. [2014] with the assumption of a linear temperature profile through the ice and snow layer as

$$T_{\text{ice/snow}} = \frac{(T_{\text{air}} - T_{\text{water}}) \cdot \lambda_{\text{snow}} \cdot d_{\text{ice}}}{\lambda_{\text{ice}} \cdot d_{\text{snow}} + \lambda_{\text{snow}} \cdot d_{\text{ice}}}, \quad (2.20)$$

with λ as the thermal conductivity of the layer. Even though there are simple empirical expressions for the thermal conductivity of snow and sea ice [Petrich and Eicken, 2010], for above approximation of thermal equilibrium fixed values are suitable. For snow and ice λ is approximately $\lambda_{\text{ice}} = 2.1 \text{ W K}^{-1} \text{ m}^{-1}$ and $\lambda_{\text{snow}} = 0.31 \text{ W K}^{-1} \text{ m}^{-1}$ [Maaß et al., 2013, Petrich and Eicken, 2010, Yu and Rothrock, 1996]. More accurate formulations depend on the density of snow and ice and parameterizations are summarized by [Petrich and Eicken, 2010]

2.2.4 Dielectric constant and refractive index

Vant et al. [1978] concluded the connection between the brine volume fraction and the complex dielectric constant as an empirical linear relationship. This makes the dielectric constant dependent on temperature and salinity of the sea ice only, which simplifies the modeling of the microwave emission of sea ice.

Other studies take a more general approach and assume sea ice as a mixture of two different dielectric materials, namely ice and brine, and use a dielectric mixture model to calculate the dielectric constant of this mixture. The result then is very sensitive to the shape and orientation of the brine inclusion of the mixture [Mills and Heygster, 2011b, Shokr, 1998, Winebrenner et al., 1992]. This more general approach allows also to predict the dielectric constant for very saline ice and warmer temperatures.

A good approximation of the shape and orientation of the brine inclusions within the sea ice is not evident for first year ice. If the ice has been formed under rough conditions, the brine inclusions may have no preferred orientation and can be approximated as randomly oriented needles [Shokr, 1998]. In calm conditions without much temperature variations, the brine inclusions can take spherical shape or can deposit as vertical oriented needles or ellipsoids [Shokr, 1998, Vant et al., 1978]. Also, combination of several types can occur and the behavior can vary with depth in which the ice grows. However, even ice formed at deeper layers may have random oriented inclusions typically found in frazil ice [Shokr, 1998].

To employ a mixture model for the dielectric constant of sea ice, the dielectric constant of the inclusion and the host material must be known. We here use the dielectric constant of brine calculated from Stogryn and Desargant [1985] which is based on the Debye re-

relaxation of the brine solution, the brine volume (Equation (2.18)) and the brine salinity (Equation (2.19)). The dielectric constant of ice depends only on temperature and frequency [Mätzler, 2006]. The formulas for the calculation of the dielectric constant of brine are given in Appendix A. Throughout this document we use more the refractive indices rather than the dielectric constant to describe the dielectric properties. This is due to practical reasons as the absorption term of the radiative transfer Equation (2.13) depends on $\Im(\sqrt{\epsilon}) = \Im(N) = n''$ while, the wavelength in the medium and thus refraction depends on $\Re(\sqrt{\epsilon}) = \Re(N) = n'$.

The dielectric properties of sea ice varies mostly with temperature T and salinity S , so that we can illustrate and discuss this dependence for different dielectric models. The refractive indices for frazil first year ice, with brine inclusions modeled as random needles from [Shokr, 1998, Polder and van Santeen, 1946] are shown in Figure 2.1. For $S = 0$ ppt the real part (plot a) converges to the refractive index of pure ice which dependence on T is weak and $N_{\text{pice}} \approx 1.78$ [Mätzler and Wegmüller, 1987]. The brine inclusions cause an increase of the refractive index over 3.0 for high temperatures and high salinities. Higher salinity induces a higher temperature dependence in addition as the brine volume fraction changes with T . A similar dependence is seen in the imaginary part of the refractive index (Figure 2.1 b). For the mathematical description of the frazil ice dielectric model see Appendix A.2.1.

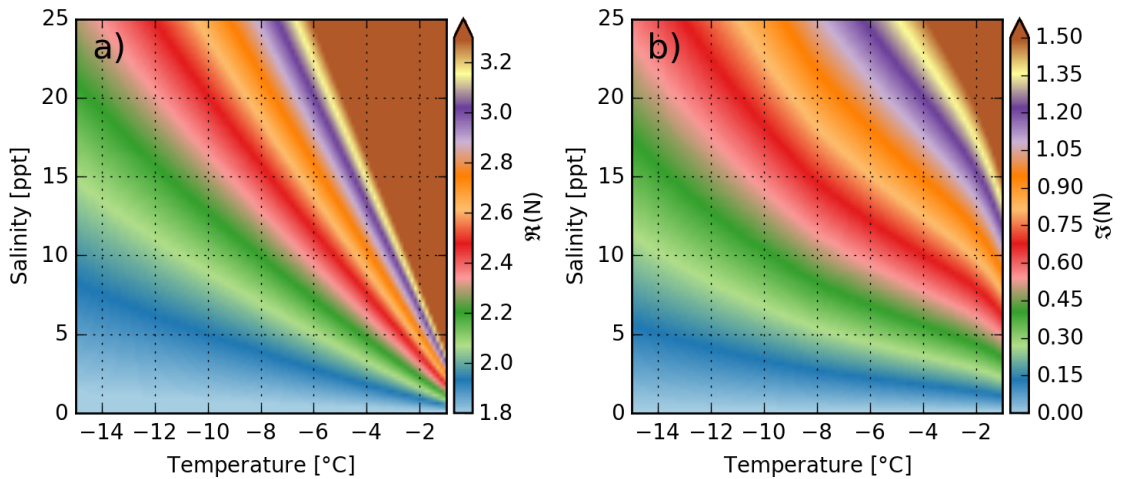


Figure 2.1: Real (a) and imaginary part (b) of the refractive index of first year frazil ice with random needle brine inclusions after [Shokr, 1998] calculated for 1.4 GHz.

Another mixing model assuming spherical shape of the brine inclusion is discussed in Shokr [1998] and Polder and van Santeen [1946]. As the spherical shape of the brine inclusions is more likely to occur in calm conditions [Shokr, 1998] we will refer to this model as the columnar ice model even though the brine inclusions are not oriented. The real and

imaginary part of the refractive index is shown in Figure 2.2 (a) and (b) respectively. The real part of the refractive index is slightly lower compared to the frazil ice model in Figure 2.1 while the imaginary part is much lower by factor of about 6 especially for typical salinity values within sea ice of around $S = 5$ ppt along the temperature axis. The mathematical formulation of the columnar ice dielectric model is given in Appendix A.2.2

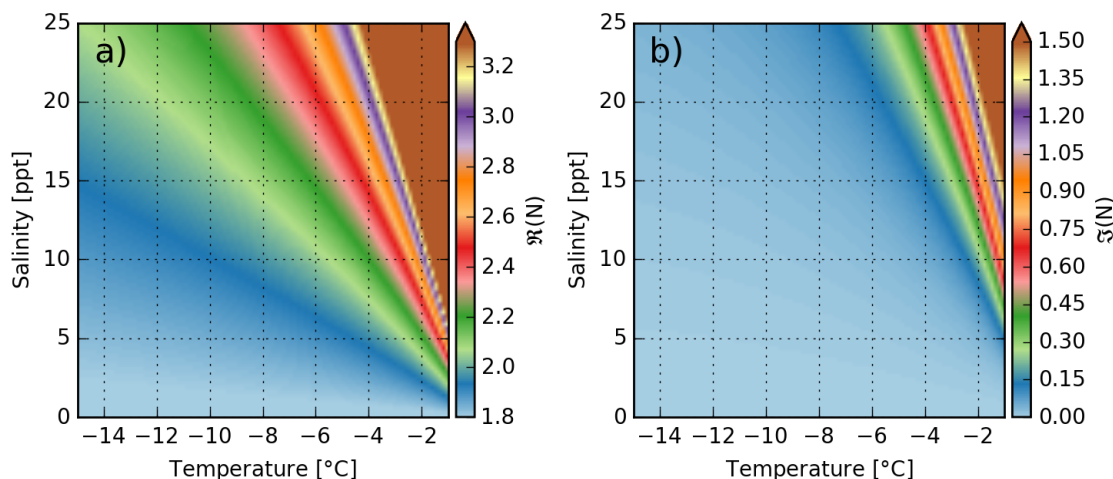


Figure 2.2: Real (a) and imaginary part (b) of the refractive index of first year columnar ice with spherical brine inclusions after [Shokr, 1998] calculated for 1.4 GHz.

Finally, we discuss an empirical model from Vant et al. [1978]. The coefficients fitted by Vant et al. [1978] are adapted to 1.4 GHz by interpolation between 1 GHz and 2 GHz as done in previous studies [Kaleschke et al., 2013]. For both, first-year and multiyear ice, the resulting formulation and coefficients for L-band are given in Appendix A.3. The temperature and salinity dependence of the refractive index using the empirical Vant dielectric model is shown in Figure 2.3. The real part is consistently lower than in the frazil or columnar ice model while the imaginary part is higher than in the columnar ice model but much lower than in the frazil ice model. This model is a linear fit to the brine volume fraction for a limited amount of measurements mostly with relatively low salinity, i.e., low brine volume fraction ($\frac{V_b}{V} < 0.07$). Thus, it is questionable if for higher salinities and temperatures the linear relation to the brine volume fraction is still applicable [Vant et al., 1978, Kaleschke et al., 2013]. However, the Vant dielectric model is widely used in L-band modeling activities [Maaß et al., 2013, Tian-Kunze et al., 2014, Maaß et al., 2015a,b].

For the refractive index of dry snow we use an empirical relation used by Matzler [1996] based on work of Looyenga [1965] and Polder and van Santeen [1946]. The underlying formulas are given in Appendix A.4. We show the real and imaginary part and their dependence on snow density and temperature in Figure 2.4. The real part entirely depends on the density and spans the range $1.05 < \Re(N_{snow}) < 1.5$. The direct rela-

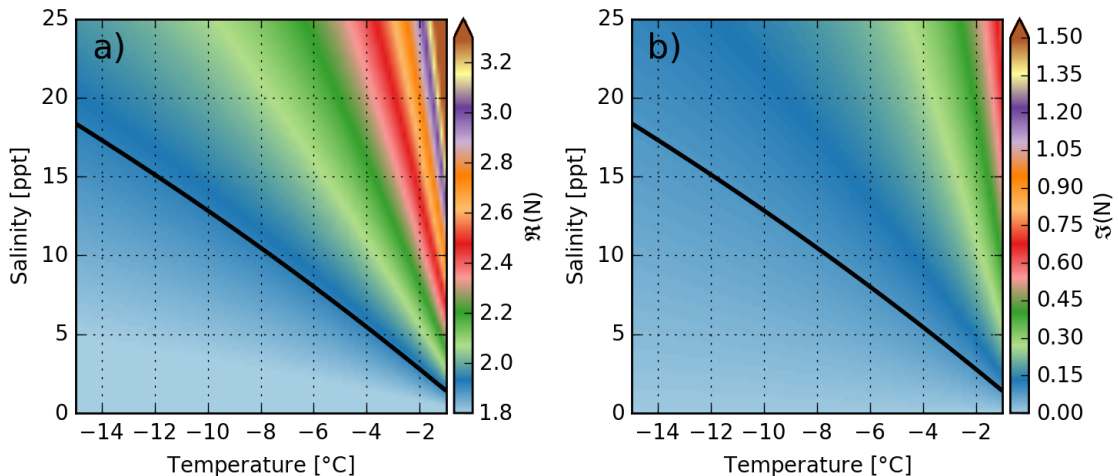


Figure 2.3: Real (a) and imaginary part (b) of the refractive index of first year ice according to the dielectric model of Vant et al. [1978] calculated for 1.4 GHz. The model is supposed to be valid for temperatures and salinities below the black line.

tion of snow density to its dielectric constant is also used to retrieve snow density with Advanced Synthetic Aperture Radar (ASAR) and is proposed for usage within the ESA Sentinel 3 mission [Singh and Venkataraman, 2009, Knudsen et al., 2013]. Recently also a retrieval for snow density and soils dielectric properties for SMOS using the L-band Microwave Emission of the Biosphere (L-MEB) model in combination with the Microwave Emission Model of Layered Snowpacks (MEMLS) was introduced Wigneron et al. [2007], Schwank et al. [2015]. In Section 5.1.3 we employ a similar approach as an attempt to retrieve the dielectric properties of snow and sea ice. A typical value for snow density in the Arctic and Antarctic is 0.32 g cm^{-2} [Massom et al., 2001, Warren and Rigor, 1999] leading to $N_{snow} = 1.25$. This density for snow is also used for a snow thickness retrieval on multi-year ice by Maaß et al. [2013, 2015a]. The imaginary part of the refractive index (b) (modeled after [Tiuri et al., 1984]) is highest for high temperature and high densities. However, it is 5 orders of magnitude smaller than the imaginary part of the frazil first-year ice. For our investigation it is therefore also sufficient to neglect the imaginary part of the refractive index of dry snow. In the freeze up period we do not expect to deal with wet snow. However, simple empirical models for a liquid water fraction of snow exist [Tiuri et al., 1984]. With the assumption of dry snow, potential capillary effect leading to brine uptake from the sea ice into the snow, cannot be modeled. To account for this effect appropriately, firstly a model for desalination of sea ice surface due to brine uptake by the snow and, secondly, an appropriate mixture model for calculating the dielectric constant of this mixture, is required. The latter is investigated by Drinkwater and Crocker [1988], modeling the brine uptake by the snow as oblate spheroids after [Denoth, 1980] using a mixture formula from [Polder and van Santeen, 1946]. However, we did not find any em-

pirical formula for the amount of brine soaked into the snow, so that this effect remains unconsidered for this study.

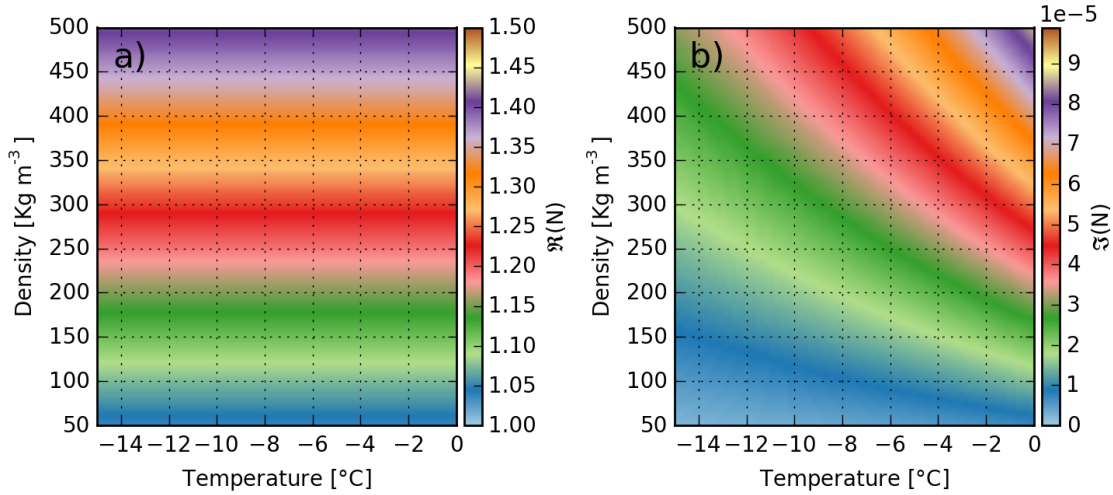


Figure 2.4: Real (a) and imaginary part (b) of the refractive index of dry snow after Matzler [1996], calculated for 1.4 GHz.

Comparing the three dielectric models for first-year ice, the random needles frazil ice model [Shokr, 1998] yields in general higher refractive indices than the other models with spherical brine inclusions or the empirical model by Vant et al. [1978]. It shows 4-6 times higher imaginary part for common temperature and salinity conditions and also the real part show higher values for high salinity and high temperature values than the empirical fit used by Vant et al. [1978]. The sea ice density variation of first year ice contributes little to the refractive index and is often assumed to be constant [Kaleschke et al., 2013, Tonboe et al., 2011].

There is a wide range of different shapes and variation to model the brine inclusions in sea ice which greatly affect the dielectric properties. When the brine inclusions are modeled as oriented structures or the inclusions just have a preferred orientation, then the dielectric constant is incidence angle dependent and thus becomes a tensor [Stogryn, 1987, Shokr, 1998]. In this document we refrain from using a tensorial dielectric constant as it complicates the radiative transfer description [Yeh, 1979, Fleck, Jr. and Feit, 1983, Chang and Shieh, 2001]. This, however, can be worth the effort considering that in-situ methods as cross-borehole DC resistivity tomography nowadays can monitor the evolution of brine orientation within the sea ice [Ingham et al., 2008, Jones et al., 2010, 2012]

The three models shown in Figures 2.1 to 2.3 for first-year sea ice will be used in Section 5.2.1 for comparison within a simple incoherent multilayer microwave emission model based on Equation (2.13).

2.3 The SMOS mission and data products

The Soil Moisture and Ocean Salinity (SMOS) satellite was launched by the European Space Agency (ESA) in 2009 and its only payload MIRAS provides collects data since the beginning of 2010. MIRAS works since mid 2010 in the so called full polarization mode, i.e., it collects the whole stokes vector. In the following subsections we will provide a brief description of the MIRAS radiometer and introduce its application to sea ice related research. The SMOS satellite operates in a sun synchronous orbit at an altitude of 767 km resulting in a 100.0 min period with an inclination of 98.4° . The orbit is a so called dusk-dawn orbit with a local overflight time of 6 am and 6 pm. It provides good coverage due to a wide swath (up to 1400 km) over polar regions without covering the pole directly.

2.3.1 The radiometer MIRAS

The passive microwave instrument Microwave Imaging Radiometer with Aperture Synthesis (MIRAS) is working at 1.4 GHz. At this frequency MIRAS was the first satellite based instrument. MIRAS consists of a three legged star shaped antenna holding 23 smaller antennas each. The principle of MIRAS is that each antenna records the incident radiation at L-Band, a frequency of about 1.4 GHz. From the correlation of the signal of the individual antennas the emission of an area of about $1000 \text{ km} \times 1000 \text{ km}$ is reconstructed in a resolution of $20 \text{ km} \times 30 \text{ km}$ to $90 \text{ km} \times 30 \text{ km}$ depending on the incidence angle. This hexagonal shaped observed area is called a *snapshot* (Figure 2.5) in the SMOS vocabulary and is taken every 1.3 seconds. The snapshot can be divided into different regions with different expected data qualities. The alias free field of view where the best data quality is expected (red in Figure 2.5 a)) and the extended alias free field of view (blue) with slightly degraded data quality. The border of the snapshot and the borders of the unit circles which are part of the image reconstruction procedure [Font et al., 2010] are shown in yellow. For our application we consider data from the entire snapshot as usable.

To be able to be able to collect polarization information, MIRAS switches polarizations of the antennas along each leg every snapshot in a cycle. Therefore, the full stokes vector is not obtained each snapshot but every three snapshots [Martín-Neira et al., 2002]. As the requirements on the data may vary by application, this transformation is not included in the official products but has to be performed by every user according to their needs.

Three Level 1 products from MIRAS are available.

- L1A

The calibrated visibilities, i.e., the correlations of the individual antennas before the reconstruction.

- L1B

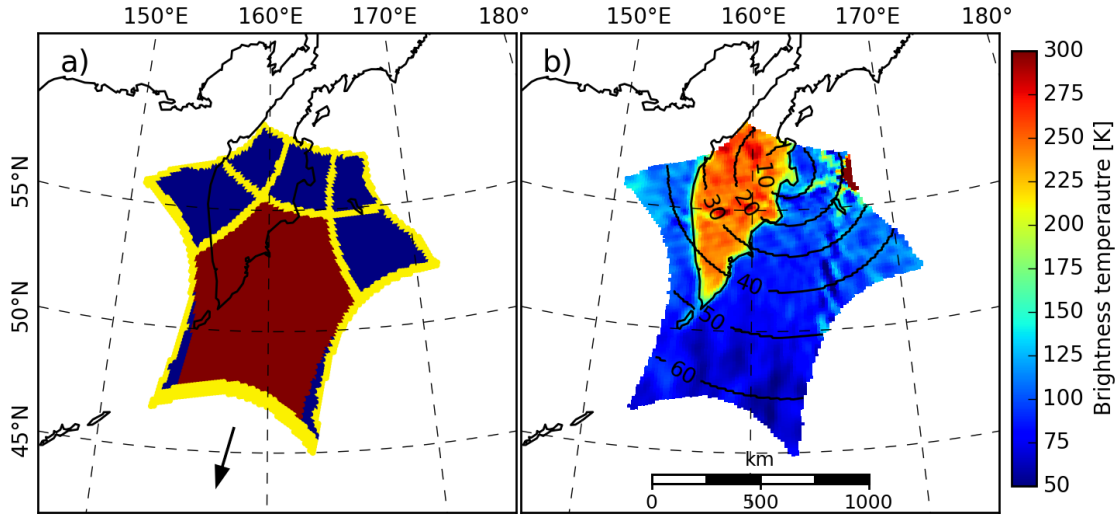


Figure 2.5: A SMOS snapshot of Kamchatka and the Sea of Okhotsk as taken by MIRAS. a) shows the different areas within a snapshot which differ in data quality. The best data quality is expected from the so called *alias free field of view* (red), the dark blue areas show the *extended alias free field of view*, yellow are borders of snapshot and borders of the unit circles. The arrow marks the flight direction. b) shows the brightness temperatures obtained in X-polarization, incidence angles are shown as black contour lines with the numbers in degree.

The Fourier components of the brightness temperatures from the image reconstruction in the antenna reference frame.

- L1C

Brightness temperatures in gridded form in Icosahedron Snyder Equal Area (ISEA) 4h9 grid with 15 km resolution in the antenna reference frame.

In this study we use the SMOS L1C product.

2.3.2 Coordinate transformation

In order to use L1C data product to relate the obtained brightness temperatures to real physical quantities the data have to be converted from the antenna reference frame (X, Y) into the earth surface plane (V, H) by the coordinate transformation in Section 2.3.2.

$$\begin{bmatrix} A_1 \\ A_2 \\ A_3 \\ A_4 \end{bmatrix} = \begin{bmatrix} \cos^2(\alpha) & \sin^2(\alpha) & -\cos(\alpha)\sin(\alpha) & 0 \\ \sin^2(\alpha) & \cos^2(\alpha) & \cos(\alpha)\sin(\alpha) & 0 \\ \sin(2) & -\sin(2) & \cos(2\alpha) & 0 \\ 0 & 0 & 0 & 1 \end{bmatrix} \begin{bmatrix} T_{b,H} \\ T_{b,V} \\ T_{b,3} \\ T_{b,4} \end{bmatrix} \quad (2.21)$$

With $A_1 = \Re(T_{b,XX})$, $A_2 = \Re(T_{b,YY})$, $A_3 = 2\Im(T_{b,XY})$ and $A_4 = -2\Im(T_{b,XY})$ while $\alpha = \alpha_r + \omega_{F_\alpha}$ where ω_r and ω_{F_α} are geometric rotation angle and Faraday rotation angle, respectively [Zine et al., 2008], which are supplied in the SMOS L1C data. $\Re(\dots)$ and $\Im(\dots)$ are the real and imaginary part, respectively.

The transformation needs for each observation in the (V,H) frame brightness temperatures at three polarizations XX , YY and XY . However, only one (either XX or YY) or two of them (either (XX, XY) or (YY, XY)) are measured within one snapshot so that either one or two missing values need to be interpolated.

For the interpolation we use observations from neighboring, overlapping snapshots acquired within 2.5 s before or after the time of interest (SMOS takes snapshots every 1.2 s). Within 2.5 s the atmosphere and surface conditions should change only little. As an additional condition, the incidence angle may only vary less than 0.5° . All observation not fulfilling the interpolation criteria are discarded from further data processing.

2.3.3 Data quality and external influences

Even though anthropogenic emission in the frequency band near 1.4 GHz is prohibited, Radio Frequency Interference (RFI) have been strong during the early phase of the SMOS mission. They have been reduced since then, but not completely eliminated [Camps et al., 2010, Oliva et al., 2012].

The source location of the RFI shows much higher brightness temperatures than occur in nature and may exceed the expected signal by several orders of magnitude in extreme cases. All surface emissions of more than $T_b = 300$ K in the Arctic are unrealistic because they would require an emissivity larger than unity and are considered as RFI. Due to the Fourier transform like reconstruction of each snapshot, a strong RFI from a single source on the Earth surface may influence the obtained brightness temperatures in the entire snapshot (see upper right of the snapshot in Figure 2.5). In order to also discard the RFI influences, in our processing the whole snapshot is discarded if at least one pixel shows a brightness temperature higher than 300 K.

Other more complex filter methods can be applied in order to preserve more data while filtering out unrealistic RFI influenced data [Maaß et al., 2013, Tian-Kunze et al., 2014, Huntemann and Heygster, 2015, Zhao et al., 2015]. Some methods for RFI filtering will be shown later in Section 5.1. Other external influences are also mainly restricted to special cases or have much less influence on the Brightness temperatures [Zine et al., 2008, Maaß et al., 2013], like atmospheric influence, sun glint, influences from ionospheric effects, or solar storms. For our investigation we consider these influences as random errors and do not apply any specific correction.

2.3.4 Other L-Band radiometers onboard satellites

In addition to MIRAS there are other satellite based microwave radiometers operating. From mid 2011 to June 2015 the Satellite de Aplicaciones Cientificas-D (SAC-D) satellite with its payload *Aquarius* was observing at 1.4 GHz. In January 2015, the National Aeronautics and Space Administration (NASA) launched the Soil Moisture Active Passive (SMAP) satellite, also working at 1.4 GHz. In addition to the passive microwave radiometer, SMAP employs an active radar instrument working at slightly lower frequency of 1.2 GHz to 1.3 GHz simultaneously.

3 | Empirical sea ice thickness retrieval

As a first approach to relate brightness temperatures from SMOS to ice thickness it was proposed that the first component of the Stokes vector, the intensity $I = (T_{b,H} + T_{b,V})/2$ at nadir would be most sensitive to sea ice thickness. Ice thickness retrievals were developed using I for the incidence angle range of 0° to 40° where I is nearly constant [Kaleschke et al., 2012, Tian-Kunze et al., 2014]. Here, we will here describe the completely empirical method used by [Huntemann et al., 2014] using the intensity I and the polarization difference $Q = T_{b,V} - T_{b,H}$ at an incidence angle range of 40° to 50° .

3.1 Retrieval development

For development of an empirical retrieval for ice thickness, input, training, and validation data is needed. The input data comes from the SMOS L1C product covering an incidence angle range of 0° to 68° while the widest part of the swath is covered at an incidence angle of about 48° . The dependence of brightness temperatures to the incidence angle is shown in Figure 3.1. Thick sea ice and open water are clearly distinguishable terms of their intensity I . Additionally, on sea ice horizontal and vertical brightness temperatures are closer together than on open water, i.e., the polarization difference Q is smaller.

To train an empirical retrieval we use I and Q at 40° to 50° . The brightness temperatures are averaged for all overflights from an incidence angle of 40° to 50° while all RFI affected snapshot fulfilling above criteria are discarded. The number of data points in this average depends on the time and region and varies from zero to several hundreds.

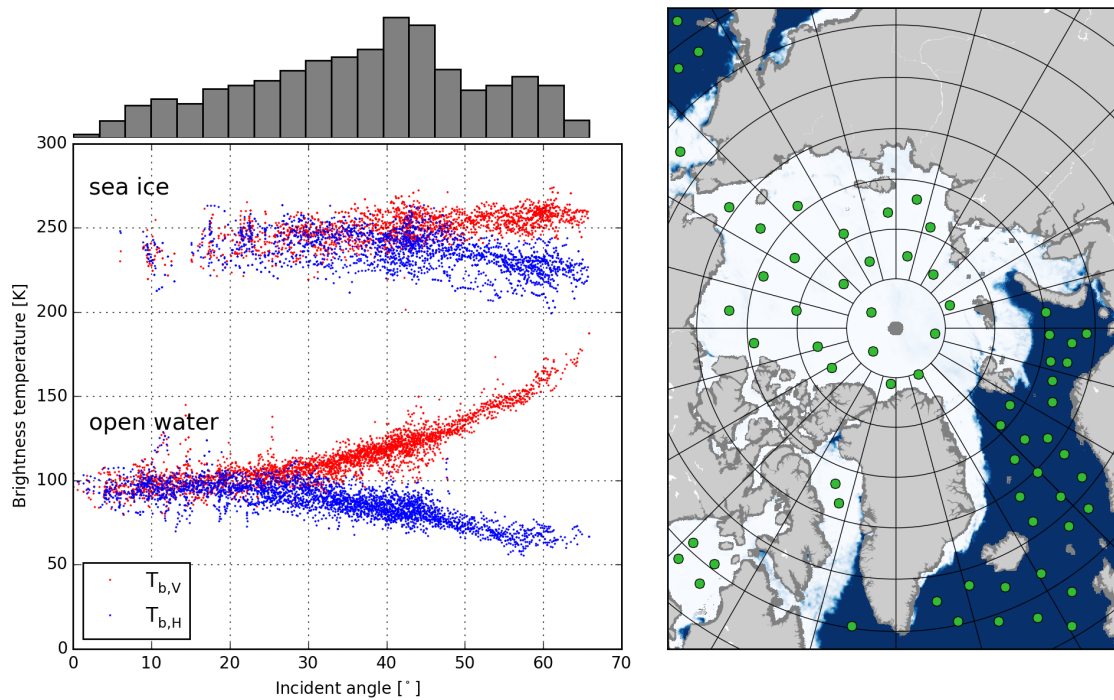


Figure 3.1: Testing large area of brightness temperatures throughout the whole Arctic area from 20 April 2012. Right: ice concentration from SSMIS and test areas for sea ice and open water (green bullets). Left: the corresponding brightness temperature dependence on the incidence angle.

3.1.1 Training data and region

For training of an empirical retrieval, ground truth data is needed. At the time of this analysis, there was no sea ice thickness data of thin sea ice available as acquisition of such data is difficult. During the freeze up, the investigation by ships is restricted as the ice thickness increases very fast. Also in situ measurements on thin are complicated because of the danger of breaking ice cover. We therefore rely on model based ice thicknesses with satellite remote sensing support to determine the initial freeze up. We investigated in the following models

- The one-dimensional HIGH-resolution Thermo-dynamic Snow/Ice model (HIGHTSI) [Launiainen and Cheng, 1998], a regional thermodynamic one dimensional sea ice growth model driven by High Resolution Limited Area Model (HIRLAM), [Källén, 1996, Undén et al., 2002], a short-range weather forecasting system intended to use for limited areas developed by eleven European countries (www.hirlam.org). HIGHTSI was employed to model the freeze up period 2010 in the Barents Sea and Kara Sea.
- Towards an Operational Prediction system for the North Atlantic European coastal Zones (TOPAZ) [Sakov et al., 2012], a coupled global ocean-sea ice data assimilation system which, among other, provides information on sea ice thickness and sea ice concentration. For our analysis we used data from the TOPAZ V3 model.
- National Centers for Environmental Prediction (NCEP) and National Center for Atmospheric Research (NCAR) produce Analysis and Reanalysis data out of observations and historic data, frequently used as reference for global climate variables and for initializing mesoscale atmospheric models. The spatial resolution is 2.5° [Kalnay et al., 1996].

While TOPAZ and HIGHTSI contain the Sea Ice Thickness (SIT) directly, NCEP air temperatures has been used to model the ice thickness using the empirical CFDD model from Equation (2.16). Because of the limited region covered by HIGHTSI, we chose 10 grid cells in the Kara and Barents sea shown in Figure 3.2, in the Arctic freeze up period from 1 October to 26 December 2010.

In this region the sea ice drift is of the order of 8 km/d on average, according to the low resolution ice drift product of the Ocean and Sea Ice Satellite Application Facility (OSI-SAF) [Lavergne et al., 2010]. This is about a half of the size of the 15 km grid cell used here, so that the influence of sea ice drift from one day to the next may be neglected. Therefore, 1D-models like HIGHTSI or the CFDD can be applied without introducing too large errors from the 1D assumption. However, the data cannot be taken blindly as in the worst case a thick ice cover can move into a grid cell within 2 days from previously open

water while thermodynamic ice growth would have needed more than a month to form an ice cover of similar thickness.

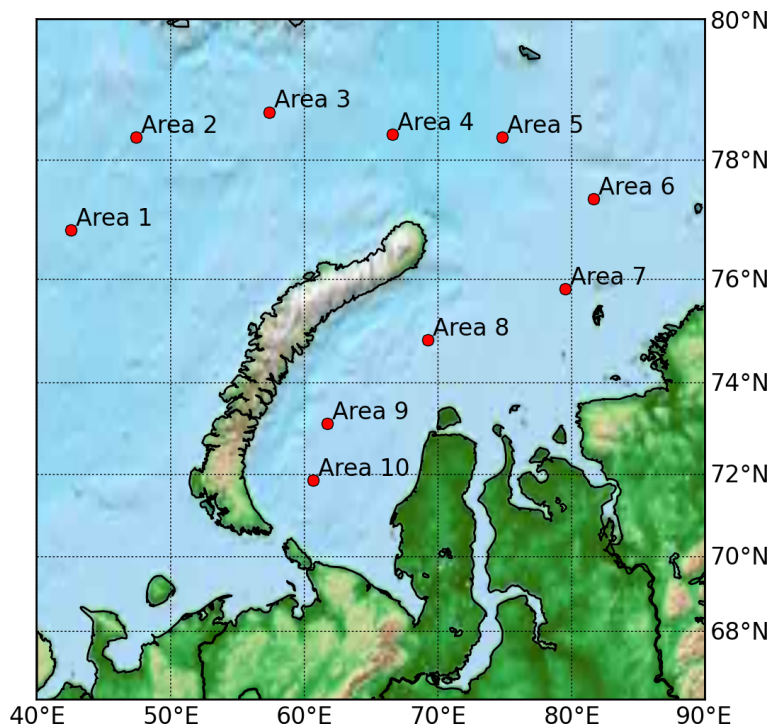


Figure 3.2: Location of the 10 training areas in the Kara and Barents Seas.

The training areas are in a sufficient distance from each other so that the CFDD based SITs are not obtained from the same grid cell of the coarse NCEP grid.

These regions yield high ice concentrations according to sea ice concentration data from AMSR-E and SSMIS sea ice concentrations as retrieved with the Arctic Radiation and Turbulence Interaction Study (ARTIST) Sea Ice (ASI) algorithm [Spren et al., 2008].

For areas 3, 6, and 7 of Figure 3.2 the ice thicknesses from HIGHTSI, TOPAZ and from the CFDDs based on NCEP air temperatures were analyzed as function of SMOS brightness temperatures from in the incidence angle range of 40° to 50° . In several of the regions, SIT did not increase monotonically as Sea Ice Concentration (SIC) reduced over longer periods or freeze up was late in the investigation period. As a result, only Areas 3, 6 and 7 show monotonic freeze up periods sufficiently contiguous for our analysis. Figure 3.3 shows the NCEP air temperatures and the SIC from the ASI algorithm using AMSR-E [Spren et al., 2008] together with different modeled ice thicknesses and the SMOS $T_{b,H}$, $T_{b,V}$ and Q for these areas. The only ice thickness which can reduce during the freeze up period is the one based on the TOPAZ model since it includes drift and melt. HIGHTSI also models ice and snow melting if the temperature goes above zero. The major difference to TOPAZ is that HIGHTSI does not include ice growth due to drift and deformation. In

general, HIGHTSI predicts thickness of undeformed level ice with 100 % SIC. Naturally CFDD does not include ice melting.

Figure 3.3 reveals a high correlation of the SMOS brightness temperatures $T_{b,H}$ and $T_{b,V}$ with the SIT from the models up to about 30 cm to 40 cm thickness. Moreover, $T_{b,H}$ and $T_{b,V}$ are getting closer to each other with increasing ice thickness (decreasing Q). The brightness temperatures are not only influenced by the SIT but also by the SIC. In the current SIT retrieval approach, the SIC is assumed to be equal to 100 %. However, if we restrict the SIC in the training data set to 100 % SIC, we risk to miss the formation of very thin sea ice because SIC retrievals from current passive microwave algorithms yield ice concentrations below 100 % in case of a thin ice cover [Heygster et al., 2014, Kwok et al., 2007, Kern et al., 2007]. In order not to miss these initial ice thicknesses, we include observations with the initial increase of ice concentration from 0 % to 100 % into the training data set while later drops in SIC, possibly ice breakups, are excluded. These excluded regions are shaded gray in Figure 3.3.

As ice forms, an anti-correlation of temperature to the brightness temperatures is seen in the SMOS data which is expected as the ice growth up to the saturation of brightness temperatures. Beyond that point, air temperature and brightness temperatures are expected to be more positively correlated even though no direct relation to the brightness temperatures can be seen. In Area 3 (day 67), Area 6 (day 37) and Area 7 (days 60 and 73) an increase in temperature is connected with a drop of SIC to about 90 %. Overall the temperatures are relatively stable around -20°C without any melt events in these three regions. TOPAZ shows considerably lower SIT in Area 3 than the other non-dynamic models. However, we tend to trust the HIGHTSI and NCEP based thicknesses as the temperature is almost all the time below -20°C where a steady ice thickness growth is expected.

3.1.2 Fit functions

Between the $I = (T_{b,H} + T_{b,V})/2$ and $Q = T_{b,V} - T_{b,H}$ parameters and SIT obtained from the models for each of the different training areas the following functions are fitted:

$$I_{abc}(x) = a - (a - b) \cdot \exp(-x/c) \quad (3.1)$$

$$Q_{abcd}(x) = (a - b) \cdot \exp(-(x/c)^d) + b \quad (3.2)$$

Equation (3.1) is also used by Kaleschke et al. [2012] and is basically the Lambert-Beer law. Equation (3.2) was chosen empirically since it allows representing the shape of thickness dependence of the polarization difference appropriately.

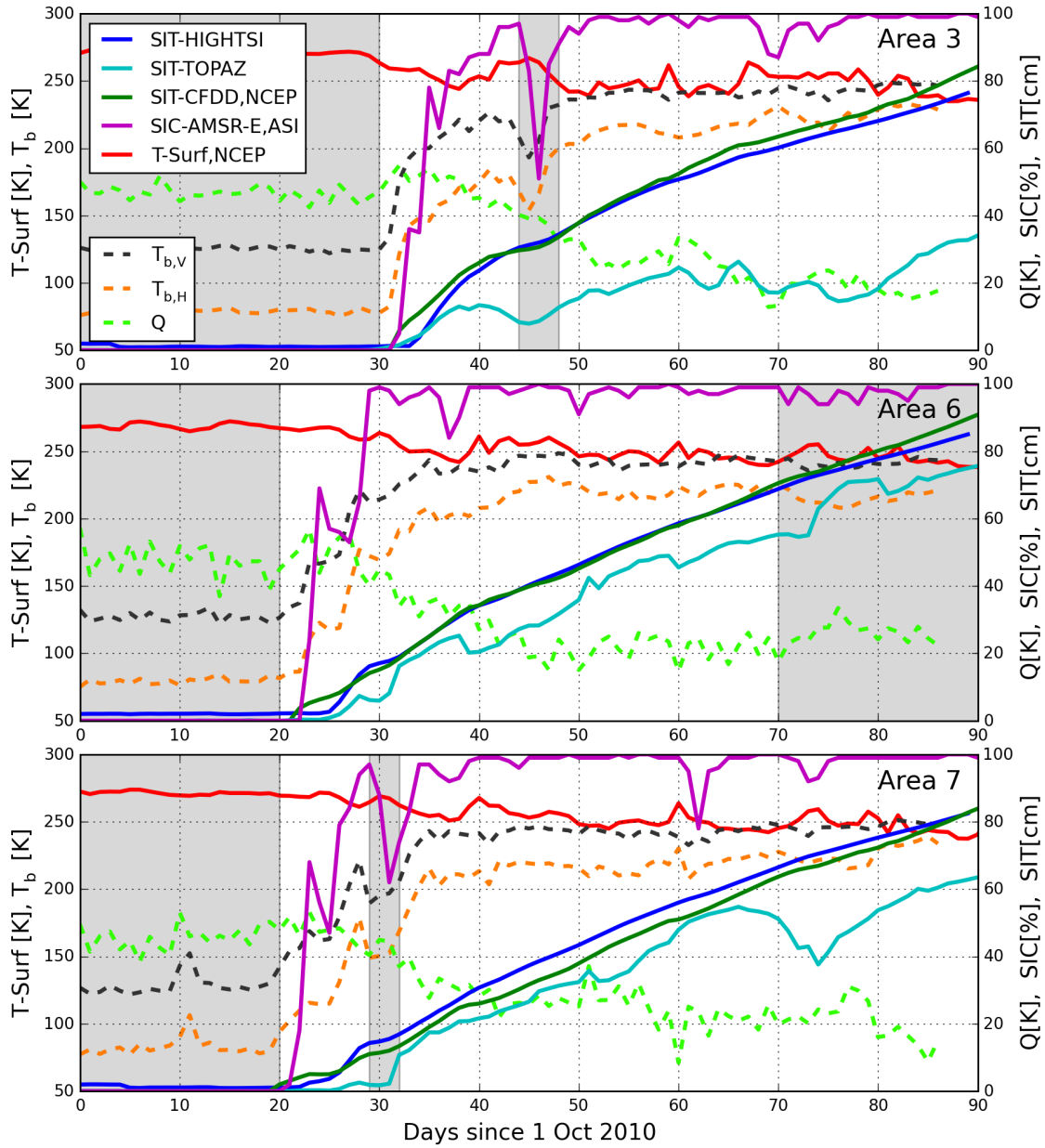
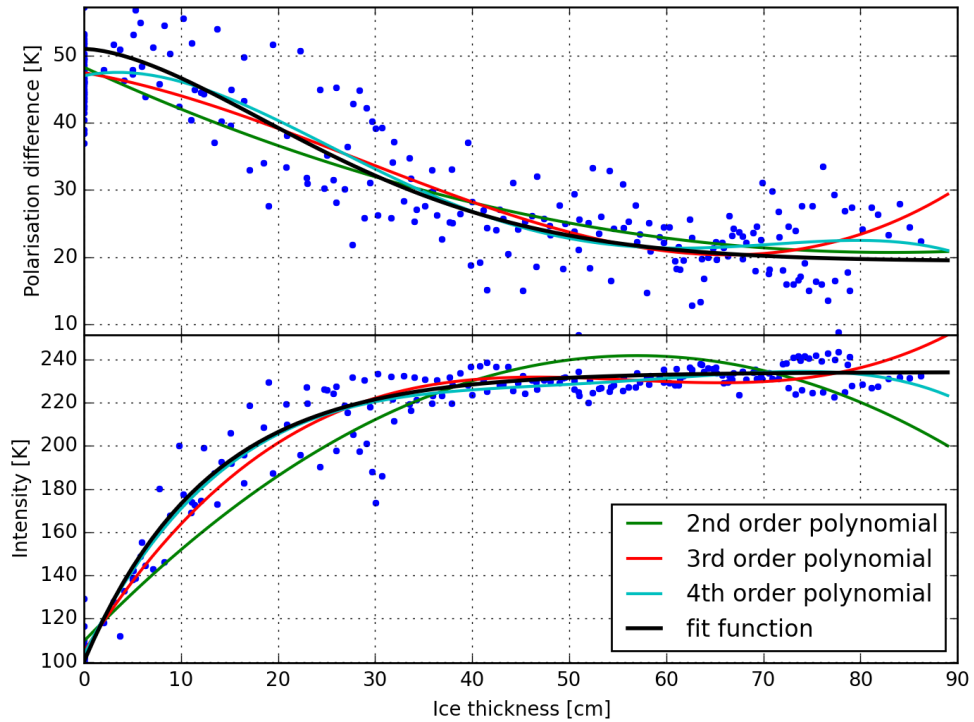


Figure 3.3: Sea Ice Thickness (SIT) of training Areas 3, 6 and 7 (for location see Figure 3.2) from TOPAZ, HIGHTSI and NCEP, air temperature from NCEP, Sea Ice Concentration (SIC) from ASI (AMSR-E), and SMOS brightness temperatures. Left y-axis for $T_{b,H}$ and $T_{b,v}$, right y-axis for Q, all SIT, SIC and air temperature at surface level. Shaded areas are excluded for retrieval training.

Table 3.1: Parameters for fit functions in Equations (3.1) and (3.2).

Parameter	a [K]	b [K]	c [cm]	d
I_{abc}	234.1	100.2	12.7	-
Q_{abcd}	44.8	19.4	24.1	2.1

Figure 3.4 shows the relation between the SIT and the polarization difference Q and intensity I , respectively, in our training dataset. The sensitivity of I to sea ice thickness decreases from 30 cm onwards, whereas Q is sensitive up to about 50 cm, considering their relative range of variation. However, the relative error of the brightness temperature difference is higher than it is with the intensity. The colored lines show polynomial fits of different degrees while the thicker black line shows the fit functions (Equations (3.1) and (3.2))

**Figure 3.4:** Fit functions compared to polynomial fit of first few degrees

For training, only the CFDD derived SIT from NCEP data is used. We decided against the HIRLAM based HIGHTSI model, because we perform a cross validation with a MODIS based ice thickness retrieval which is also driven by HIRLAM. Table 3.1 shows the optimal parameters for Equations (3.1) and (3.2) which best represents the training dataset as seen in Figure 3.4.

Figure 3.5 shows the two functions as a parameterized curve in the (Q, I) plane. The color of the points indicates the different regions (Figure 3.2). The curved black line

represents the SIT retrieved for a given pair (Q, I) . For finding the SIT for given I and Q , the minimum Euclidean distance to the retrieval curve is determined. Figure 3.5 shows that changes in Q only influence the retrieved SIT at higher intensities, thus it only influences SIT higher than 30 cm.

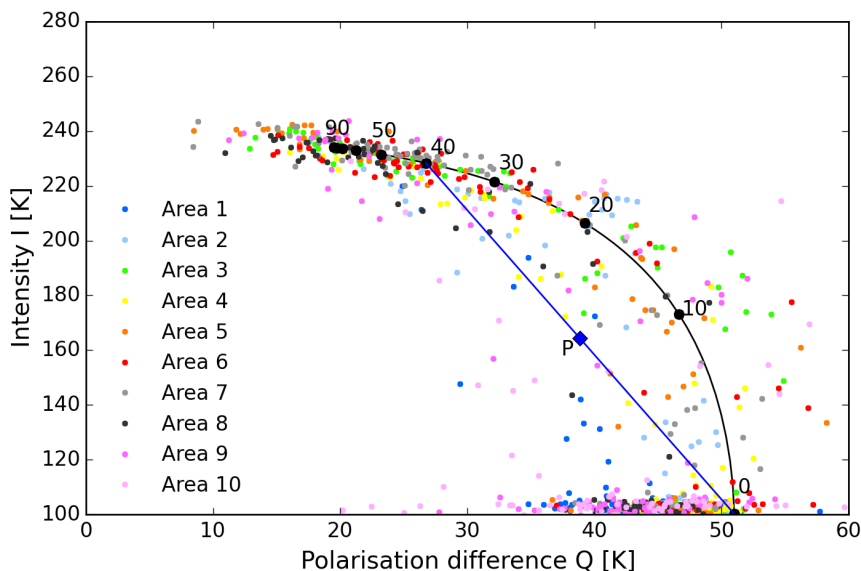


Figure 3.5: Q - I -plane with sea ice thickness fit line and corresponding ice thicknesses in 10 cm steps.

The current retrieval has no criteria to flag a returned value as unreliable, so that all points in the Q - I -space will end up with a valid SIT retrieval. At higher SIT the returned values are sensitive even to small changes of the observed I and Q . The uncertainty of the instrument is about 2 K to 3 K for a single measurement [Brown et al., 2008] in the instrument frame and can be higher in the earth reference frame. The error budget of daily averages within one grid cell is reduced by the averaging over the incidence angle range of 40° to 50° , but increased by the emissivity variations with incidence angle (Figure 3.1 (left)). As the sensitivity of the retrieved SIT to both intensity and polarization difference increases strongly with SIT (Figures 3.4 and 3.5), the retrieval is cut off at 50 cm SIT.

Higher retrieved values are marked by a flag for more than 50 cm but no distinct values are returned.

The retrieval assumes ice concentrations of 100%. As the two parameters I and Q do not scale linear with ice thickness an additional retrieval of ice concentration seems possible. An example observations $P=(Q, I)$ (Figure 3.5) then could be explained as a linear combination of open water (ice thickness 0 cm) and 40 cm thick ice. However, attempts to establish such a two-parameter retrieval have turned out to be quite noisy [Heygster et al., 2012]. Therefore, here we refrain from a two-parameter retrieval. The advantage

of introducing a second parameter is rather a gain of sensitivity in the upper range of ice thicknesses.

3.1.3 Uncertainty estimation

The uncertainties of the retrieval are estimated from the variability of the training data and corresponding brightness temperatures. For each 10 cm interval of the training NCEP CFDD SIT, the root mean square deviation (RMSD) to the SIT retrieved from SMOS is shown in Table 3.2. The uncertainty is about 30% of the retrieved value. The retrieval of very thin ice of 0 cm to 20 cm is quite accurate and stable. Higher retrieved SIT have a larger uncertainty and because of the restriction of the SIT retrieval to 50 cm, it might yield larger than stated deviations close to the 50 cm border. The RMSD values in Table 3.2 describe how well the retrieval curve represents the learning dataset based on the NCEP CFDD data. It includes the uncertainties introduced by the NCEP and CFDD models and by sea ice drift. Table 3.2 also includes the summary of validation approaches with external data. In the next section, the detailed comparison to these independent SIT values is described. This allows an error characterization independent of the learning dataset.

Table 3.2: Retrieval characteristics from learning and independent validation data sets. r is the correlation coefficient.

Data set	thickness range [cm]	RMSD [cm]	r
CFDD (learning)	0 - 10	3	
	10 - 20	7	
	20 - 30	9	
	30 - 40	14	
	40 - 50	16	
	average	0 - 50	10
MODIS	0 - 50	11	0.68
EM bird	0 - 50	5	0.73

3.2 Comparison and validation approaches

In the following, a comparison of the SMOS ice thickness retrieval to existing products estimating ice thickness, such as ice thickness estimates from MODIS, the electromagnetic induction based EM-bird is presented. In addition, a self consistency check comparing the daily changes of the ice thickness retrieval is performed.

3.2.1 MODIS thermal imagery ice thickness estimates

MODIS based ice surface temperature together with HIRLAM atmospheric forcing data was used to estimate thin ice thickness over the Barents and Kara Seas through the ice surface heat balance equation [Yu and Rothrock, 1996, Mäkynen et al., 2013]. The spatial resolution of the MODIS ice thickness charts is 1 km and they show SIT values from 0 cm to 99 cm. Only night-time MODIS data was employed. This validation dataset was provided within the SMOSice project of the ESA by the Finish Meteorological Institute (FMI) [Kaleschke et al., 2013].

Since originally MODIS has a much higher spatial resolution than SMOS, the MODIS data were averaged to the SMOS resolution. Another smaller discrepancy between the two data sets is that for SMOS the data of one day is averaged as part of the retrieval procedure while the MODIS data stem from single overflights.

The SMOS and MODIS SIT retrievals for one single day, the 4 December 2010 are shown in Figure 3.6 (top left and top center respectively)

The MODIS image shows incomplete coverage due to clouds. Some regions like North West of Novaya Zemlya show a good agreement in shape and thickness distribution of the sea ice. In the image center, East and South of the North East tip of Novaya Zemlya, SMOS retrieves higher SIT values than MODIS. Areas closer to the coast than 40 km are screened out because of potential land influence in the SMOS data. In Figure 3.6 (top right) the averaged MODIS SIT values suitable for comparison with SMOS SIT are shown. Similar studies have been performed for all days with a sufficient number of coincident SMOS and MODIS thickness retrievals from 24 November to 14 April 2011 with 71 scenes in total (not shown here). Figure 3.6 (bottom) shows the combined scatter plot. As the data have been taken under a variety of different conditions, the scatter is considerably large with a correlation of $r = 0.68$ and a RMSD with respect to the regression line of 11 cm. The line has a slope of 1.75, indicating that on average the SMOS retrieval gives 75 % higher SIT than the MODIS retrieval. Both retrievals agree best at low thickness. The regression line has been determined by minimizing the RMSD to the MODIS retrievals. For the assessment of the comparison with MODIS derived SIT, it should be mentioned that the MODIS SIT yields errors of mostly 40 % to 50 % [Mäkynen et al., 2013]. While the example shows good agreement of SIT from both sensors below 20 cm thickness which supports the conclusion of lower errors in this range (Table 3.2), we cannot attribute the statistical disagreement at higher thicknesses to any of the two sensors. In addition, the errors in the two retrievals stem from different sources. While the SMOS brightness temperatures are expected to have a higher random error due to lower radiometric accuracy and averaging over a large incident angle range while the atmosphere is close to transparent in the L-band, MODIS ice surface temperature may be influenced by thin clouds and fog missed by the MODIS cloud mask.

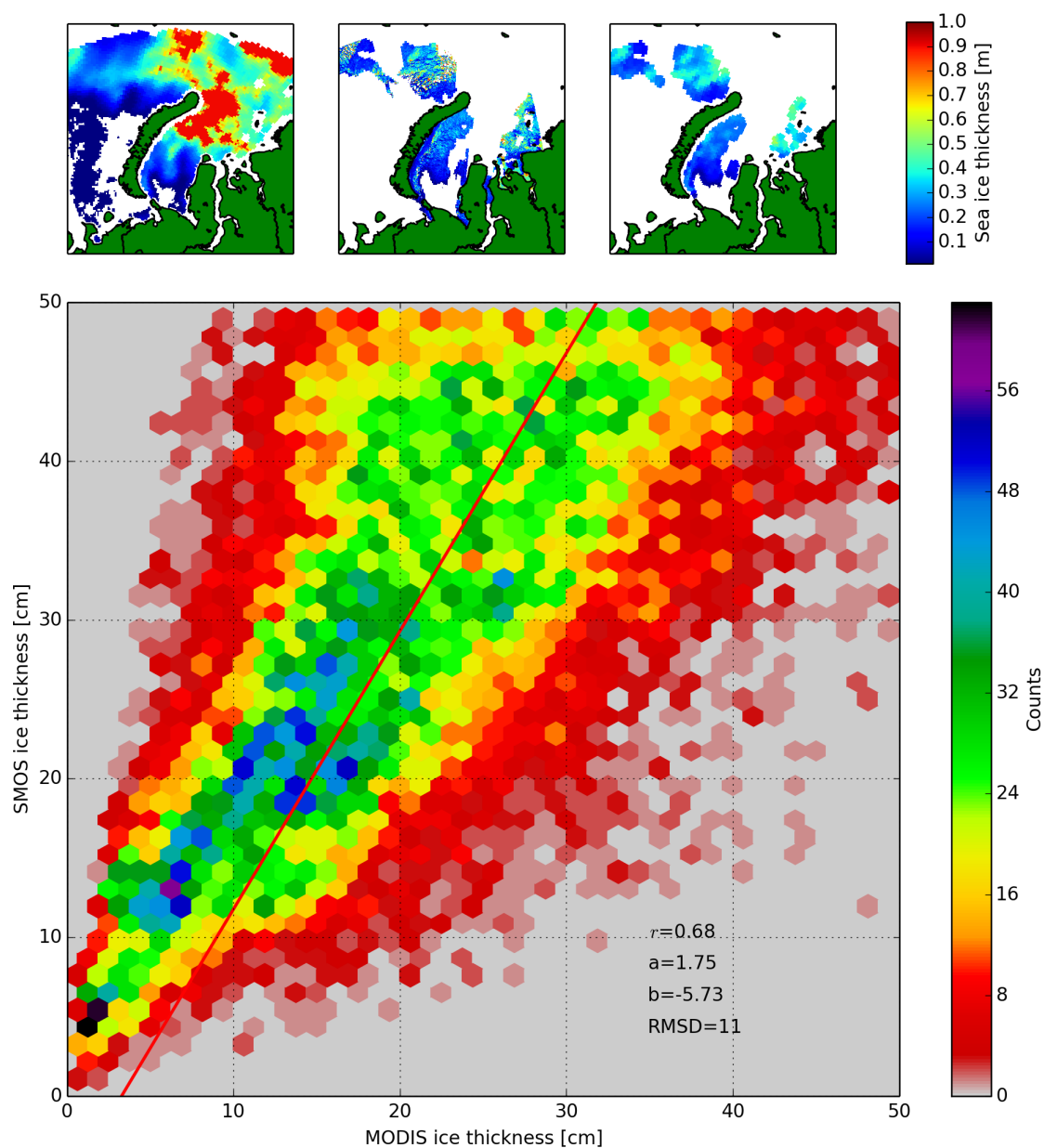


Figure 3.6: Comparison between SMOS (top left) and MODIS (top center) retrieved SIT for 4 Dec. 2010 in the Kara Sea. The valid MODIS data after averaging to the SMOS footprint size (top right). The scatter plot of MODIS and SMOS for all MODIS data from 24 Nov. 2010 to 14. Apr. 2011 (71 scenes) (bottom). Regression line (red): $y = 1.75x - 5.73$, RMSD = 11 cm, correlation of $r = 0.68$.

3.2.2 EM-bird airborne measurements

The Alfred Wegener Institute (AWI) has developed an airborne instrument to measure SIT when attached to a plane or helicopter [Haas et al., 2009], called EM bird. The method employs the contrast in electrical conductivity between sea water and sea ice for determining the distance to the ice-water interface, and from a laser altimeter the distance to the ice top. The difference yields the ice thickness [Haas et al., 2009]. It takes a measurement each 3 m to 4 m with typical footprint size of 40 m to 50 m diameter.

The SITs are determined at an absolute error of less than 10 cm for a single measurement [Haas et al., 2009]. For freshly frozen thin sea ice, the EM bird might underestimate the SIT since its conductivity is higher due to the higher salinity [Kruppen et al., 2011]. In regions like the Laptev Sea known for high variations in salinity through the year, the influence of the insufficiently known salinity has to be checked. An estimate of the mean and standard deviation of weekly sea surface salinity is given by Tian-Kunze et al. [2014]. The error associated to the conductivity assumptions of the EM-bird processing are estimated to be within the range of the instrument error because during processing manually identified regions of open waters are used to constantly calibrate the EM-signal. The uncertainty of the EM bird results of about 10 cm makes it suitable for validating SMOS SIT retrievals, which are expected to have a clearly higher uncertainty, especially in the upper thickness range.

On 20 April 2012 EM bird measurements were taken during a helicopter flight in the Laptev Sea over freshly frozen thin sea ice with negligible snow cover, shown in Figure 3.7 together with the SMOS retrieved SIT.

The considerable variability of the EM bird ice thicknesses within one single SMOS grid cell is shown in the histograms on the left. As the meteorological conditions of ice formation should have been quite homogeneous within the SMOS footprints during the short lifetime of this thin ice, the variability of ice thickness at this small horizontal scale should mainly be caused by mechanical redistribution of ice through the process of ridging, rafting, and shearing. Wadhams [1983, 1992] found for ice thicker than approximately 2 m an exponential tail of the thickness distribution. Here, the histograms reveal a similar exponential tail also for sea ice in the thickness range from 0.5 m to 1.5 m. Some studies also use lognormal distributions to describe ice thickness distribution [Haas et al., 2009, Tian-Kunze et al., 2014]. Close to the turning point of the helicopter (points 2, 3, 6, and 7) the SMOS retrievals are around 45 cm (purple), and those from the EM bird are mainly above 50 cm thickness but also contain a few thin values around 10 cm, possibly caused by leads much smaller than the SMOS footprint size (see black circle in Figure 3.7 (right) for an example). Since the EM bird measurements and the corresponding averages are taken along a narrow line of its footprints of 40 m to 50 m width, but the SMOS footprint covers a large area of about 50 km in diameter, we have to expect larger discrepancies in the SIT retrievals from the two instruments. The fraction of SMOS footprint area covered by EM

bird measurements along one the flight track is less than 0.1%. The colored vertical lines in the histograms in Figure 3.7 correspond to the mean (purple) and median (cyan) of all EM bird measurements within the corresponding SMOS footprint while the yellow lines show the retrieved SIT by SMOS. In almost all cases the SMOS retrieval agrees better with the median because it is less influenced by the long tail of high thickness values in the distribution. The only case of larger disagreement is the histogram of point 14 where the EM bird median thickness is 25 cm and the SMOS thickness exceeds its limit of 50 cm. This is in agreement with the map of Figure 3.7 (right) where the SMOS SIT mostly exceeds 50 cm within the size of a footprint (black circle) around point 14. Apparently, these thick ice regions are missed by the EM bird measurements (small gray dots) as can be seen in the histogram. This is an example for the more general case where parts of the SMOS footprint are covered by ice thicker than SMOS can retrieve. Therefore, this case is excluded from the comparison in Figure 3.8. The histogram of point 3 near the turning point of the flight shows a pronounced bi-modal shape indicating at least two different regimes of ice thickness within this SMOS footprint. As the EM bird thicknesses in Figure 3.7 are the best large-scale in situ observations of thin sea ice we currently have, we perform the comparison in the scatter plot Figure 3.8 in spite of the small number of data points from a quite limited region and season entering the comparison. The diagram shows a good agreement with correlation coefficient $r = 0.73$ and RMSD of 5 cm.

3.2.3 Day-to-day differences – plausibility check

The two previous comparisons have shown the limitedness in space, time and sea ice thickness of validation data available to us. Therefore, as an additional, more global consistency check the SIT difference of two consecutive days, the 20 and 21 October 2011 was investigated (Figure 3.9 (left)). As the thermodynamic thickness growth within one day is limited, large changes are either due to drift or errors in the retrieval. In most regions of the map the change is only a few cm as expected. Some areas show larger differences like the central Arctic (80°N , 150°E) or the Beaufort Sea (75°N , 140°W). In the Beaufort Sea narrow parallel bands of opposite sign in SIT difference are visible. These indicate sea ice drift which is confirmed by the vectors of the sea ice drift product from the OSI-SAF [Lavergne et al., 2010] running perpendicular to the bands of high sea ice thickness change (Figure 3.9 (right)). Other regions of high thickness change are found near the upper limit of the retrieved sea ice thicknesses where the retrieval noise is higher, extending e.g. East of North Greenland, North of Svalbard and Franz Josef Land. The strong increase in thickness in the Laptev Sea is in good agreement with CFDD based modeled growth of very thin ice at temperatures around -10°C .

Figure 3.10 provides histograms of all positive (red) and negative (blue) day to day changes from October to December 2010. Most frequently are the plausible changes between around 1 cm. This range covers about 90% of all pixels. Negative changes of a

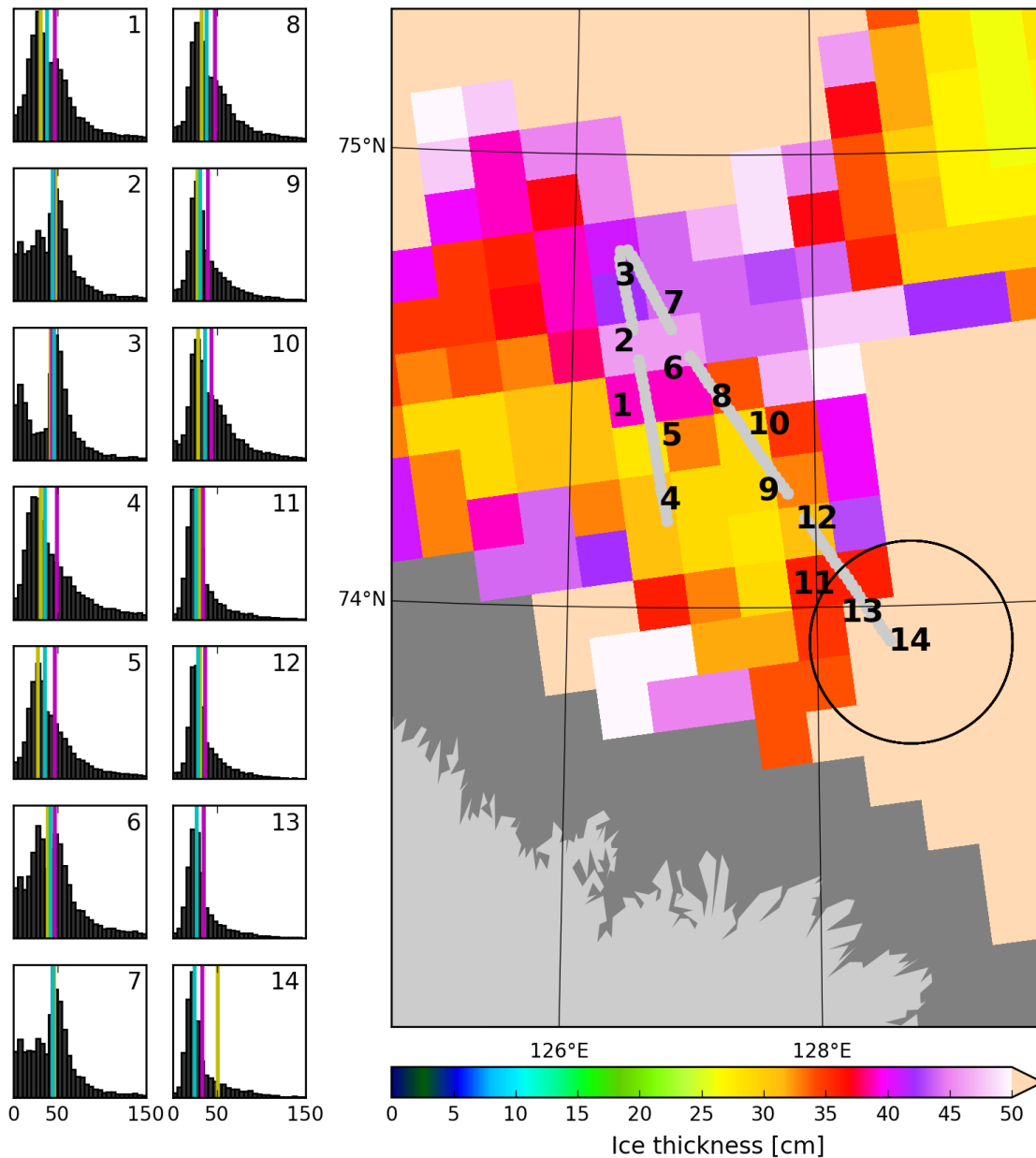


Figure 3.7: Comparison of SMOS and EM-bird ice thicknesses in the Laptev Sea on 20 April 2012. The numbers indicate the SMOS footprints while the light gray line shows the EM-bird track. Each histogram shows the frequency of occurrence of EM-bird measured ice thickness within the corresponding SMOS footprint. The colored vertical lines are mean (purple) and median (cyan) the EM bird measurements and SMOS retrieved ice thickness (yellow) in the corresponding SMOS footprint. A sample SMOS footprint size (diameter of 50 km) is shown as black circle around number 14.

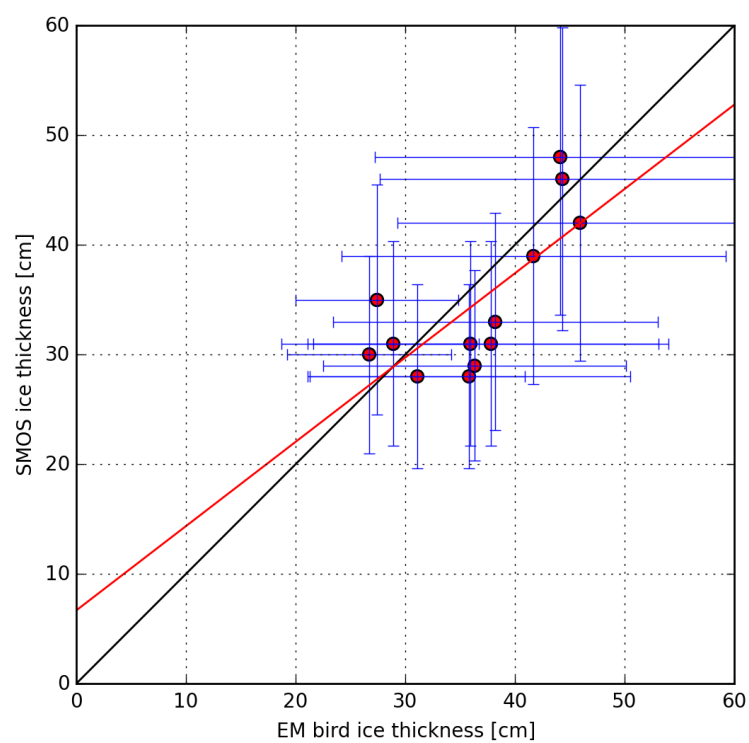


Figure 3.8: Scatter plot of SMOS retrieved ice thicknesses and median EM-bird ice thicknesses. For SMOS error bars are 30% of the values (see Section 3.1.3), while for EM-bird the median absolute deviation is shown.

few cm thickness are considered plausible here because of the uncertainty of the retrieval procedure. According to the overall sea ice increase in the freezing season, on all days the positive changes overbalance the negative ones. The average daily increase in SIT is 0.3 cm with a standard deviation of 3.3 cm reflecting the average ice thickness change throughout the Arctic. Higher changes in SIT than ± 8 cm are detected in less than 0.5 % of the cases. Such strong ice thickness changes will not be generated thermodynamically but are drift or other disturbing influences, as, according to Equation (2.16), an ice thickness growth from e.g. 2 cm to 10 cm within one day requires an air temperature of -30°C . In conclusion, the SMOS data generally provides a realistic scenario for a daily ice thickness development in the Arctic during the freeze up period.

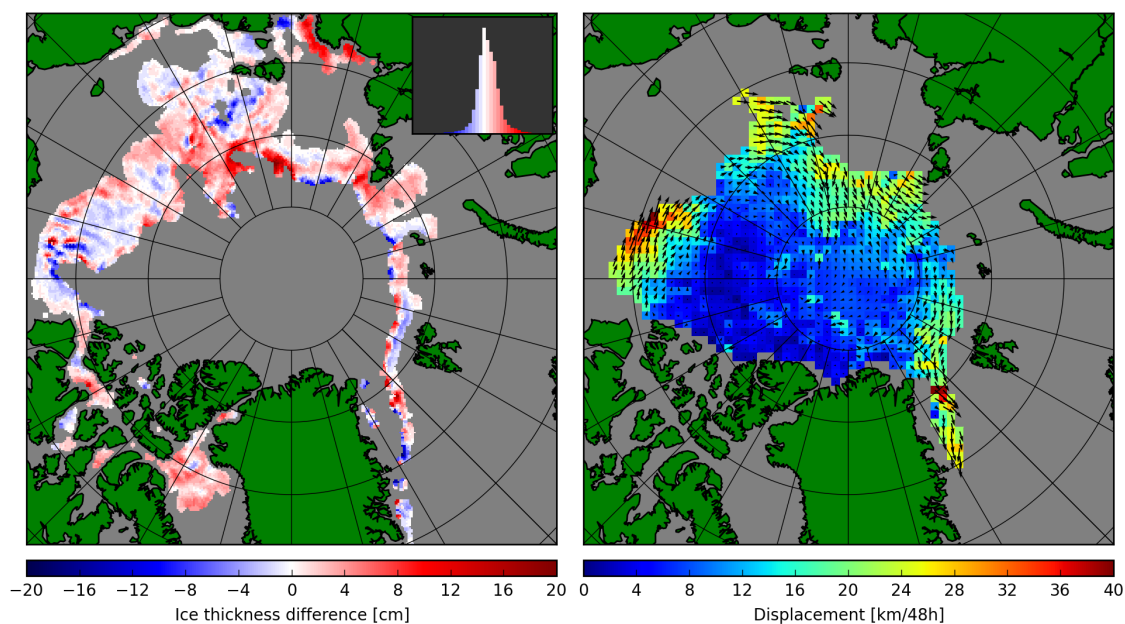


Figure 3.9: Left: difference map of SMOS SIT retrieval from 20 to 21 October 2011 in the ice growth phase. Areas of open water and areas where the retrievals 50+ cm flag is set are excluded. Histogram of day to day change from 20 to 21 October 2011 (top right). Right: OSI-SAF sea ice displacement product from 19 to 21 Oct 2011.

3.3 A sea ice thickness product

3.3.1 Operational implementation and data distribution

For the continuous production of daily SMOS ice thicknesses, an operational processing chain was set up. The data is acquired from an FTP server from ESA. Originally, the data was available in the L1C product only about 24h after acquisition as the processing. For the purpose of Near Real Time (NRT) processing, the data was also available in the

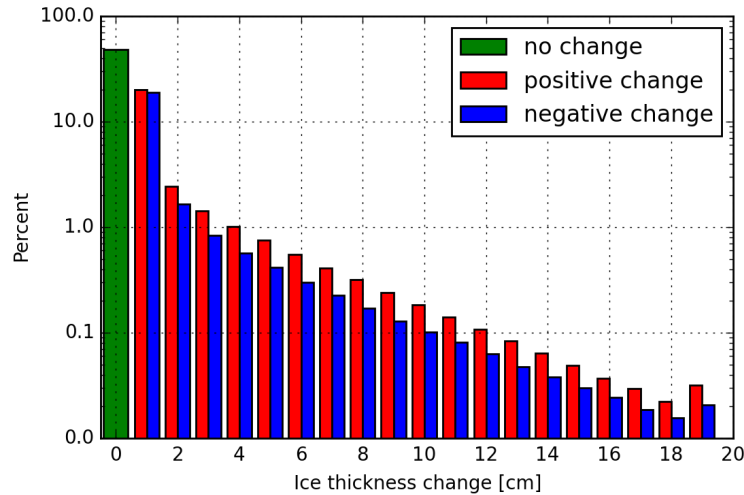


Figure 3.10: Histogram of daily change of SIT from 1 Oct to 26 Dec 2010.

Binary Universal Form for the Representation of meteorological data (BUFR) format about 4 to 6 hours after acquisition. It was mainly meant for the soil moisture community and therefore had more sparse sampling over the ocean surface. Even though in the beginning we used the BUFR product to provide NRT service, nowadays the LIC data provision is fast enough for this purpose as well. The processing is scheduled now at 8 am CET for the day before and takes about half an hour. For the case that not all data for that day is available on the FTP, at 6 am CET of the following day. Downloading and potential reprocessing of a day is scheduled. Usually only few swaths are missing, so that complete coverage of all Arctic and Antarctic regions is achieved after the first run and the repeated processing a day later changes the products only slightly.

Two different products are available, a RFI filtered and unfiltered version for Northern hemisphere. For the Southern hemisphere no RFI filtered product is needed as RFI is negligibly small. The processing chain consists of downloading, filtering, application of the retrieval algorithm, and output into gridded products of several formats. As grid, the National Snow and Ice Data Center (NSIDC) polar stereographic grid with 12.5 km resolution is used. The available formats are Portable Network Graphics (PNG) (images), GeoTIFF (data and images), and Network Common Data Format (NetCDF) (data) which are available. A website (www.iup.uni-bremen.de:8084/smos) was created which provides basic functionality for browsing through images and download links to all data products.

3.3.2 Users and applications for thin sea ice data

Our SMOS ice thickness product was involved in different projects and activities like the EU project Sea Ice Downstream services for Arctic and Antarctic Users and Stakehold-

ers (SIDARUS), the Federal Ministry of Education and Research / Bundesministerium für Bildung und Forschung (BMBF) project Midterm Climate Prognosis/Mittelfristige Klimaprognose (MiKliP), the ESA project Sea Ice - Climate Change Initiative (SICCI) and the EU project Polar Ice. For SIDARUS the website and the operational daily processing was developed (at that time also with the BUFR format). For MiKliP monthly means of the thin ice product were provided for comparison with mid-range climate models. The thin ice product was used within SICCI together with manual Synthetic Aperture Radar (SAR) analysis in homogeneous ice covered region to estimate the influence of thin ice to current passive microwave ice concentration retrieval algorithms [Heygster et al., 2014, Ivanova et al., 2015]. Within the Polar Ice project the thin ice data is used in an operational feed together with many other sea ice related products for the integration into a common sea ice data portal (no public release yet).

3.3.3 Conclusions and remarks

An operational empirical ice thickness retrieval for SMOS is presented. The retrieval currently assumes 100% ice concentration. It is difficult to correct for ice concentration as current passive microwave retrievals underestimate the ice concentration in case of thin ice as shown by recent studies [Heygster et al., 2014]. The SMOS retrieval is sensitive to the dielectric properties of the surface and thus will not give reliable results during the summer period when the surface conditions may change drastically within a small time frame and snow and ice becomes wet. In summer in addition melt ponds will have similar characteristic as open sea water to the microwave signal which would alter the ice thickness retrieval. Without other microwave remote sensing based support for detection of melt onset [Drobot and Anderson, 2001, Smith, 1998] the SMOS ice thickness retrieval is restricted to winter season from October to April in the Arctic and March to September in the Antarctic. However, this general seasonal restriction will not entirely remove melt contamination in the data due to the variability of the melt season [Markus et al., 2009, Belchansky et al., 2004]. Since SMOS brightness temperatures are quite sensitive to the incidence angle in the range of 40° to 50° (Figure 3.1), this may increase the uncertainty in addition to the intended stabilizing effect from the angular noise in the SMOS data. This effect is further addressed in Section 5.1, where functions are fitted to improve stabilization while preserving the brightness temperature to incidence angle dependence. The current retrieval is only empirical and is not supported by other data like the retrieval presented by Tian-Kunze et al. [2014] which employs temperature and salinity information to refine the ice thickness estimate. Another question arises from the influence of the snow cover and its dielectric and thermal insulation properties on the brightness temperatures. Maaß et al. [2013] presented a snow depth retrieval based on the thermal insulation over multi year ice. In the next chapter we will employ a thermodynamic and a microwave emission model to compare the empirical retrieval with various modeled ice condition to develop

3.3. A sea ice thickness product

a deeper understanding of the geophysical influences on the brightness temperatures like temperature, salinity and snow cover.

4 | Emissivity modeling

To estimate the signal expected from SMOS over sea ice as support for the empirical retrieval, modeling of the sea ice emissivity is needed. Previous model studies and observations showed an ice thickness dependence in the low frequency microwave emission of sea ice Heygster et al. [2009], Thomas and Dieckmann [2009], Menashi et al. [1993], Apinis and Peake [1976] before the launch of the first satellite based L-band radiometer. The emissivity of sea ice depends on the general macro structure and micro structure of the sea ice. The history of modeling of the thermodynamic properties of sea ice is summarized by Untersteiner [1986], Shokr and Sinha [2015] while the most relevant quantities for the L-band emission are described in Section 2.2.

In this section we chain the output of an atmospheric model to a thermodynamic ice growth model simulating first year ice profiles which serve as input to a microwave emission model. The modeled brightness temperatures are compared to the empirical relation we established for SMOS data in Chapter 3.

4.1 Ice atmosphere interaction — an energy balance model

We use an energy balance model by Tonboe et al. [2011] based on the Crocus model for snow accumulation [Brun et al., 1992]. The model computes the surface energy flux, mass balance, and snow and ice interaction using atmospheric input data. The atmospheric input parameters can be taken from ECMWF ERA 40/interim [European Centre for Medium-Range Weather Forecasts, 2004], Japanese ReAnalysis (JRA) 25/55 [Japan Meteorological Agency, 2013] or Arctic System Reanalysis (ASR) [Byrd Polar Research Center - The Ohio State University, 2012]. Table 4.1 lists the atmospheric variables used by the energy balance model as they have the strongest influence on the sea ice and snow evolution

[Tonboe et al., 2011].

Table 4.1: ECMWF input to thermodynamic model

#	Quantity	Unit
1	Time (currently assumes 6-hourly data)	h
2	Sea level pressure	mbar
3	Surface air temperature	K
4	Wind speed	m s^{-1}
5	Shortwave radiation energy (downwards)	$\text{W m}^{-2} \text{s}^{-1}$
6	Longwave radiation energy (downwards)	$\text{W m}^{-2} \text{s}^{-1}$
7	Dew point temperature	K
8	Precipitation	kg m^{-2}

4.1.1 Initial conditions and assumptions

The initial condition for the sea ice growth is a 1 cm ice layer of 269 K temperature and 22 ppt salinity. The sea ice evolution is then modeled from the current sea ice condition and the current atmospheric input in order to derive the state of the sea ice for the next time step.

For the determination of sea ice growth, the temperature gradient from the top layer to the bottom layer with respect to ice thickness is used [Maykut and Untersteiner, 1971, Timco and Weeks, 2010]. Therefore, the growth rate is decoupled from the temperature, heat capacity, and from the heat flux at bottom layer and thus deviates from the energy balance approach. The salinity of newly formed layers is calculated from the ice growth rate as described by Equation (2.17) [Nakawo and Sinha, 1981]. During the model run, the salinity of each finished ice layer is fixed over the whole simulation which turned out to be a good assumption in past studies for the Arctic freeze up [Nakawo and Sinha, 1981, Untersteiner, 1986]. Dynamic desalination processes within the ice are not modeled. The influence of density on the sea ice emissivity is little, so that the density is set to a fixed value of 920 kg m^{-3} for all sea ice layers.

In the model the thermal insulation of sea ice is overestimated compared to traditional models leading to a linear temperature gradient through the sea ice during the freeze up [Timco and Weeks, 2010, Thomas and Dieckmann, 2009]. Here we will discuss both, simulations with the original model, and simulations with linearized temperature profiles. To ensure that the energy balance model is not influenced by the modification of the temperatures of the ice column, these are only changed at the interface to the microwave emission model (see next section). The following time steps in the energy balance model are unaffected by this modification.

A schematic illustration of the layered output from the energy balance model is shown in Figure 4.1. The sea ice column generated by the energy balance model is discretized

into 2 cm thick layers. E.g., For the case of 50 cm thick sea ice, there are about 25 layers for sea ice as input for the microwave emission model.

The snow modeling includes the heat exchange, grain size evolution, gravity based compaction and the energy contribution by the precipitation. The thickness of a single snow layer has no upper nor lower limits. As a consequence of this complex one dimensional snow model, the layers and the total snow thickness can increase and even decrease (as a consequence of compaction) over time.

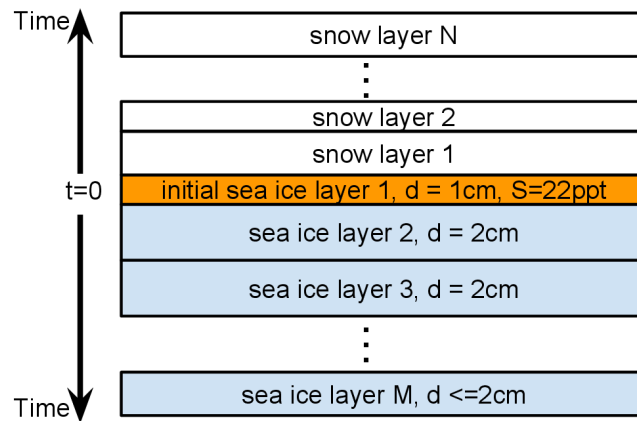


Figure 4.1: Diagram of layered sea ice evolution output from energy balance model.

A typical temperature and salinity profile from the energy balance model is shown in Figure 4.2. The y-axis shows the depth below the sea ice surface. On the upper x-axis the temperature is shown for the original (red) and linearized (blue) profile. The green line corresponds to the salinity which can be read from the lower x-axis. At 20 cm ice thickness, the salinity strongly increases due to an increase in growth rate as a consequence of a drop in the air temperature. With the fixation of salinity once a layer reaches 2 cm, the effect of brine expulsion is not also modeled, so that the characteristic C-shape of the salinity profile during the freeze up period cannot be reproduced with this model Petrich and Eicken [2010].

As input of atmospheric conditions we take ECMWF ERA 40 data, since it supplies all needed variables (Table 4.1) in 6 h time steps. We select sample regions known for the certain occurrence of first year ice. The simulations are initiated at different starting times as the date of the first formation of sea ice varies among the regions. We take the first occurrence of sea ice in from the variable *sea ice cover* of the ERA 40 model as indicator for the start of ice formation. Typically, the ice forms at air temperatures much lower than the freezing point of the sea water, i.e., the sea water releases its sensible heat to the atmosphere until the freezing temperature is reached.

For each of the 18 selected regions (Figure 4.3), the month October to March are taken

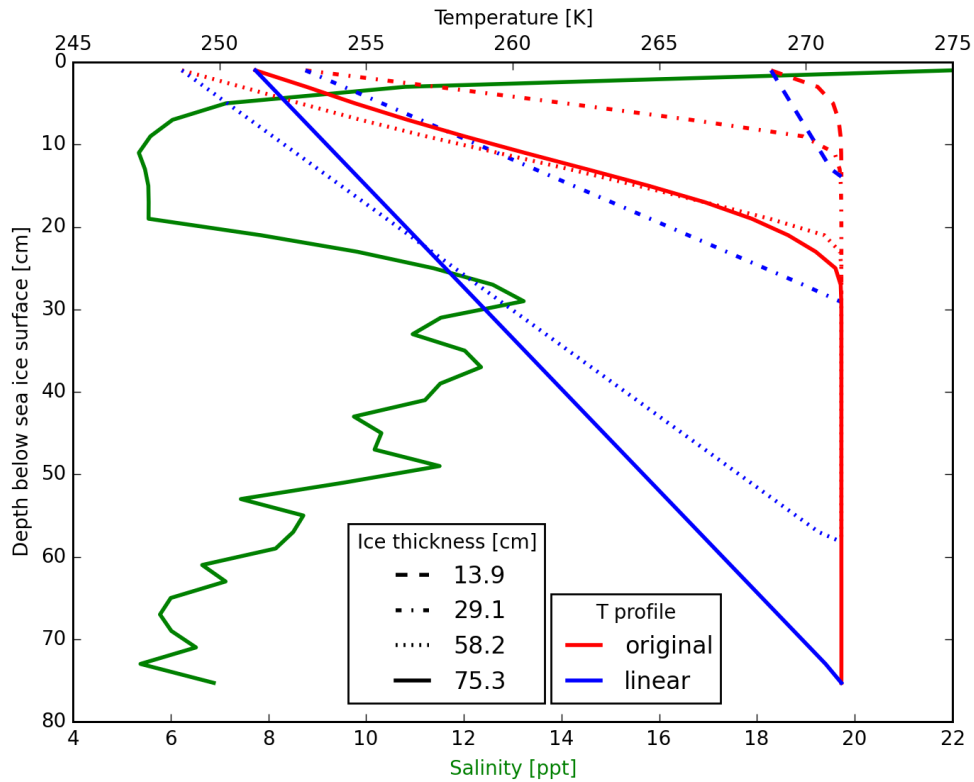


Figure 4.2: Example sea ice profile generated by the energy balance model at 13.9 cm, 29.1 cm, 58.2 cm and 75.3 cm indicated by line styles. Original model temperature profile (red), linearized temperature profile (blue) and salinity profile (green). The salinity of a layer is fixed so that the profile applies to all ice thicknesses up to the specific depth, given by the ice thickness value.

from 20 years (1980-2000) of ERA-40 data. In total 283 time series with 6 h resolution resulting in more than 100.000 individual snow and sea ice profiles were generated by the energy balance model as input for the microwave emission model. We take a region as qualified for a single winter season if no sea ice is present at the beginning of October according to ECMWF ERA 40 data.

Note that many common first year ice regions of recent years are not used because in most of the years from 1980 to 2000 these regions were not yet ice-free in summer.

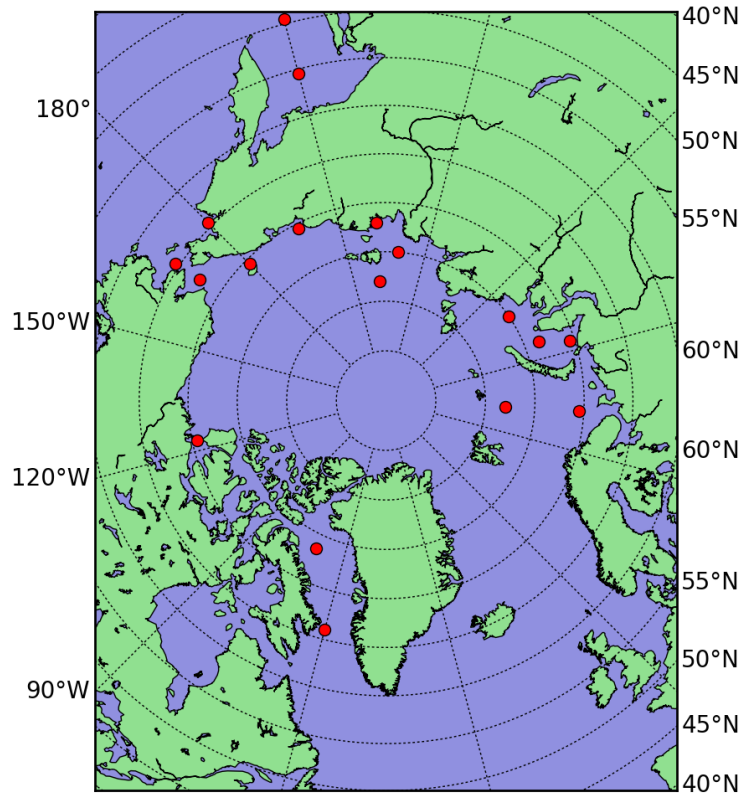


Figure 4.3: 18 selected regions where 20 years of ECMWF ERA 40 data were taken as input for ice growth simulation using the energy balance model. All regions were ice free on 1. October 1980.

4.1.2 Precipitation and snow cover on sea ice

The energy balance model assumes that precipitation is snowfall if the temperature is below 0°C . To avoid constant tiny precipitation which often occurs in the ECMWF data, the energy balance model pools snow fall to release more rare but stronger precipitation events which seem more realistic [Tonboe et al., 2011]. As a consequence the snow depth on sea ice can increase from one time step to the next by more than 20 cm and causes strong variations in the snow layer thickness of the snow pack.

All, more than 100.000 sea ice thickness and snow depths profiles resulting from the model run on the 18 regions of 20 years of ECMWF ERA 40 data are shown in Figure 4.4. In all simulations the sea ice has no snow cover immediately after the ice formation. The thicker the ice grows, the more likely snow accumulation on top as consequence of precipitation events. The snow depth is in most cases lower than the ice thickness which is in agreement with observations [Thomas and Dieckmann, 2009]. An upper limit for snow thickness in our simulations is observed at about 40 cm. At the strong snow fall events which are indicated by the highest peaks in Figure 4.4, the densification of the snow is visible as the snow depth decreases while the sea ice thickness increases steadily. From 30 cm onwards, snow depth values cover the range from 0 cm to about 30 cm and no dependence on ice thickness can be recognized in the mean snow depth. In case of precipitation at air temperatures of $T < 0^\circ\text{C}$ rain is simulated with an accumulation of a dense freshwater ice layer within the snow cover. In some rare cases nearly no precipitation accumulated on top of the sea ice during the growth phase. We assume that the simulated results reflect the most probable cases occurring in the Arctic during the freeze up period.

Note that if the mass of the snow cover exceeds the buoyancy of the sea ice, flooding occurs. However, these events are rare in the Arctic and are currently not simulated by the energy balance model. In Figure 4.4 flooding would occur in cases above the blue line assuming densities of 1000 kg m^{-3} , 900 kg m^{-3} and 300 kg m^{-3} for water, ice, and snow, respectively. In the energy balance model the snow cover seems overestimated especially for small ice thicknesses as even the mean snow depth (red) is above the flooding criterion (blue).

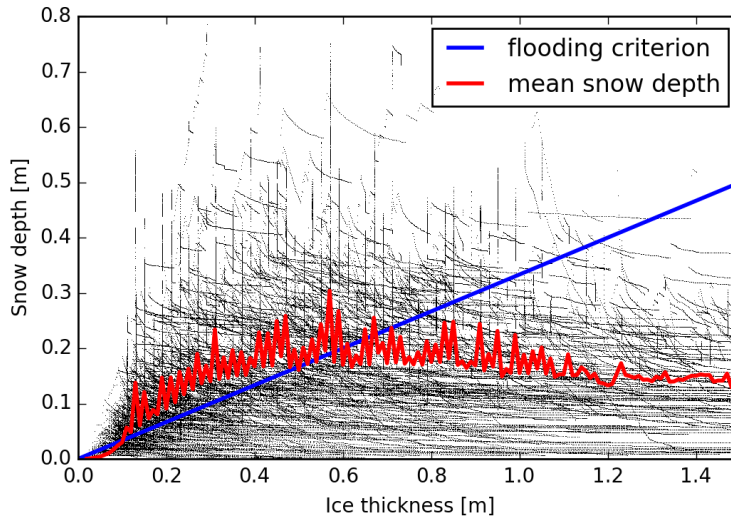


Figure 4.4: Simulated ice thicknesses versus snow thickness in 18 regions of 20 years of simulated ice conditions from ECMWF data. Mean snow cover per ice thickness is shown in red. Cases above the blue line would cause flooding (not modeled).

4.1.3 Review of energy contributions

The model accounts for several forms of energy balance contributions, namely shortwave radiation, longwave radiation, precipitation, sensible heat and latent heat. In the following we shortly discuss their definition and meaning for the snow and sea ice system. Here we speak of fluxes, i.e., difference between incoming and outgoing energy. Note that in the following we use the words *heat* and *energy* synonymously to meet literature conventions on the specific terms.

- Shortwave energy arrives at the sea ice from the sun. In winter the contribution from the shortwave radiation is negligible during the polar night. As the sea ice and snow cover does not emit radiation in the shortwave regime, its contribution can only be positive.
- Latent heat is the energy required or released due to a phase change, in our case from solid to liquid and from liquid to vapor. As it is not an external energy but energy which is already in the system, its contributions is defined by the amount of mass involved in the phase translation. The other energy types are the major drivers for the release and uptake of the latent heat.
- Sensible heat is the energy exchanged due to direct contact of masses. In the energy exchange with the atmosphere, it is a direct temperature and wind speed driven exchange. The contribution can be positive (warming) or negative (cooling) to changing air temperature. Simply put, the air cools the surface (negative energy contribution) or the surface cools the air (positive energy contribution).
- Precipitation heat is the contribution by introducing new mass into the system having a certain temperature and heat capacity.
- Longwave energy summarizes the longwave radiation emitted from the snow and sea ice directed upwards to the sky and the reflection and emission by the atmosphere, which means mainly the contribution by clouds.

The cumulative energy balance of all kinds discussed above entering the snow and sea ice system from the atmosphere is shown in Figure 4.5. The energy contributions are cumulatively summed hourly from the initial freeze up. Sensible heat and longwave radiation are the major energy balance contributions. In some cases, the sensible heat has small local minimums and maximums which are caused by a change of the sign of the difference between air temperature and ice temperature. At the end of the freeze-up global minimums are reached in the sensible heat contribution from where on the atmosphere has a constant warming effect on the snow and sea ice. In all the cases, the longwave radiation has a cooling effect as expected and it is the driving force for sea ice growth, with a larger and more consistent contribution than the sensible heat. Here, the question arises

of how the ice growth can be modeled accurately from only the temperature information when the energy contribution from the sensible heat is not the driving force. This can be explained when viewing at all energy contributions as a coupled system in which the air temperature is a part of the entire environmental condition. At the end of the growth phase the shortwave energy contribution increases as more and more sun hours accumulate in March.

4.1.4 Comparison to CFDD based model

The empirical CFDD based ice growth model (Equation (2.16)) should on average agree with the ice growth modeled by the energy balance model. The only free parameter which is expected to effect ice growth is the thermal insulation by the snow cover. We therefore expect for bare ice or small snow cover the CFDD based ice growth rate to be less than for the energy balance model as the latter accounts for the snow cover explicitly. For thick snow layers the heat exchange between atmosphere and sea ice is reduced, so we expect the ice thickness from the energy balance model to be lower than the CFDD based ice thickness.

Figure 4.6 shows the ice thickness from the energy balance model compared to a simple CFDD based model. The CFDD based sea ice thickness is higher on average. Up to 0.2 m the slope is steeper thus the CFDD based ice growth is faster compared to the ice growth in the energy balance model. At a thickness of 0.3 m onwards, the energy balance model starts to fit the ice growth rate from the CFDD based model as most of the lines go parallel with the one-to-one-line (black). For some lines, after strong snowfall the ice thickness remains constant while more snow accumulates on top. This effect can be promoted by temperatures near the freezing point at the surface, since the growth rate is primarily a function of the temperature gradient. Overall, the expected decrease of sea ice growth with increasing snow cover is visible from the color gradient from the snow thicknesses along the CFDD based ice thickness axis. Figure 4.6 reveals that the ice growth from the CFDD based model can be reproduced with the energy balance model. However, from 0 cm to 20 cm the growth rate do not match between the models. In addition, the early stop of ice growth in the energy balance model deserves more attention and will be investigated in Section 4.3.

4.2 Sea ice emissivity from MEMLS

For all snow and sea ice profiles obtained from the energy balance model discussed in Section 4.1, the microwave emission has to be modeled. For modeling $T_{b,H}$ and $T_{b,V}$, we employ the Microwave Emission Model of Layered Snowpacks (MEMLS) Wiesmann and Mätzler [1999], Mätzler and Wiesmann [2012]. It was originally developed for microwave emission of the snow cover in the Alps and was adapted to sea ice later [Tonboe, 2005]. MEMLS

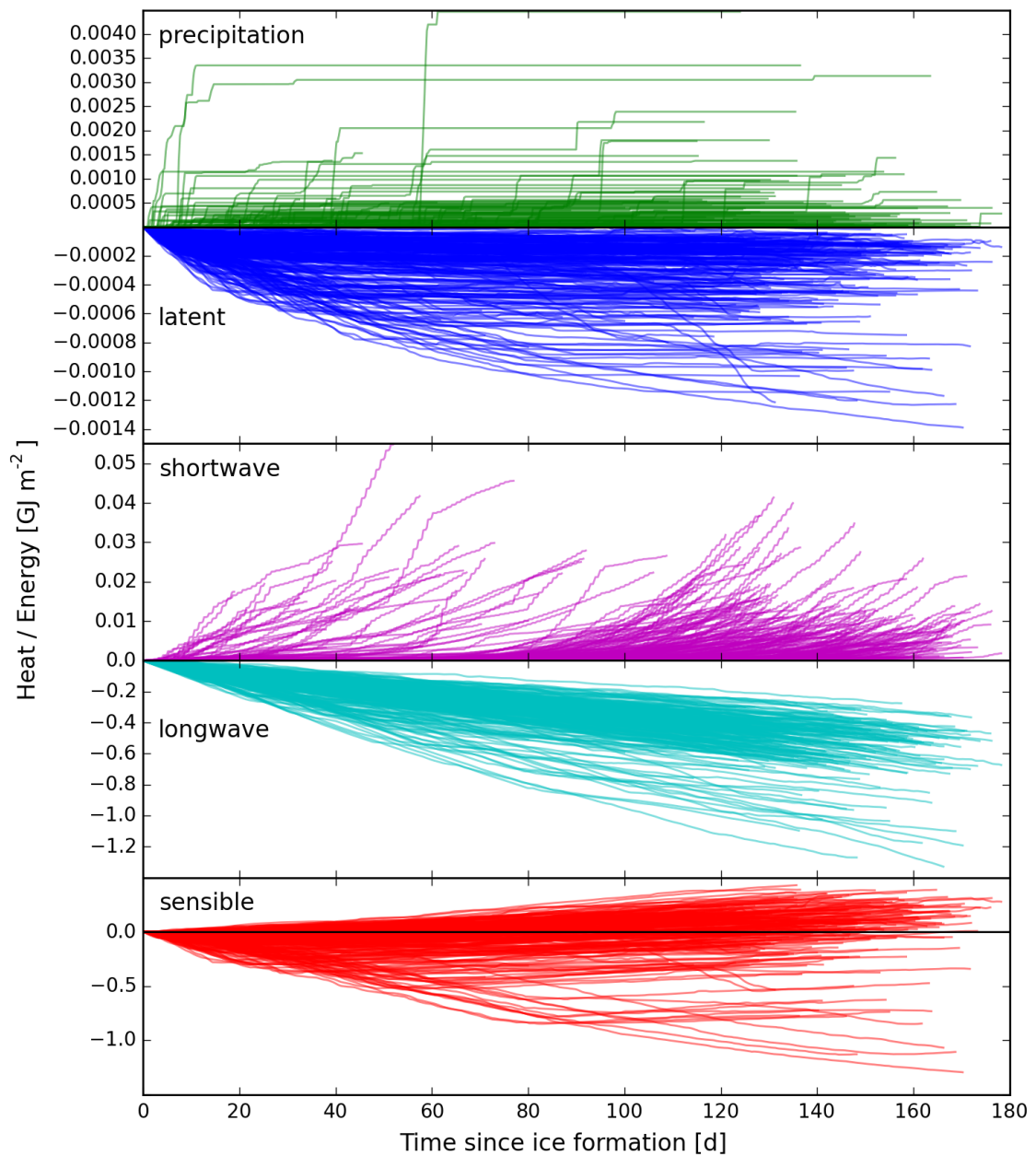


Figure 4.5: Energy fluxes of different types as modeled by the energy balance model during the freeze up season. Each line shows the energy flux from one single freeze up season for a single location. Major contribution from the longwave and sensible heat. Shortwave energy raises after the polar night, close to the end of the growth season. Small contribution due to sensible heat and precipitation.

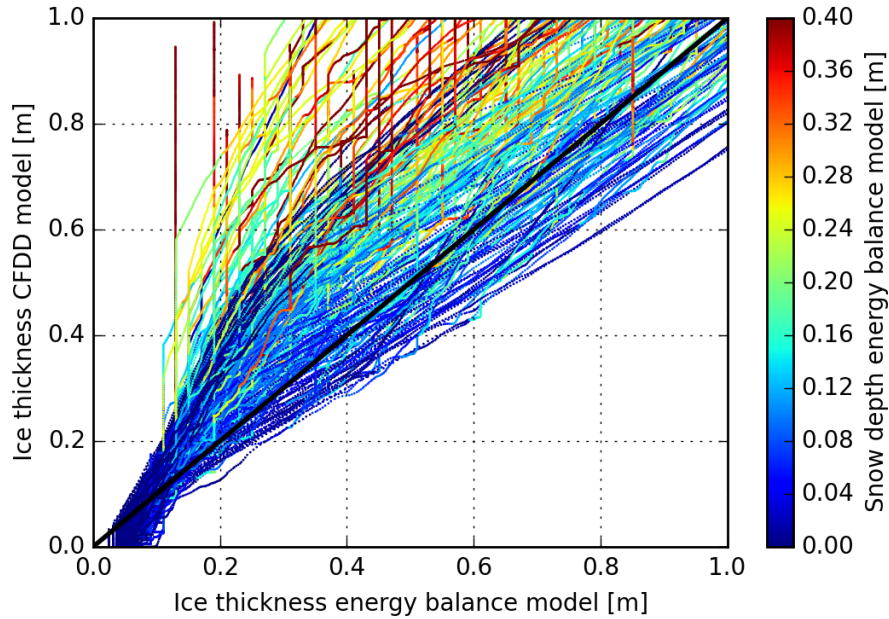


Figure 4.6: Scatter plot of modeled ice thicknesses from energy balance model and CFDD based ice thickness model. Colors indicate the snow thickness from the energy balance model.

employs a radiative transfer approach with a 6-flux model to account for directional scattering. The volume scattering at the ice inclusions is modeled using the improved Born Approximation [Mätzler, 1998]. The dielectric properties of snow and sea ice are modeled after the frazil and columnar ice model [Shokr, 1998] while snow dielectric properties are modeled as described by Tiuri et al. [1984] (Section 2.2.4).

The output of the energy balance model is designed to serve as input for MEMLS, so that all input parameters for MEMLS are delivered by the energy balance model. Table 4.2 lists the input values given for each layer. Three parameters need further explanation at this point. The exponential correlation length is a measure of grain size within MEMLS and is used to calculate the volume scattering properties. The liquid water fraction is mainly to calculate the dielectric properties for wet snow and is not used for sea ice. Liquid brine inclusions inside the sea ice are calculated from the temperature and salinity parameters as described in Section 2.2 and are not connected to the input of liquid water fraction. To describe the type of layer and chose the corresponding scattering and dielectric mixture model, a type code is used. It can take values of 1-4 with 1 for fresh snow, 2 for old or wet snow, 3 for first year ice, and 4 for multi-year ice. The thermodynamic model currently has no mechanism implemented to transform layers into other types. Thus, the process of aging of first-year ice and resulting creation of multiyear ice is not modeled as well as fresh snow does not turn into old wet snow in this model.

Table 4.2: Output from energy balance model and input for the microwave emission model.

#	Quantity	Unit
1	Layer number	-
2	Temperature	K
3	Layer type (1,2,3 or 4)	-
4	Density	kg m ⁻³
5	Thickness	m
6	exponential correlation length	mm
7	salinity	ppt
8	liquid water fraction (0-1)	1

Two different sets of sea ice profiles are simulated:

- original temperature profile
- linearized temperature profile

A typical case of the original temperature profile was shown in Figure 4.2. The temperatures of approximately the lower 70 % of the layers are close to the freezing point in the original temperature profile. This biases the effective emitting layer temperature towards the water temperature especially at 1.4 GHz where the radiation can origin from deeper layers compared to higher microwave frequencies.

4.2.1 Original temperature profile

The simulated $T_{b,H}$ and $T_{b,V}$ at 50° incidence angle versus sea ice thickness are shown in Figure 4.7. The upper series of curves are $T_{b,V}$, the lower series are $T_{b,H}$. $T_{b,V}$ shows more stable brightness temperatures, reaches saturation with ice thickness at about 20 cm and also shows slight dependence on the snow depth. $T_{b,H}$ on the other hand shows lower brightness temperatures but with a more pronounced dependence on the snow cover. $T_{b,H}$ shows a saturation at about 30 cm SIT but shows a higher scatter at all SITs compared to $T_{b,V}$. Vertical lines with a gradient in snow thickness originate from strong precipitation while the energy forcing was not strong enough to cause further ice growth. This effect is amplified by the insulation of the snow and is addressed in Section 4.3. The stair-like structure in the low ice thicknesses in both $T_{b,H}$ and $T_{b,V}$ is caused by the discretization of the layers into 2 cm steps. Since the first sea ice layer is 1 cm thick (see Section 4.1), the steps occur at odd thicknesses and are most pronounced in the lower thickness range where the brightness temperature has the highest sensitivity to sea ice thickness and snow depth. Overall we expected a lower sensitivity to snow thickness, more stability of the brightness temperatures and more sensitivity to ice thickness after the retrieval we have developed and validated in Chapter 3.

A possible explanation for the spread in brightness temperature with ice thickness is the strong temperature gradient in the upper layers of. Due to the layer discretization, the strong temperature gradient causes a high contrast in temperature and thus a high contrast in the refractive index among the upper layers. This in turn causes a lower transmissivity through the layer boundaries and thus lowers the radiation leaving the sea ice. A variation in temperature profile in the upper layers therefore causes a high variability of the emitted radiation from the sea ice which is reflected in Figure 4.7.

However, with this high temperature contrast at the sea ice top while most lower layer having water temperatures (Figure 4.2), we consider the original temperature profile unrealistic and prefer the linearized profile in the following discussion.

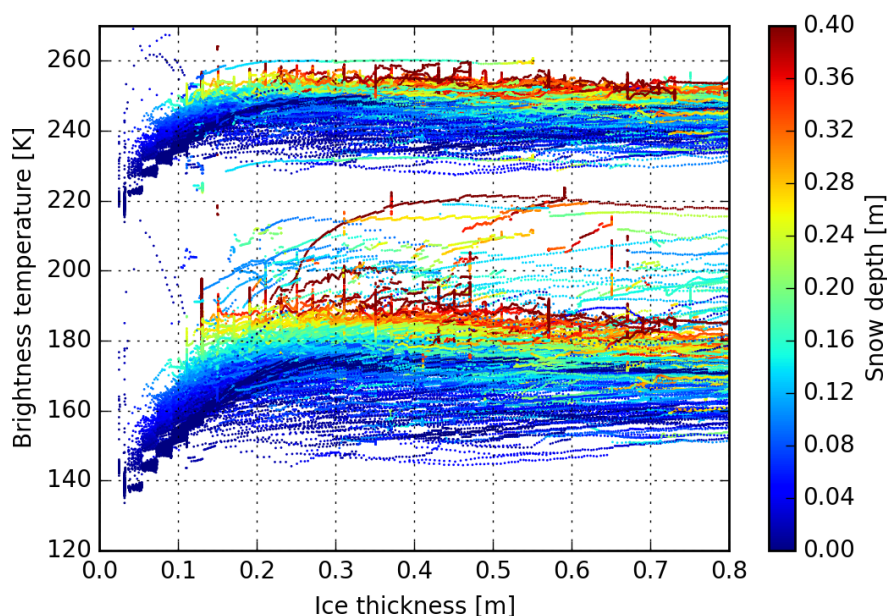


Figure 4.7: $T_{b,H}$ and $T_{b,V}$ versus ice thickness as produced by MEMLS using the temperature profile from the thermodynamic model. Snow depth is color coded.

4.2.2 Linearized temperature profile

The linear temperature profile is commonly used to describe the sea ice temperature profile in growth conditions of first year ice and seems more realistic than the original profile as discussed in Section 4.1. Since here we are not exactly interested in the sea ice evolution but in the emissivity of individual ice conditions (a single data point in Figure 4.7), we can replace the temperature profile with a linear one when modeling the brightness temperatures. This modification does not affect the energy balance model, since the profiles as input for next time step. The result is that each input profile for MEMLS is exactly the same as before except for the temperature of the layers. An example of linearized

and original temperature profiles throughout the sea ice part of the layers was shown in Figure 4.2. The resulting brightness temperatures for all simulated conditions are shown in Figure 4.8 analogous to Figure 4.7.

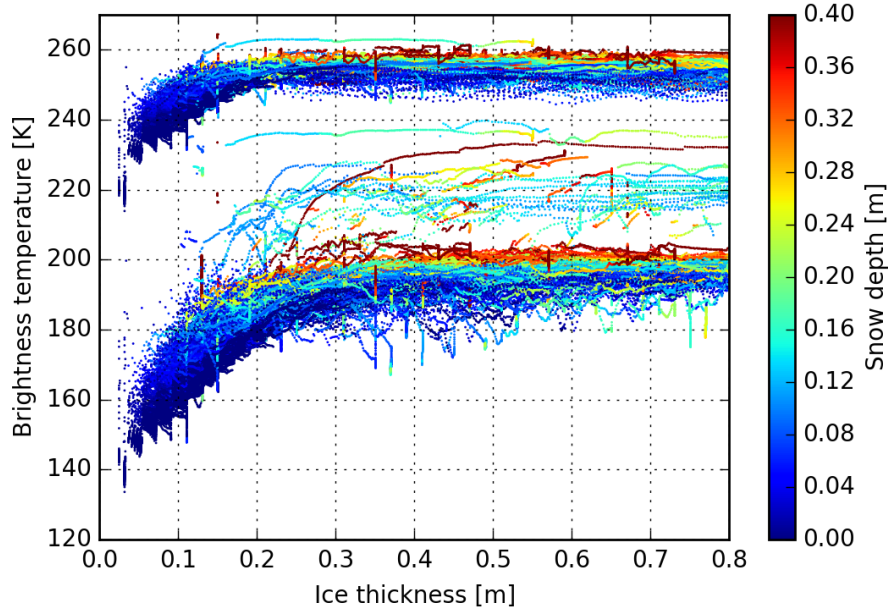


Figure 4.8: $T_{b,H}$ and $T_{b,V}$ versus ice thickness as produced by MEMLS using linearized temperature profiles. Snow depth is color coded.

Both, $T_{b,H}$ and $T_{b,V}$ show higher brightness temperatures and are much less affected by snow thickness. $T_{b,V}$ shows less variation with the ice thicknesses above 20 cm compared to Figure 4.7 while $T_{b,H}$ shows slight increase with ice higher thicknesses beyond 40 cm. For ice thicknesses higher than 20 cm in unknown snow conditions $T_{b,H}$ and $T_{b,V}$ cannot serve directly as ice thickness indicator as the snow thickness dependence is considerable in both polarizations. However, as both, $T_{b,H}$ and $T_{b,V}$ increase with snow depth at any ice thickness, the difference $T_{b,V}-T_{b,H}$ is much less effect by the snow cover and might serve as additional parameter to retrieve sea ice thickness at 1.4 GHz. The polarization difference Q is shown in Figure 4.9. Even though the highest snow thickness are found at the lowest Q of the upper branch, no pronounced dependence on snow thickness is seen. The lower branch correspond to the upper branch in $T_{b,H}$ in Figure 4.8 and yield mostly snow thicknesses above 10 cm. As only few times series are affected, we consider this as an artifact.

To note is that the linearized temperature profile is calculated over the number of layers and not weighted with the layer thickness. As a consequence, the temperature of the layers make a small jump once a new layer is created, after the last layer reaching its 2 cm limit.

This causes the different shape of the steps at low ice thicknesses between Figure 4.7 and Figure 4.8. The higher brightness temperatures in the linearized model can be explained by the smaller dielectric contrast of the layers due to the smaller temperature steps and the consequently higher transmissivities.

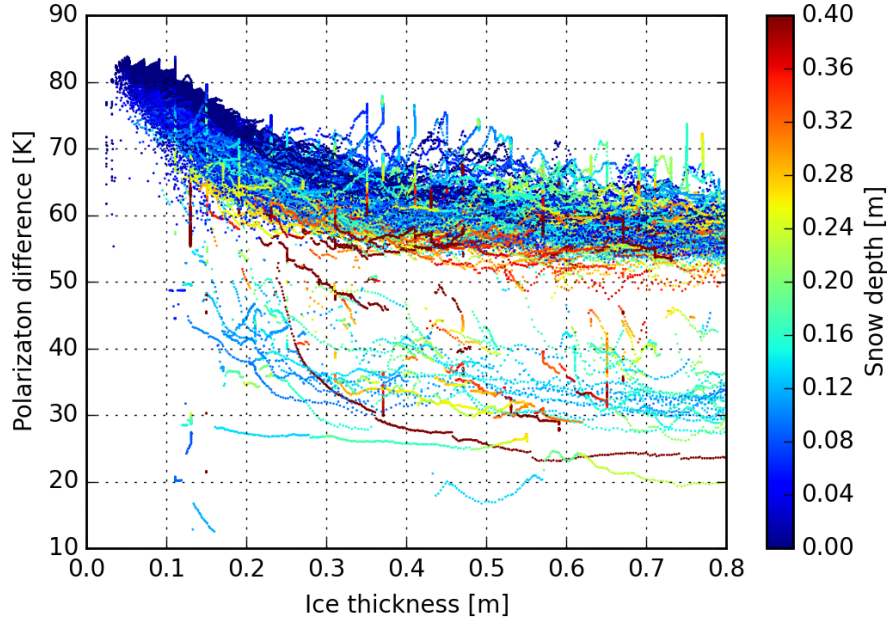


Figure 4.9: Q versus modeled ice thickness using linearized temperature profile.

4.2.3 Comparison with empirical retrieval from SMOS

In Chapter 3 we introduced an empirical retrieval for SMOS based on intensity I and polarization difference Q averaged for incidence angles of 40° to 50° . In this section we investigate how our model runs compare to real data obtained from SMOS. To match the averaged incidence angle range from SMOS, we modeled brightness temperatures at 40° , 45° and 50° and averaged the results.

Figure 4.10 shows the modeled values of I and Q versus ice thickness and the fit from the empirical retrieval. The intensity shows a large discrepancy of more than 50 K at low ice thicknesses. This can be explained by our way of the SMOS retrieval training; for the initial freeze-up we did not require 100% ice concentrations as we do not want to miss the thinnest possible ice thickness values. As the ice concentration retrieval algorithms tend to classify thin ice as lower ice concentrations [Heygster et al., 2014] we took the risk of using a combination open water and sea ice at the initial freeze-up (Section 3.1). The same applies to Q , only the discrepancy between empirical fit $Q \approx 50$ K and modeled polarization difference $Q \approx 65$ K is less. SMOS sees cold open water as $I \approx 100$ K and $Q \approx 40$ K at 40° to 50° incidence angle. This discrepancy can be explained if we assume

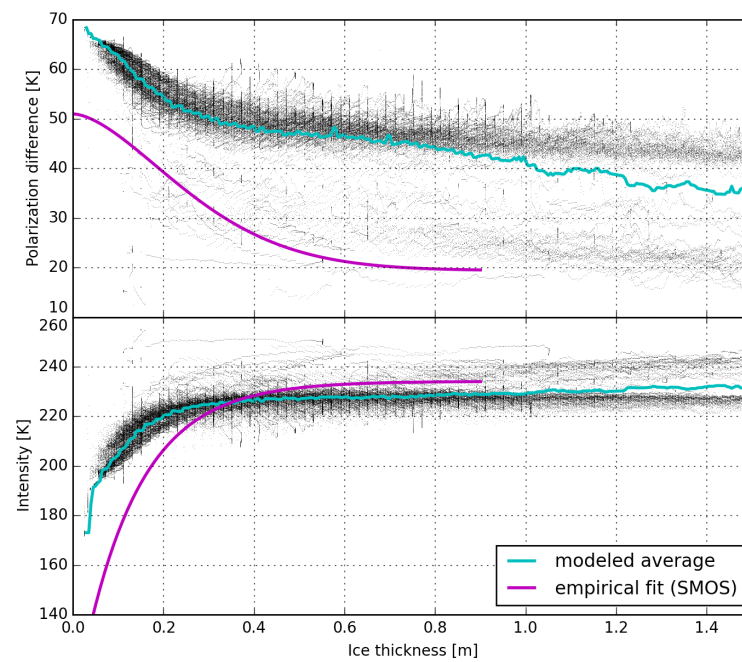


Figure 4.10: I and Q modeled mean of 40° , 45° and 50° incidence angle versus ice thickness using linearized temperature profile. Average modeled value (cyan) for each ice thickness. Empirical relation from SMOS ice thickness retrieval in the incidence angle range of 40° to 50° is shown in magenta.

that on average we trained the empirical retrieval with a certain amount of open water in the field of view of the sensor footprints. However, this does not alter this comparison in the higher ice thickness regime. At SIT around 60 cm we see a quite good agreement of model and observation in intensity at $I = 225$ K with a difference of just about 5 K. However, the polarization difference is lower by about 30 K in the empirical fit compared to the model. As the ice grows thicker, a gradually increasing split of the curves into two branches is visible. It starts at about 80 cm for both I and Q . If we extrapolate the empirical fit from the maximum SIT of 90 cm by a constant up to 140 cm the empirical fit match the modeled values at this SIT in about one third of the cases in both, I and Q . We investigate these phenomena in the detailed analysis of the energy balance model and MEMLS in the next section.

4.3 Model modifications

The model chain with thermodynamic model (Section 4.1) and emissivity model (Section 4.2) from Tonboe et al. [2011] used in this study is not able to reproduce the details in the empirical relation of SIT and intensity I and polarization difference Q . In this section the weaknesses of the individual elements of the model chain and their solutions or workarounds are discussed.

These include

- calculation of brine salinity (Section 4.3.1)
- early stop of ice growth and connection to thermal isolation by snow (Section 4.3.2)
- adding explicit ocean water salinity input parameter Section 4.3.3
- reflectivity at the ice-water interface (Section 4.3.4)
- sensitivity of the emissivity model to the sea ice layer discretization (Section 4.3.5)
- correction of errors in calculation of dielectric properties of brine (Section 4.3.6)
- handling of thin coherent layers (4.3.7)
- discrepancy between model and SMOS observations

The obvious problem of an unrealistic non-linear temperature profile was treated with a preliminary fix in Section 4.1 (Figure 4.2). A more sophisticated way to resolve the temperature profile would be to employ a heat balance equation and integrate the sea ice handling including the growth into an energy balance behavior. For simplicity, we refrain from this approach for now. Tuning the energy balance model to realistically represent ice

growth based on heat transfer while preserving empirical relations relevant for microwave remote sensing would require a more detailed investigation. We presume that the sea ice part of the energy balance model by Tonboe et al. [2011] relies only on the empirical relations for simplicity.

4.3.1 Brine salinity

During the investigations an insensitivity of brightness temperatures to salinity changes in the layers were found, when the ice consisted of many layers in the MEMLS run (not shown here). This was caused by an error in the calculation of the brine salinity which is used for the calculation of the dielectric constant of sea ice. Whenever the temperature of the layers spans over a range of -1.8°C to -8.3°C within the ice, the evaluated brine salinity takes a fixed low value for all sea ice layers of the entire ice column. This leads to lower absorption and emission of sea ice in general and to jumps in the brightness temperatures, whenever leaving or entering this temperature range. We illustrate the consequences for a sample time series of a single location for one freeze up period in Figure 4.11. While the ice is thin, the temperature within the profile does not vary beyond -1.8°C to -8.3°C . From 0.1 m ice thickness onwards the corrected brine salinity calculation results in higher brightness temperatures in $T_{b,H}$ and $T_{b,V}$. $T_{b,H}$ yields larger differences than $T_{b,V}$. At around 0.48 m and 0.61 m ice thickness, the brightness temperatures in the original model jump to the corrected one for some centimeters and then jumps back to its previous regime. At this ice thicknesses, the air temperature caused the layer temperatures of all ice layers within the column to be in the range of -1.8°C to -8.3°C so that the evaluation is correct within that range also for the original brine salinity calculation. The corrected evaluation of brine salinity is more stable and yield the correct values for each layer as can be seen from the stability of the brightness temperatures. In this particular case the effect of the correction is up to 3 K in $T_{b,H}$ and up to 1.5 K in $T_{b,V}$ while in other cases, with stronger temperature difference within the ice column we found differences of up to 7 K (not shown here). In all following model runs the corrected brine salinity calculation is used.

4.3.2 Limit of ice thickness during the growth phase

The relation of snow depth to ice thickness (Figure 4.4) shows that the ice growth modeled with the energy balance model stops in some cases at small ice thicknesses possibly due to the thermal insulation by the snow cover. This feature is not particularly important when averages of many model runs are considered and used for emissivity modeling. However, in a time series this early stop of the ice growth leads to unrealistic profiles (thick snow cover on thin ice during cold conditions) and makes the modeled SIT deviate from other models as the CFDD based model (4.6) or from in situ observations [Thomas and Dieckmann, 2009, Untersteiner, 1986].

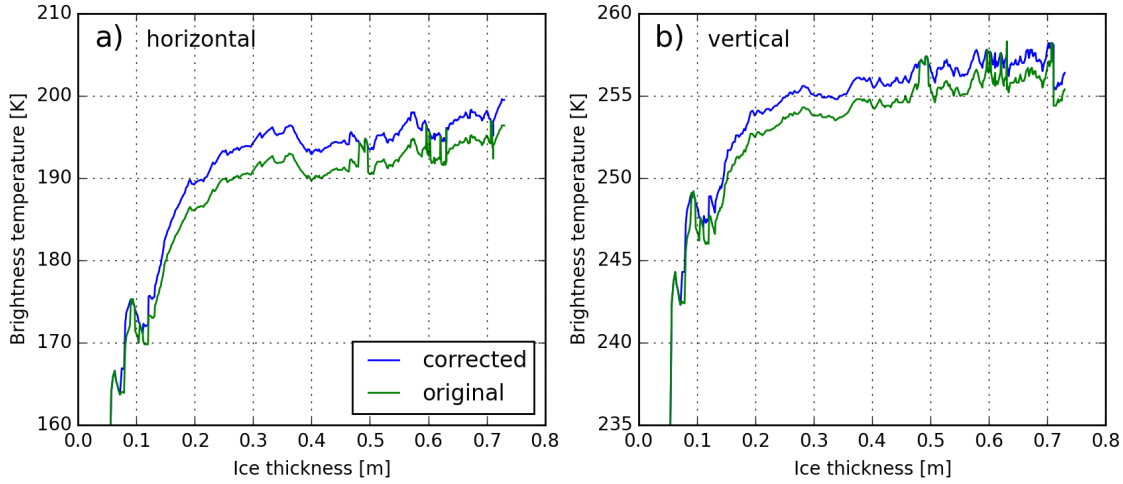


Figure 4.11: Example time series to illustrate influence of the correction of brine salinity calculation. a) shows $T_{b,H}$, b) shows $T_{b,V}$.

It turned out that the energy balance model removes layers thinner than 1 mm during generation of the snow and sea ice profile at every internal model time step of one hour. This means that in the original implementation, the ice growth rate must be at least 1 mm per hour after the lowest 2 cm sea ice layer is completed in order to create a new layer at the ice-water interface. If this criterion is not fulfilled no new sea ice layer is created and the ice stops growing. The ice growth only continues if the uppermost sea ice layer reaches a sufficiently low temperature because the ice growth is calculated from the temperature difference between the first layer and the water temperature. However, this gets more unlikely as time passes by and snow accumulates leading to higher thermal insulation and thus higher temperatures of the ice. In most cases where the ice stops growing once, no further ice growth happens for the rest of the season. This introduces the vertical lines at odd values of thicknesses in the emissivities and in the thickness comparisons (Figures 4.4, 4.6 and 4.10). Since this behavior is unrealistic, especially the discretization into 2 cm steps at odd thicknesses, we only keep the removal of snow layers smaller than 1 mm each time step and remove this restriction for sea ice layers. In Figure 4.12 the snow and sea ice thicknesses from the original model (left) and the modified model (right) and the original are shown. The discretization and terminal behavior of ice thicknesses is removed completely with this change and the mean snow depth is a more smooth function of the ice thickness. In addition, the mean snow depth is slightly higher in the regime of ice thicknesses from 0.6 m to 0.8 m.

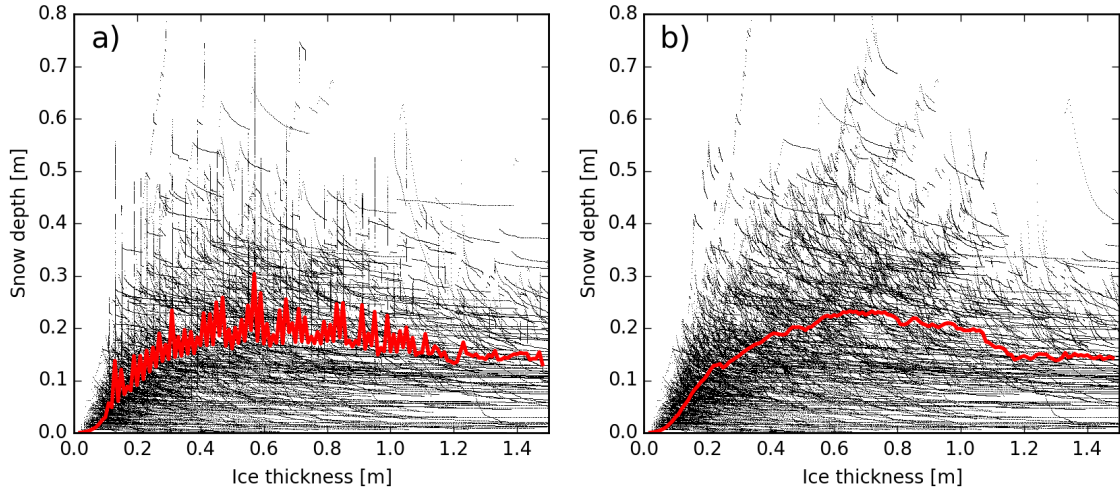


Figure 4.12: Snow depth as function of ice thickness from the original energy balance model (a) and from the model with removed 1 mm new-layer-restriction for sea ice (b). Mean snow depth for a given ice thickness is shown in red.

4.3.3 Sea water salinity as input parameter

The energy balance model comes with a fixed sea water salinity of 34 ppt. However, all empirical relations used in the energy balance model are suitable to simulate ice growth also in waters of other salinities. We made the sea water salinity an input parameter to simulate ice growth in waters with different salinity. An analysis of different salinities using this modification is carried out in Section 4.4.

4.3.4 Reflectivity of the ice-water interface

The sea ice version of MEMLS was mostly used to simulate brightness temperatures at a fixed incidence angle to match the sensor geometry of SSM/I, AMSR-E and AMSR2 [Tonboe, 2010]. Therefore, originally a database of reflectivities for the interface between water and sea ice is used in the emissivity model. To simulate the emissivity at all possible incidence angles the reflectivity has to be calculated at each incidence angle using the dielectric properties of the sea water. For the purpose of simulating arbitrary incidence angles we replaced the database with individually calculated reflection coefficients using the dielectric properties of sea water from [Klein and Swift, 1977]. This is achieved by introducing a new layer class for sea water into MEMLS and adding a thick water layer to the sea ice bottom within MEMLS. For this layer type only salinity, temperature are part of the dielectric model which should be valid for frequencies below X-band [Klein and Swift, 1977]. MEMLS treats this layer as any other layer, so that the reflectivity at the water-ice interface is then calculated from the Fresnel Equations (2.11).

Table 4.3: Influence of different Maximum Layer Thickness (MLT) compared to the final reached ice thickness for an example time series.

Maximum Layer Thickness (MLT) [cm]	Final ice thickness [cm]
1.0	50.5
2.0 (reference)	31.8
3.0	27.9
4.0	27.0
5.0	21.4
10.0	19.8

4.3.5 Influence of maximum layer thickness

The energy balance model generates 2 cm thick layers as input for the microwave emission model. As this choice seems arbitrary, we try different values and investigate the influence of this maximum layer thickness on the development of ice thickness within the energy balance model and the brightness temperatures returned from MEMLS. The ice growth within the energy balance model is calculated from the temperature difference between the top and the bottom layer. As all layers are in thermal contact with each other a change of the maximum layer thickness may influence the total ice thickness. We chose a sample time series of atmospheric data and try different Maximum Layer Thickness (MLT) values. The result in Table 4.3 shows a strong, but irregular decrease of ice thickness with increasing MLT, most pronounced at small MLT. The difference in final ice thickness between 2 cm and 4 cm MLT is less than 20%. However, MLT of 1 cm and 2 cm show about 19 cm or 60% of the reference final ice thickness with 2 cm MLT.

With different MLT, also the output of the microwave emission model changes. To compare the influence on the microwave emission, 4 cm, 2 cm, and a random MLT for each layer of 1.5 cm to 2.5 cm for a full run on all simulations described in Section 4.1 is performed. The run with random MLT is performed to ensure that the effects seen in the microwave emission does not originate from the fixed thickness relation of the layers.

Figure 4.13 shows the comparison between the default of 2 cm (a), 1.5 cm to 2.5 cm (b), and 4 cm (c) Maximum Layer Thickness (MLT) which are addressed as MTL2, MLTR, and MLT4, respectively. The SIT is less densely populated at higher SIT as the simulated first year ice did not grow to that thickness with the given atmospheric conditions in the half year of simulated freeze up. As the ice growth in MLT4 is less than in MLT2 or MLTR, even fewer cases reach higher SIT in MLT4.

MLT2 and MLT4 yield different I and Q variations with SIT in the lower SIT regime while at higher SIT, both look similar. At low SIT the spread of simulations in MLT2 and MLTR is small in I and Q while in MLT4 a split into two branches occur; between 0 cm and 20 cm a cluster of points in I at 140 K to 160 K and in Q at 65 K to 70 K is visible which is not present in MLT2 and MLTR. From SIT of 30 cm to 40 cm another split is

visible in I and Q reaching a difference of about 10 K in I and 20 K in Q . The empirical fit from SMOS observations (magenta) is closer to the lower branch in Q and lies between the branches in I . In the MLT2 and MLTR simulations there is no distinct SIT where the split between I and Q occurs. The transitions between the two branches seem to be distributed over a large range of SIT values. At higher SIT a split is still visible, especially in Q . A jump in Q can also be seen in MLT4 from the cluster of points around 65 K to 70 K at SIT of 0 cm to 40 cm.

All these strong jumps in Q fall together with moderate jumps in I are caused by an increase in $T_{b,H}$ coinciding with an increase in snow depth. The lower I values in MLT4 below the empirical SMOS curve at around 140 K to 160 K remain unexplained at this point.

In conclusion, we see a large difference between MLT2 and MLT4 and both yield explainable features on one hand and unexpected features and large differences to the empirical fit from SMOS data on the other. This gives the impression that the emissivity model has a general, not yet definable problem with the output from the energy balance model. MLTR and MLT2 yield similar results over the whole SIT range. Additionally, MLTR has none of the features of MLT4. We conclude therefore that the fixed layer thickness is not the cause of the problem for the emissivity model. However, Figure 4.13 gives the impression that there can be a threshold in maximum layer thickness from which on the modeled emission is more scattered.

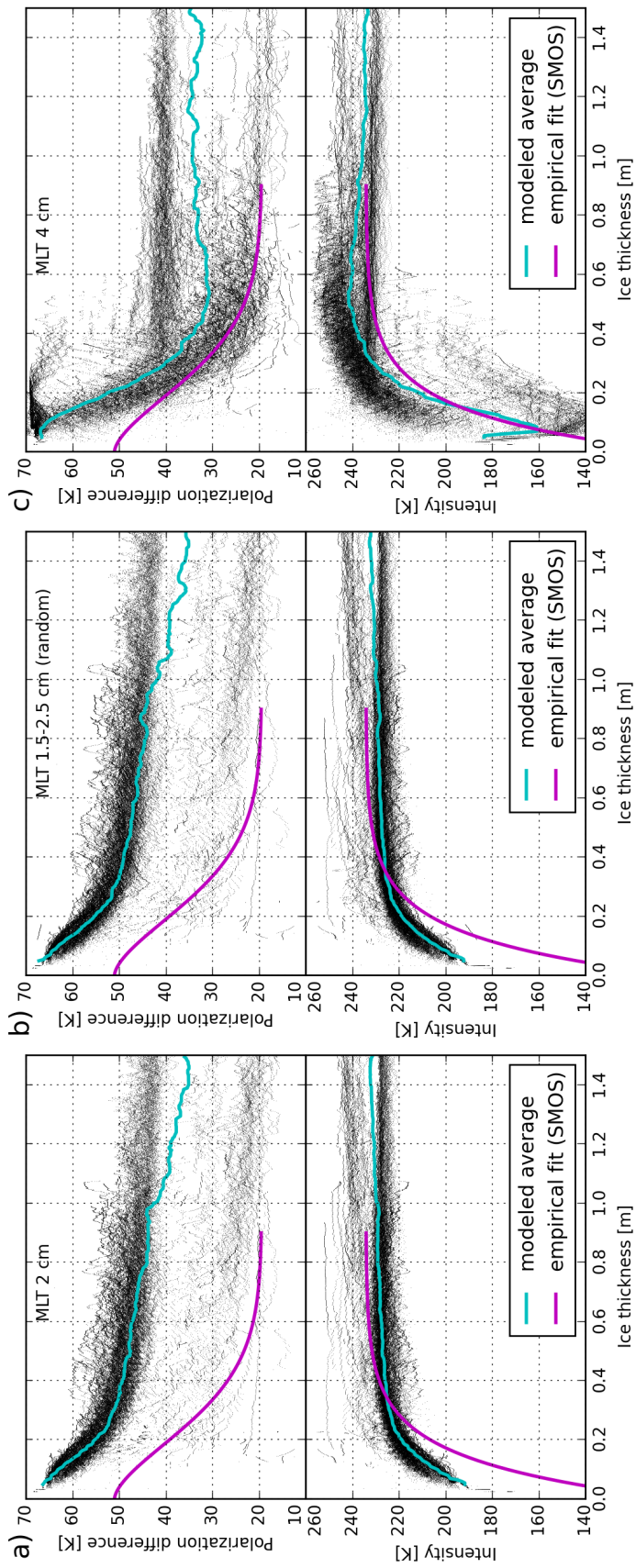


Figure 4.13: Comparison of different maximum layer thicknesses as input for MEMLS. (a) 2 cm (MLT2), (b) random 1.5 cm to 2.5 cm (MLTR), (c) 4 cm (MLT4). Otherwise each analogous to Figure 4.10.

4.3.6 Correction of dielectric mixture models

The dielectric mixture model for frazil ice used in MEMLS as developed by Polder and van Santeen [1946] and reviewed and validated for sea ice application by [Shokr, 1998] gives relatively high permittivity and loss. Even though, still inside the boundaries calculated from the analytical continuum method by Mills and Heygster [2011b], the permittivity and loss yield higher values than all mixture models, empirical formulations and the permittivities calculated from the Strong Fluctuation Theory (SFT) in the review of [Mills and Heygster, 2011b]. A review of the underlying formulas for the brine dielectric properties revealed deviations from the literature resulting in increased loss calculated within the mixture models in MEMLS. The differences are highlighted in the detailed formulas given in Appendix A.1. After the correction, the mixture model was able to reproduce the results for the frazil ice model for 5 GHz from [Shokr, 1998] (not shown here). The refractive indices calculated from the corrected frazil ice model for 1.4 GHz for the temperature range of -15°C to -1°C was shown in Figure 2.1. The mixture model for spherical inclusions, used in MEMLS for scattering calculations, also uses the brine dielectric properties. However, the effect on this mixture model was much less pronounced compared to the frazil ice model due to generally lower loss values. This correction translates mainly in lower imaginary part of the refractive index and thus to smaller absorption and emission in the sea ice.

4.3.7 Handling of thin coherent layers

MEMLS handles coherent layers in a way that deviates from a classical radiative transfer model. In MEMLS a layer is defined as a coherent layer if the condition of

$$2P_j < 3\pi/2 \approx 4.71 \tag{4.1}$$

is fulfilled, where P_j is the one way phase change within layer j as defined in Equation (2.15). Here, a simple check is performed which kind of layers fulfill this criterion. An estimation of the refraction indices of a warm, possibly snow covered sea ice from Figure 2.1 and for the snow cover from Figure 2.4 is taken and the local incidence angle θ by Snell's law for a satellite observation angle of 50° is calculated. For different example thicknesses result is shown in Table 4.4.

According to the Equation (4.1) all sea ice layers generated by the original energy balance model with $d = 1$ cm for start layer and $d = 2$ cm for the other layers are treated as coherent by MEMLS for 1.4 GHz

The details of MEMLS treatment of coherent layers is given below as needed for interpretation of the results. In the following discussion a layer is called *thin* if $2P < 4.71$ otherwise it is *thick*. MEMLS does not take the layer stack in its original form as it comes from the thermodynamic model, but reprocesses the layer stack to account for thin layers.

Table 4.4: 2P criteria check for warm sea ice, refractive index taken from Figure 2.1 for sea ice top at $S \approx 22$ ppt and $T \approx -7^\circ$ and sea ice middle at $S \approx 6$ ppt and $T \approx -4^\circ$ and from Figure 2.4 for snow with a density of about 280 kg m^{-3} . Propagation angle θ and phase change P for an incidence angle of 50° .

layer type	n	$d[\text{cm}]$	$\theta[^\circ]$	2P	coherent
sea ice (top)	3.2	1	13.9	1.9	yes
	3.2	2	13.9	3.7	yes
	3.2	4	13.9	7.4	no
sea ice (middle)	2.4	1	18.6	1.4	yes
	2.4	2	18.6	2.7	yes
	2.4	4	18.6	5.4	no
snow	1.2	1	39.6	0.6	yes
	1.2	5	39.6	2.8	yes
	1.2	9	39.6	5.0	no

This so called *layer reduction* procedure searches for thin layers in the layer stack and consecutive thin layers are joined together and their properties are averaged, weighted by their phase P from top to bottom. Single thin layers between thick layers are not modified. The reflection coefficients between the layers of the resulting layer stack is calculated again as neighboring layers may have changed their dielectric properties due to the joining process. At this point the layer stack may still contain thin coherent layers if (a) they were single thin layers between thick layers, or (b) the consecutively joined thin layers together are still thin. These layers are treated as coherent layers using Equation (2.14). The properties of the thin coherent layer is then exclusively represented by the modified interface reflection coefficients of the adjacent thick layers. For this combined interface reflection coefficient only the real part of the refractive index is taken into account. This is a good approximation for thin layers where absorption can only be very small due to the short path length through this layer. This layer reduction procedure makes MEMLS sensitive for the layer thicknesses and discretization. As the phase P and thus the criterion $2P < 4.71$ depends on the propagation angle this layer reduction depends on the incidence angle. Therefore, layers treated as coherent under high incidence angles may be treated as incoherent at smaller angles. The details of the layer reduction are not entirely transparent in the original documentation of the MEMLS model [Mätzler and Wiesmann, 2012], so it was inferred from the source code.

Considering this procedure helps to explain the large difference between MLT2 and MLT4 in Figure 4.13. In MLT4 the middle sea ice layers are thick layers and thus are not affected by the layer reduction procedure of MEMLS. In the default MLT2 model run, all sea ice layers get reduced to one single layer with properties averaged and weighted with the phase.

The snow cover as generated by the energy balance model is not discretized into layers of fixed thickness. From Table 4.4 we can see that a single snow layer of density 280 kg m^{-3}

have to be at least 9 cm thick in order to be treated as a thick layer under 50° incidence angle. Due to the snow pool feature, a single snow layer of that thickness can be generated by the energy balance model (Section 4.1). However, if no such a thick layer is within the snow pack on top of the sea ice, all snow and sea ice layers are joined together and expressed by one single layer for the MLT2 case. Effectively MEMLS runs as a three layer model in this case: water, the joint ice and snow with averaged properties, and air. With these insights the result of MLT2 (Figure 4.13 left) is more easy to understand; The main branches in I and Q show the cases when all snow and sea ice layers get joined to one single layer. The quite small variabilities within these branches then results from the variability in the average dielectric properties of these joined layers. The second branch is a result from strong snow fall events is some rare cases forming a thick snow layer which is not reduced by MEMLS.

In case of MLT4 with thin snow layers, the layer reduction procedure combines all snow layers together with the 1 cm thick top sea ice layer. The thickness of the snow cover dominates the averaged dielectric properties of the joined layer. This strongly influences the reflection coefficient of this layer and introduces a large variability of the resulting brightness temperatures (Figure 4.13 right). Most sea ice layers below do not get merged. The only exceptions are cold cases where the lower refractive index causes $2P < 4.71$ (Figure 2.1 and Table 4.4).

There is another side effect of the current method of layer merging. The scattering properties are calculated depending on the layer type. However, within the MEMLS layer reduction procedure, the properties of the different layer types get averaged during the layer merging process, even if they are of different type. This includes the type flag itself, so that type specific scattering parameters are not evaluated as a floating point type flag is not expected within MEMLS. A mechanism to calculate scattering properties for mixed layers (single layers of composite types) is not implemented. This causes errors as soon as different layer types are mixed as no type specific scattering is evaluated for the resulting layers. As the volume scattering is negligible in L-Band, this error in calculation of scattering does not introduce additional uncertainties at L-band. However, it would do so at higher microwave frequencies where volume scattering is more pronounced.

There are some options to treat the layer merging:

- (i) modification of the energy balance model so that the output layers stack better fits to the MEMLS coherent layer handling.
- (ii) introduction of an intermediate step between the energy balance model and MEMLS to modify the layers like joining similar layers.

- (iii) modification of the layer reduction within MEMLS to combine layers of same type and similar properties to form thicker layers, preserving layer types.

We discuss the advantages and disadvantages of above possibilities in more detail. The modification of the energy balance model, so that its output fits better to the coherent layer handling of MEMLS (1) has the advantage that MEMLS can remain unmodified. However, this would restrict the possibilities for input to MEMLS as the input layer types have to be of certain thickness in order to be kept by MEMLS, and would require the border layer thicknesses to be thick, i.e., the top sea ice layer must be thick in order to not get combined with the snow cover and introduce an unsupported mixed type layer. The problem with mixed type layers applies to the possibility of adding a routine before the layer reduction in MEMLS (2).

We decided therefore to modify layer merging scheme (3). The new algorithm works the following way: Layer by layer is checked if it is thick or thin ($2P > 4.71$ or $2P < 4.71$). If it is thick, the layer is kept unchanged. If it is thin, the layer properties are collected in a pool. The content of the pool is combined with the next layer if it is thin, weighted by each phase P . If the next layer is thick, the pool is expelled as one layer. When the combined thin layers in the pool form a thick layer, a new layer is created. If the next layer is of different type, the content of the pool is expelled as one layer. In addition, the saline sea ice surface layer is preserved. The original MEMLS layer reduction would combine this layer with the layer below and average their properties leading to unwanted effects.

At this point there are two possibilities for the radiative transfer calculation within MEMLS with the new layer discretization. Either the thin layers are kept as incoherent layers in order not to deal with the strong coherence effects, or the original behavior of MEMLS. The latter means calculating the coherent reflectivity for thin layers for a phase difference of $2P < 4.71$ with the new created layer discretization while preserving the saline sea ice surface regardless of the phase.

Incoherent version

To run MEMLS in the incoherent mode, no further modifications are needed since the original layer reduction was already replaced by the modified version. The incoherent mode changes the original characteristic of MEMLS drastically with surpassing MEMLS' handling of coherent layers.

However, when representative results for comparison with satellite data with only a few model runs are desired, the incoherent MEMLS simulations may be more appropriate as no coherent oscillations occur. This issue will be addressed later in Section 5.2.

The incoherent MEMLS simulations and the comparison to the empirical SMOS retrieval are shown in Figure 4.14. At high SIT, the model agrees well with the empirical retrieval in I and Q . Differences at lower SIT values might be affected by open water

influence on the empirical retrieval (Section 3.1.1). The individual profiles show a jump in Q of about 20 K to 40 K at some point along the SIT axis. At lower SIT there is a large variability of I and Q . At 20 cm SIT the I ranges from 170 K to 235 K, reaching up to the saturation value of I with SIT. The only variations at a fixed SIT in the individual profiles are temperature, salinity and the properties of the snow cover. The small branch of points at higher Q and narrow branch at I of 220 K stem from bare ice cases. This effect was also discussed by Maaß et al. [2013, 2015a] using an incoherent radiative transfer model and in comparison with the original sea ice version of MEMLS.

The relatively high starting value at an intensity of $I = 180$ K originate from the high refractive index of the warm saline sea ice layer. The further decrease of brightness temperature with increasing ice thickness in the lower branch originate from a slight increase in temperature of this upper layer even though the air temperature is colder. This is probably an artifact caused by the coupling between the energy balance model and the atmospheric model as the exact time step when the sea ice is has to be added is not defined. The increase in temperature after ice formation causing higher refractive indices leading to lower transmissivities through the ice-air interface and thus lower brightness temperatures.

MEMLS was originally developed for alpine snow where the loss is generally low. For sea ice, especially for warm, saline, frazil ice, the loss is quite high and needs to be considered for the calculation of the reflection coefficient Orfanidis [2014], Ulaby et al. [1981]. Figure 4.15 shows the same data as Figure 4.14 but with MEMLS using permittivity and loss for the calculation of the interface reflection coefficients Equation (2.9). The Intensity and polarization difference are about 20 K lower for thin ice and less than 5 K for thick ice cases compared to Figure 4.14.

In order to understand the mechanisms in the model leading to the difference between snow covered ice and bare ice and also between reflection calculated from permittivity only and from permittivity and loss we consider an example of transmissivity through an ice-air interface with and without snow layer. From Figures 2.1 and 2.4 the refractive indices for a sea ice top layer with the starting condition of the energy balance model with $T = 269$ K and $S = 22$ ppt a snow layer with $\rho = 280$ kg m⁻¹ and air are taken. The modeled transmissivities for both cases are shown in Figure 4.16. The full lines are calculated using only permittivity, while the dashed line shows the transmissivity calculated from permittivity and loss. In the bare ice case (blue) transmissivity is lower at low incidence angles for vertical polarization (upper branch) and is consistently lower for horizontal polarization for all incidence angles compared to snow covered sea ice (red). For sea water, the transmissivity is much lower, resulting in lower brightness temperatures at 1.4 GHz. The transmissivities of bare (blue) and snow covered (red) ice at vertical polarization are crossing near 50° incidence angle at the Brewster angle for the interface between snow and air (circles in Figure 4.16). We see that the insertion of the additional snow layer with a refractive index between that of ice and air increases the transmissivity for vertical polar-

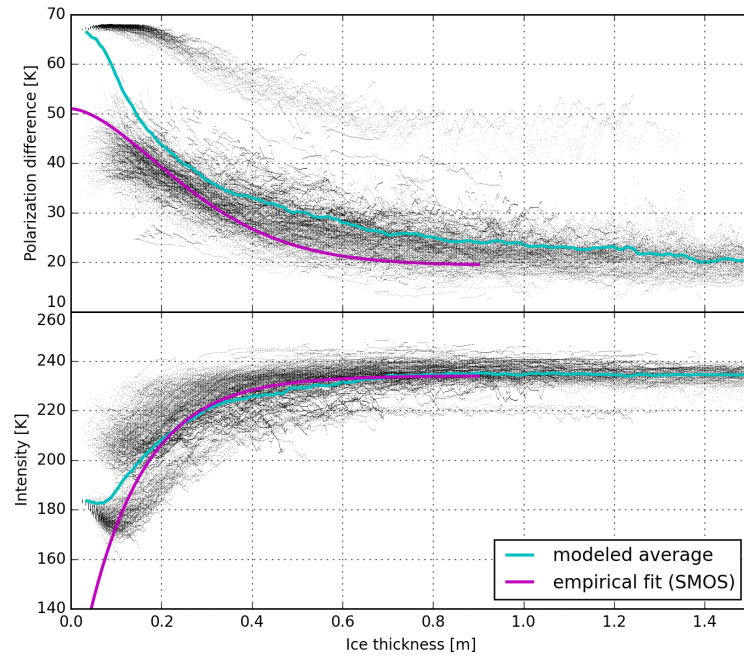


Figure 4.14: MEMLS run with modified layer reduction algorithm and comparison with empirical relation from SMOS observations. Otherwise same details as Figure 4.10.

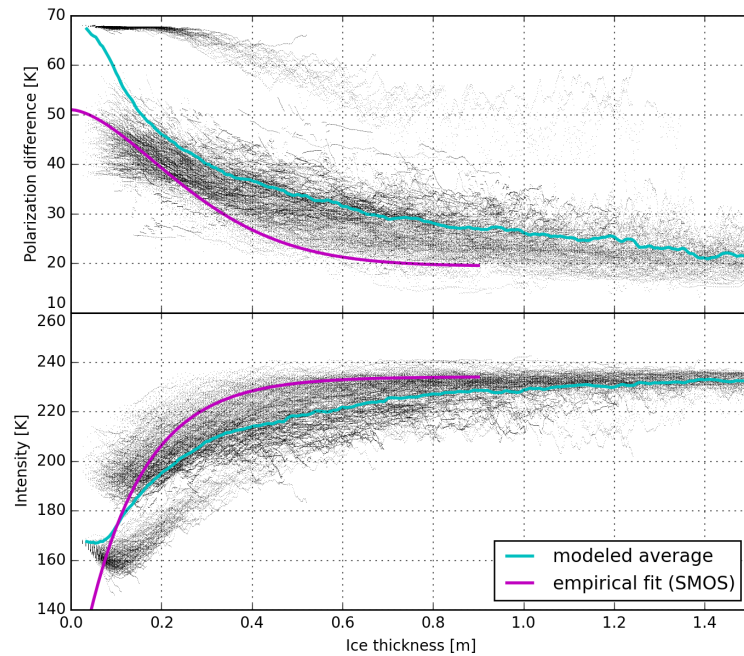


Figure 4.15: MEMLS run with modified layer reduction algorithm and using the complex permittivity for calculation of the reflection coefficient. Otherwise same details as Figure 4.10.

ization at incidence angles below 50° and for horizontal polarization for all incidence angles.

The use of the complex permittivity for calculation of the reflection at the interfaces makes a difference for the saline warm frazil sea ice of up to 20 K in brightness temperatures as can be read from the right scale in Figure 4.16 showing the transmissivity multiplied by the physical temperature of the ice ($T = 269$ K) which gives approximately brightness in case of high absorption, i.e., small penetration depth.

For warm saline ice layers the penetration depth is very small as can be calculated with the imaginary part of the reflective index using Equation (2.4) as $\delta_p = \lambda(4\pi n'')^{-1} \approx 1.3$ cm. Therefore, most radiation originates from the upper sea ice layer which explains the difference in the thin ice regime between Figure 4.14 and Figure 4.15 that is entirely caused by the difference in surface transmissivity.

This reveals the importance of including the complex permittivity for calculation of the transmissivity and reflectivity. Therefore, in all following model runs, the complex permittivity is used for determination of all interface reflection coefficients.

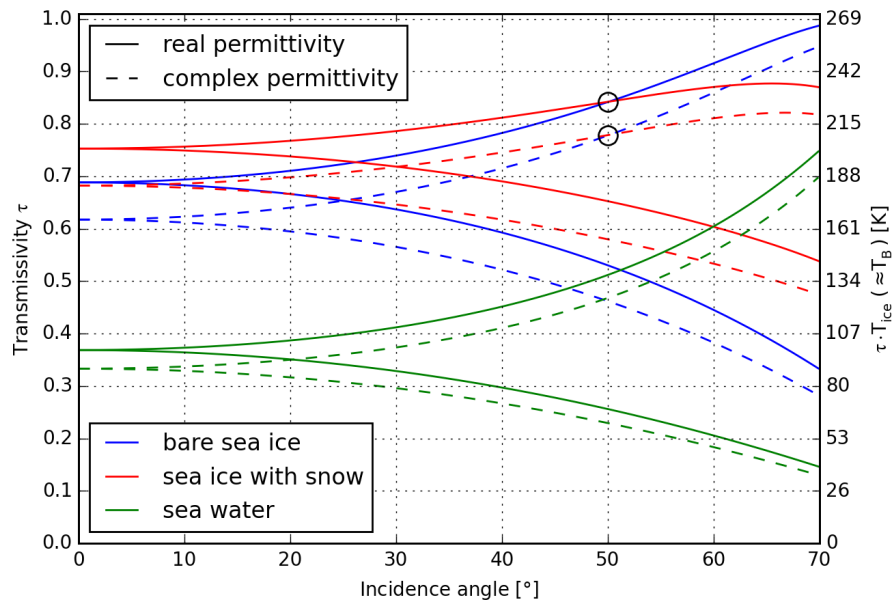


Figure 4.16: Comparison between transmissivities through the upper layer of saline frazil ice to air at an ice temperature of 269 K with and without snow for vertical (upper curves) and horizontal (lower curves) polarizations. Solid line shows the MEMLS calculated transmissivities from the real part of the permittivity, dashed line shows the transmissivities calculated from permittivity and loss.

Coherent approach

After applying the new layer reduction routine there are single thin layers left in the layer stack. Like the original MEMLS behavior we join their reflection coefficient with the layer below accounting for the phase difference using Equation (2.14).

As mentioned before, MEMLS was developed with application to snow in mind where the loss and thus the absorption and emission is small. Therefore, also calculated coherent reflection was independent of the absorption within the layer. However, for sea ice, especially with the frazil ice dielectric model, the imaginary part and thus the absorption can be high (see also Figure 2.1 and Figure 4.16). In this case even within a short distance of a phase difference less than $2P \approx 4.71$ the absorption and emission can be significant. For that reason, MEMLS was modified to also account for the loss in the thin coherent layers with the assumption that the temperature of the thin coherent layer is approximately the same as the temperature of the neighboring thick layer with which it is joined using Equation (2.14). For the application to sea ice this is a valid assumption. A more complete description of power propagation without neglecting coherence is included the model by Wilheit [1978].

The result for the MEMLS simulation with accounting for coherence effects up to a phase of $2P \approx 4.71$ is shown in Figure 4.17. A large spread of brightness temperatures is visible at thin ice thicknesses. At 10 cm, the intensities reaching from 140 K to 250 K while at higher ice thicknesses the intensity converges to about 235 K. Bare thin ice cases show intensities of less than 160 K. Once snow accumulates, the coherent oscillation starts due to the strong permittivity contrast between snow and the warm sea ice. When the snow layer becomes thick enough ($2P > 4.71$), the snow layer is taken as incoherent and the oscillations stop. However, another thin snow layer on top of the thick one can again cause coherent oscillations even though in a smaller amplitude due to the lower contrast in permittivity. That explains the convergence in intensity to about 235 K as coherence effects reduce effectively for thicker ice which is more likely to have a thicker snow cover.

4.4 Sensitivity studies

The thermodynamic model relies on strong assumptions regarding the initial ice growth and the atmospheric conditions. After having resolved some model weaknesses in Section 4.3, we now investigate the sensitivity of the brightness temperatures to freezing at different values of salinity for the ocean and the sea ice surface. As a reference point this will be compared again to the empirically trained SMOS retrieval from Huntemann et al. [2014] (Chapter 3). In addition, the relation of snow depth on sea ice to the brightness temperatures and the connected coherent oscillations are investigated. Finally, the relation of the mean penetration depth to ice thickness and surface temperature is discussed. For all these discussions all modifications of Section 4.3 are incorporated into the energy balance

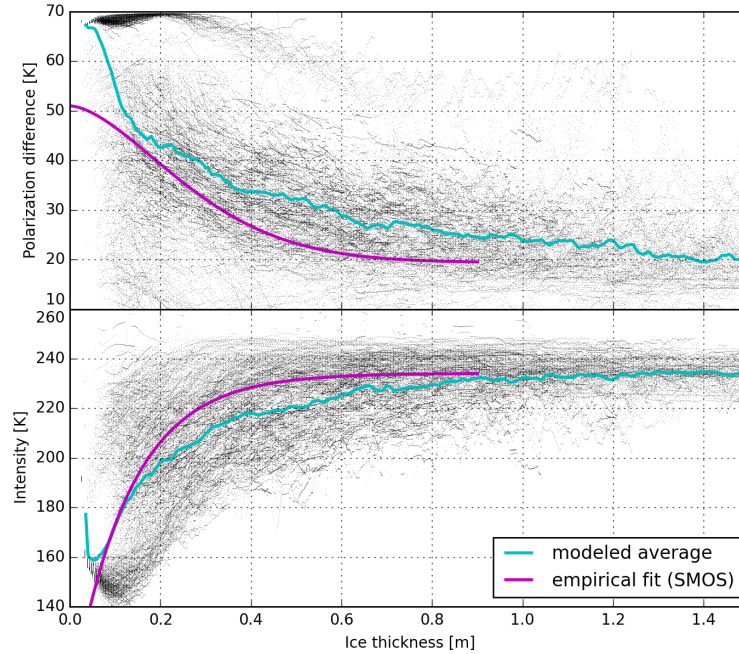


Figure 4.17: MEMLS run with modified layer reduction algorithm accounting for thin coherent layers. Otherwise same details as Figure 4.10.

model and MEMLS. All results are obtained from the coherent mode.

4.4.1 Sensitivity to salinity

Maaß et al. [2013] and Tian-Kunze et al. [2014] represent salinity of the sea ice as bulk salinity in their models. However, it has been observed that the salinity is not vertically constant, but shows a specific profile within the ice [Nakawo and Sinha, 1981, Notz and Worster, 2008]. As the dielectric properties at L-Band vary strongly with sea ice salinity [Kaleschke et al., 2013] (see also Figures 2.1 to 2.3), we investigate its influence on the brightness temperatures by varying the salinity of the top sea ice layer (the First Layer Salinity (FLS)) and the Ocean Salinity (OS) of the surrounding water in which the sea ice grows. Even though one might expect these two quantities to be correlated, it cannot be ensured that lower OS will always result in lower FLS. The FLS is additionally connected to the freezing temperature of the sea ice and to the type of ice formed. As we did not find an empirical relation between OS, FLS and temperature in literature, we model different OS and FLS values independently.

Again all atmospheric data from Section 4.1 is used to have a wide range of different condition beside the forcing of OS and FLS values. Moreover, all modifications for both models from Section 4.3 and the MEMLS variant accounting for thin coherent layers are used. In Figure 4.18 a combination of different OS and FLS is shown. Along the various plots in

x direction, FLS decreases from 22 ppt to 10 ppt while along the plots in y direction, OS increases from 22 ppt to 34 ppt.

Most changes occur along the FLS axis especially at low ice thicknesses. For OS of 34 ppt, the intensity from thin bare ice increase from 140 K to 160 K for FLS of 22 ppt up to 180 K to 200 K for FLS of 10 ppt while the polarization difference changes only slightly from about 68 K to 65 K. Also, at high ice thicknesses, the bare ice branch (lowest I and highest Q) becomes more distinct from the snow covered ice branch with decreasing first layer salinity. With increasing OS I increases slightly while Q does not change notably.

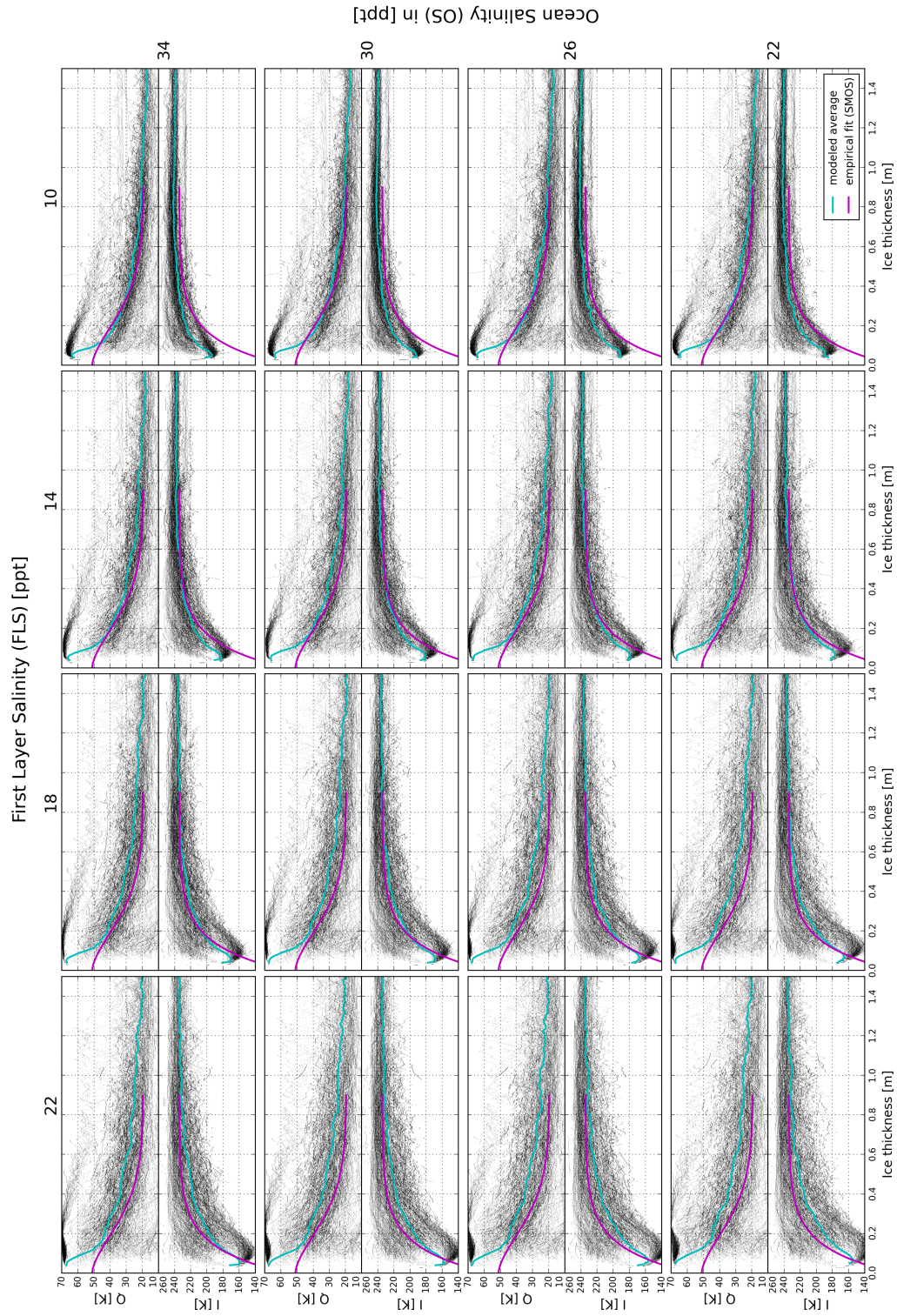


Figure 4.18: Model sensitivity to salinity changes. Decreasing first layer salinity in x -direction, increasing ocean salinity in y -direction across the plots. Each plot has the same details as Figure 4.10.

The combined average intensities and polarization differences as function of sea ice thickness for each combination of FLS and OS of Figure 4.18 are shown in the concluding Figure 4.19. Colors indicate different FLS values and line styles indicate different OS values. Also in the averages the polarization difference Q increases with FLS and show nearly no dependence on OS. With the decreasing Q the SIT increases. The intensity I decreases at all ice thicknesses with increasing FLS. With increasing OS, which mainly translates to higher bulk salinity, I increases slightly at lower ice thicknesses below 0.6 m. At higher ice thicknesses I is slightly higher, for lower OS.

Both relations can be explained by the interplay of absorption and emission and by the dielectric contrast, i.e., contrast in refractive index in the Fresnel Equations (2.11). For all ice thicknesses the contrast in refractive index between the upper ice layer and the air or snow has a major effect on the emitted radiation. The higher the FLS the higher contrast in refractive index, the lower the amount of transmitted radiation through the first sea ice layer. In the incidence angle range of 40° to 50° the effect on $T_{b,H}$ is more pronounced compared to $T_{b,V}$ leading to an increase in Q . For fixed FLS the OS has an influence as well coming from absorption and emission in the ice. Higher OS leads to higher bulk salinity which is increasing the refractive index in the ice where the imaginary part is important determining the emission and absorption. For smaller ice thicknesses, a higher bulk salinity leads to more absorption and emission and thus increase the emitted radiation. Once the radiation coming from the ocean is entirely shadowed by the sea ice, another effect prevails; the higher the bulk salinity, the smaller is the penetration depth. With a linear temperature profile in the ice, this results in lower brightness temperatures as more of the emitted radiation is coming from the upper (colder) layers. However, in Figure 4.19 this effect is only slightly visible.

4.4.2 Sensitivity to snow on sea ice

In order to investigate the influence of snow on sea ice, the default salinities for starting conditions of the energy balance model with an ocean salinity of 34 ppt and a salinity of the uppermost thin sea ice layer of 22 ppt are used.

The intensities I and polarization differences Q show a large spread at most ice thickness in our investigation. In addition, the bare ice without snow cover shows in general lower I than ice with snow cover. By comparing the incoherent run and the coherent run (Figures 4.15 and 4.17) strong coherence effects are expected to originate from the snow cover. Intensity and polarization difference from MEMLS as a function of snow depth are shown in Figure 4.20 for all modeled ice thickness values up to 1.5 m.

For a thin snow layer less than 2 cm the intensity is lower than 230 K regardless of the ice thickness which is basically the intensity for bare thick ice without snow cover. Q shows a drop from values between 50 K to 70 K to about 10 K to 20 K at the global minimum at about 4 cm to 5 cm snow depth where I reaches its maximum of 220 K to 250 K. At about

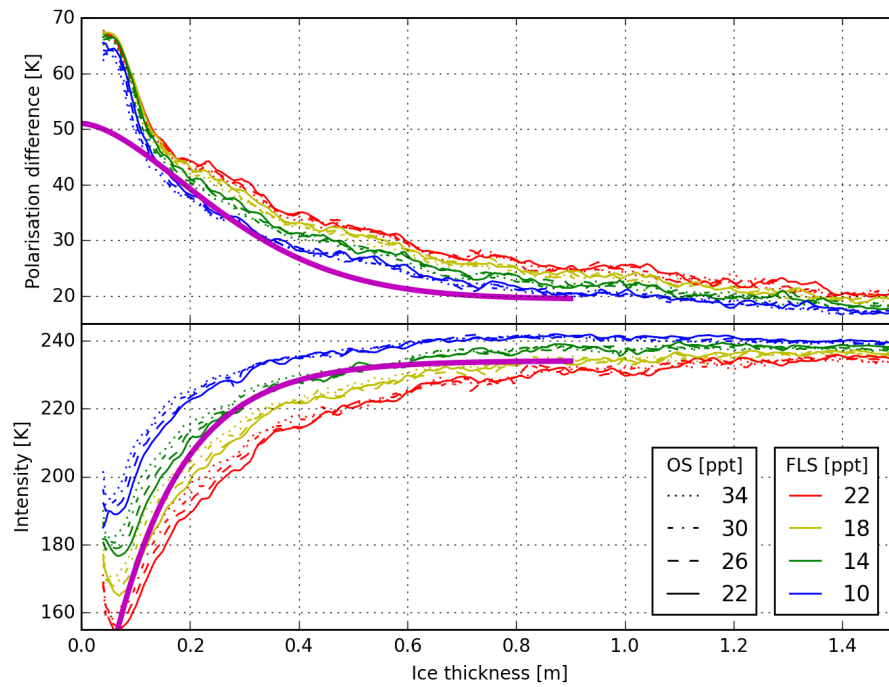


Figure 4.19: Model sensitivity to salinity, all averages from Figure 4.18.

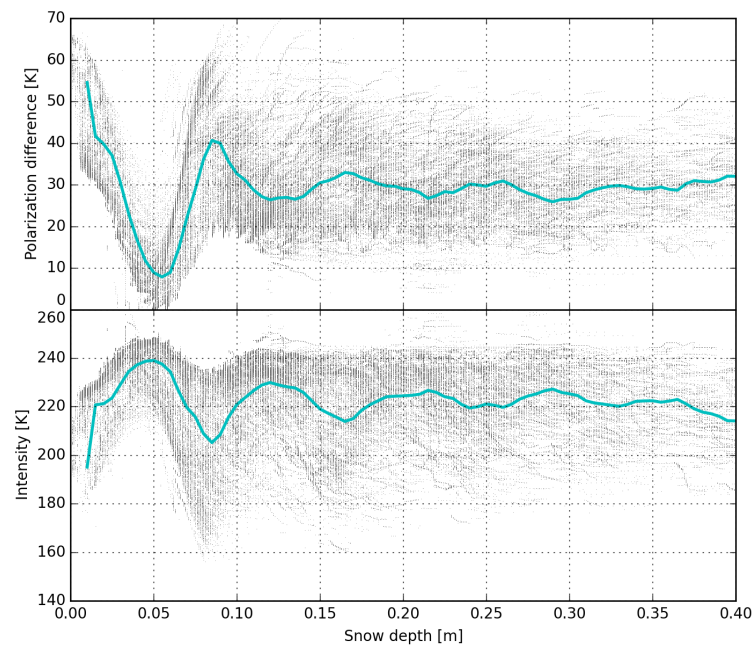


Figure 4.20: MEMLS intensity and polarization difference as function of snow thickness for all modeled ice thicknesses. The results are averaged from model runs of individual incidence angle of 40° , 45° and 50° .

8 cm to 9 cm I and Q show the largest spread right before the phase criterion $2P > 4.71$ makes the combined snow layer forming a thick layer Section 4.3.7. For further increase of the snow depth, the thin coherent layer on top does not have a sufficient contrast in permittivity compared to the existing thick snow layer to cause further strong coherence effects, so that only smaller oscillations with snow depth are visible in the averaged I and Q values.

The consequences for a satellite based ice thickness retrieval resulting from Figure 4.20 are diverse. Firstly, sea ice without any snow cover have lower brightness temperatures and shows higher polarization difference. Such distinct coherent oscillations as a function of snow depth like seen in Figure 4.20 are unlikely due to a snow depth distribution over the size of a satellite footprint. Assuming that the snow depth distribution becomes broader with increasing snow depth, coherence effects will decrease with increasing snow depth as they average out. Other studies also revealed a correlation of SMOS brightness temperatures to snow thickness up to a certain depth Maaß et al. [2013]. We will pick up the discussion on coherence effects from snow depth distributions and sensitivity to snow thickness in Sections 5.2.3 and 5.2.6.

4.4.3 Ice surface temperature and penetration depth

As an additional effect beside the dielectric contrast and resulting coherent oscillation of the snow cover, it also causes thermal insulation of the ice surface. This effect has been examined by Maaß et al. [2013] for the snow cover on the much less saline multi year ice, while here we focus on the initial first year ice formation. As before we employ the frazil ice dielectric model for the investigation. It has a high imaginary part of the refractive index (Figure 2.1), so that the penetration depth is small as a few cm. Nevertheless, we found for the simulations of frazil ice a sensitivity of intensity and polarization difference to ice thickness up to more than 50 cm on average (Figure 4.17).

Figure 4.21 shows the average surface temperatures (solid black line) for the ice thicknesses in all simulations with ocean salinity of 34 ppt, and a salinity of the first layer of 22 ppt. For each averaged surface temperature per ice thickness the transmissivity in vertical (solid green line) and horizontal (dashed green line) polarization through the first layer is calculated using the Fresnel Equations (2.11). In addition, the approximate penetration depth into the sea ice is shown in red. The penetration depth is calculated after Equation (2.4) ignoring reflection at layer interfaces. At the initial ice formation up to 0.2 m ice thickness, the ice surface temperature drops to 265 K while the transmissivities increase by about 0.1 while the penetration depth is less than 2 cm on average. At higher ice thicknesses the slope of both transmissivities decreases, but slower at horizontal polarization. From 0.3 m ice thickness onwards, a nearly linear decrease is seen in ice surface temperature, and air temperature which goes together with a nearly linear increase of the transmissivities. The penetration depth increases exponentially with the ice thickness, but

is still less than 20 cm on average for ice thickness of 1 m in our simulations.

The small penetration depth and the resulting indirect relation of brightness temperatures to ice thickness highlight the importance of proper thermodynamic modeling. With some simplifications like the linear temperature profile instead of a true energy balanced modeling of the thermodynamic processes, additional uncertainties and even artificial relations may have been introduced. In addition, the uncertainty about the dielectric properties of sea ice introduced by fixation on a single dielectric mixture model slightly limits the significance of Figure 4.21.

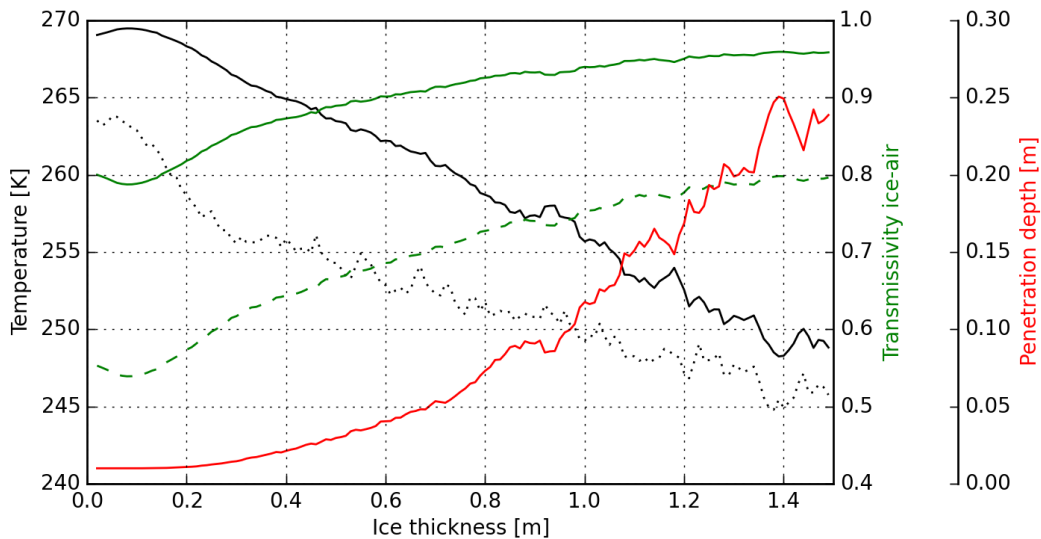


Figure 4.21: Connection of transmissivity at horizontal (dashed green) and vertical (solid green), penetration depth (red), ice surface temperature (solid black) and air temperature (dotted black) to ice thickness. The averaged quantities for all simulated time series are shown.

4.5 Summary of performed modeling

A total of 283 time series out of 18 locations over 20 years in typical first-year ice regions of emissivities were modeled. Based on the results we discussed different effects and mechanisms. Using only the frazil ice dielectric model in all simulations we experience a small penetration depth and in barely any case the radiation coming from the water-ice-interface is seen (Figure 4.21). That means the relation of measured radiation outside of the ice to the sea ice thickness is generated by other correlated quantities like snow depth and temperature. It turned out that the lower the salinity and temperature of the sea ice the more radiation may penetrate through the ice surface. Snow on top of sea ice introduces a step between the dielectric properties of sea ice and air and consequently also leads to higher

transmissivity through the interface, i.e, higher brightness temperatures. In addition, we found snow leading to coherent oscillation with the snow depth. The resulting brightness temperatures agree well with our empirically trained SMOS retrieval from Chapter 3 in both, intensity and polarization difference. However, the mechanisms behind the results differ considerably from previously discussed ones [Kaleschke et al., 2012, Tian-Kunze et al., 2014]. The major reason for this is the strong temperature and salinity dependence of the sea ice permittivity. Models considering the sea ice as one single layer with a single permittivity will be unable to resolve the complexity of the interplay between the transmissivities at the water-ice-interface, the absorption and emission in the ice, and the transmissivities through the ice top. In particular, the reflection and transmission at the interfaces may differ significantly between single layer and multi layer models. However, both are able to reproduce a sea ice thickness relation to the brightness temperatures [Heygster et al., 2009, Kaleschke et al., 2013].

Another effect is that the ice thickness is statistically correlated with snow depth and anti correlated with the probability of having a bare ice surface. This effect gives on the average of all model runs, the false impression to have a real sensitivity of SIT in Q , even at high SIT.

The energy balance model and MEMLS are implemented in MATLAB. As this is a commercial product we use the open source variant called Octave. On plain Octave as it comes with most Linux distributions the systems Basic Linear Algebra Subprograms (BLAS) package is used. However, per default this library is single threaded and many operations, especially matrix inversions are time consuming. A run of the energy balance model and MEMLS for a single combination of First Layer Salinity (FLS) and Ocean Salinity (OS) for the 283 time series takes a few days on modern hardware. To make this processing more manageable we changed the default BLAS to OpenBLAS library which is faster and multi threaded so that it makes better use of the multi core architecture of modern CPU's. This reduced the processing time to less than a day on a single computer. As not all the model modifications from Section 4.3 were investigated before the run of the salinity variation grid in Figure 4.18, many runs had to be performed. To make this more practical the Octave instance was interfaced from the Python programming language. From Python a load balanced parallel execution of Octave instances was launched over all (about 15) workstations of the network of the PHysical Analysis of RemOte Sensing images (PHAROS) group. This way the execution time reduced to about two hours for the 283 time series and made this investigation finally possible.

However, the running times are still impractical for the purpose of inversion of the emission model. On the other hand, we were able to explain basically all model results with a subset of physical effects included in the complex MEMLS model. Especially the strong side of MEMLS, the scattering and 6-flux direction propagations does not really apply in the

4.5. Summary of performed modeling

L-band simulations as volume scattering is negligible. Therefore, we investigate in more simple emissivity models for sea ice to figure out what complexity is needed for L-band simulations in Section 5.2.

5 | Follow-up on data and modeling studies

As a result of performed studies with the model chain in Chapter 4 and SMOS data in Chapter 3, valuable techniques of more effective data handling have appeared. In Section 5.1 we have a closer look into the SMOS L1C data product and introduce and compare several methods for a more compact data representation and RFI filtering.

Also, in Chapter 4 we found that the results from the complex MEMLS model can mostly be explained by rather simple physical relations. Therefore, we employ these relations as physical models as an attempt to simplify modeling at L-band while also including the investigation on surface roughness and coherence effects from snow depth and ice thickness distributions.

5.1 Techniques for SMOS data representation

The L1C data product of the SMOS satellite is the first product in the SMOS production chain to contain the brightness temperatures in a gridded format. As the satellite takes image like so called snapshots of a certain geographic point in this grid while moving forward, every point may be observed under incidence angles from 0° to about 68° during one single overflight. The SMOS satellite is in a sun synchronous polar orbit, so that the polar regions are covered most frequently with 4 to 7 overflights per day, depending on the latitude. As a result, there can be several hundred observations of a single grid point during one day for each polarization. The method to convert from the (X,Y) satellite reference frame to (H,V) earth reference frame is described in Section 2.3.

For current snow and sea ice thickness retrieval algorithms using SMOS data, a rather simple RFI filter is sufficient. Whenever a single observation in one snapshot exceeds 300 K, the whole snapshot is discarded. This leads to a large data loss of potentially unaffected data, especially in the frequent case that the RFI is not strong enough to cause ringing effects in the whole snapshot. This loss of data is not relevant on daily averages and averages over large incidence angle ranges as used by Huntemann et al. [2014], Kaleschke et al. [2012], Tian-Kunze et al. [2014] and Maaß et al. [2013]. However, if an acquisition of brightness temperatures for a smaller incidence angle range is desired or sub-daily changes are to be observed, the number of available observations is much smaller and a more careful processing is required.

For latitudes beyond $\pm 50^\circ$ on a typical day of SMOS data, there are about 40 million $(T_{b,H}, T_{b,V})$ pairs distributed over incidence angles from 0° to 68° on about 150 thousand grid points in the SMOS L1C ocean product. That results in about 260 $(T_{b,H}, T_{b,V})$ pairs per grid point on average.

We introduce, compare and review three methods handling this data in the following subsections. The methods are

- **Binning method:** (Section 5.1.1) We bin the $T_{b,H}$ and $T_{b,V}$ values to single degree incidence angle bins and use the standard deviation per bin to filter RFI and uncertainties. This method was introduced by Huntemann and Heygster [2015].
- **Exponential fit function:** (Section 5.1.2) Based on the approximate shape of the $T_{b,H}$ and $T_{b,V}$ vs incidence angle we propose a simple two parameter exponential fit function.
- **Fresnel fit function:** (Section 5.1.3) After modeling many snow- and sea ice conditions and their incidence angle dependence based on their micro physical properties in Section 4.2, we can propose a multi layer Fresnel-fit for $T_{b,H}$ and $T_{b,V}$.

Both fit methods may use an iterative method to remove outliers and in particular RFI influence. For each of these methods we will show examples on open water, thin sea ice and thick sea ice on all overflights of one day and on a single overflight of that day. We chose a location in the Laptev Sea at 74.5 N, 117 E on 1 October 2013 for open water, 27 October 2013 for thin ice, and 25 February 2014 for thick ice.

Another more complex multi stage fit approach is made in the soil moisture community as RFI is major problem for the soil moisture retrieval from SMOS in certain regions [Zhao et al., 2013, 2015]. For sea ice also polynomial fits were investigated [Maaß et al., 2013] in order to remove RFI influence and gain stability.

5.1.1 Binning method

A single overflight is sufficient to observe an area from different incidence angles as consecutive SMOS snapshots overlap considerably. We start with converting the L1C data into the earth reference frame, averaging the observations into single degree incidence angle bins and derive the standard deviation for each bin. The standard deviation is representing the variability of brightness temperatures for a given grid cell within the few seconds the grid cell is observed by SMOS under an incidence angle $\pm 1^\circ$ segment. The surface conditions will not change within this temporal scale. Therefore, if this variation is high, a non-geophysical influence on the brightness temperatures is detected and the data point is discarded. Due to the aperture synthesis step of the SMOS image generation process, RFI sources propagate in a ringing structure throughout the snapshot along specific lines. As a consequence, the values from the different snapshots of one overflight falling into an incidence angle bin of one grid cell may show a large variability in brightness temperature. As compromise between data quality and loss of data due to filtering we use 10 K standard deviation as a threshold, i.e. bins with a standard deviation above 10 K are discarded and we require at least three data points for a valid average. These values are found empirically and are reasoned and discussed on the detailed statistics of an example day, the 25 December 2010, in Figure 5.1. The upper plot (a) shows the three data point criterion in a histogram as a red line. On the left axis the number of data points is shown while the right axis shows the percentage of remaining data points when applying the data point requirement as a lower threshold. The criterion of having at least three data points is fulfilled in 63.3 % of the cases as can be read from this axis. The hatched area shows data where the criterion is not fulfilled. Some incidence angle ranges have more observations in one overflight than others because of the incidence angle distribution within the snapshot (see Figure 2.5) [Martín-Neira et al., 2002]. This causes the pronounced shape of the histogram.

For incidence angle bins with more than three data points, the standard deviation is calculated. The histogram of standard deviations of $T_{b,H}$ per incidence angle is shown in Figure 5.1 (b). The standard deviation is relatively evenly distributed over all incidence angles with a peak at about 1 K to 4 K standard deviation and 30° to 60° incidence angle. However, allowing just a maximum standard deviation of 4 K would discard about 50 % of all data. Since the radiometric accuracy of MIRAS does not vary with the incidence angle but with the position of the point within one snapshot [Khazaaal and Anterrieu, 2009, Martín-Neira et al., 2002], we chose for our application a maximum allowed standard deviation of 10 K. In the example day of Figure 5.1 (b) about 87 % of the data remain. Again, the red hatches mark the data regime not fulfilling this criterion.

A brightness temperature example of thin sea ice of 1 Oct 2010 is shown in Figure 5.2. The diagram on the left (a) shows $T_{b,H}$ and $T_{b,V}$ of the overflight at 7:36 UTC. The moderate change of brightness temperature with the incidence angle leads to a smooth

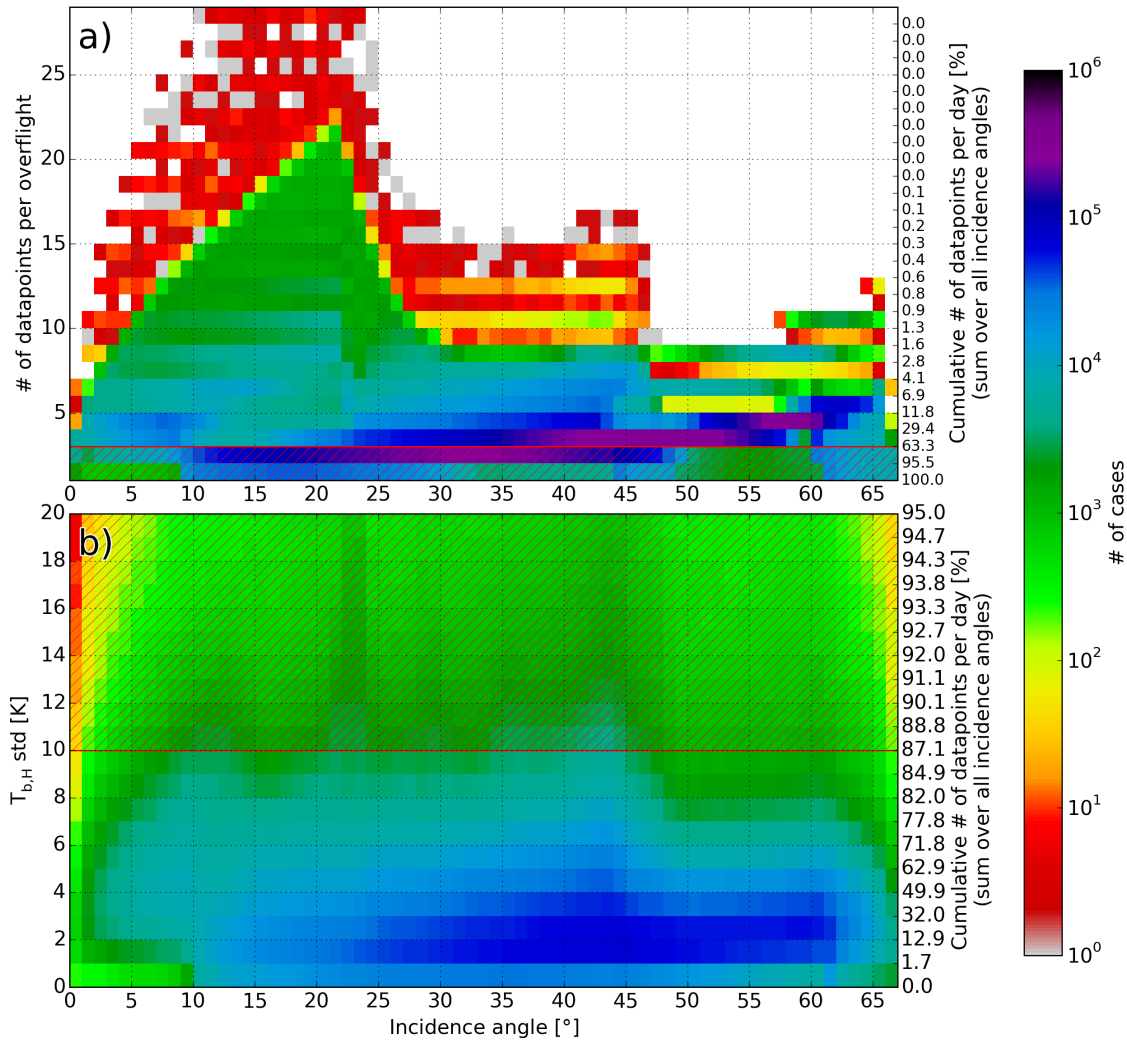


Figure 5.1: Statistical overview on SMOS L1C data higher than 50° N on 25 December 2010. The upper plot (a) illustrates the number of all observations per incidence angle bin per grid cell per overflight while the color shows the number of occurrences. The red line marks the threshold of at least three data point for a valid average brightness temperature. In the lower plot (b) the standard deviation criterion on all cases fulfilling the three data point criterion is shown. The chosen threshold of 10 K for the standard deviation is marked by the red line. Red hatched areas mark discarded data.

curve of average brightness temperatures with low standard deviations. No incidence angle bin exceeds the threshold of 10 K. In contrast, on the right (b) the result is much less homogeneous even though it is the same grid cell on the same day, but at a later overflight (12:32 UTC). The strong variations especially between 40° and 50° in $T_{b,V}$ cause high standard deviations in many incidence angle bins to exceed the 10 K threshold. An averaging of brightness temperatures will not give representative values as the strong variations are not caused by natural surface emissions but most probably by RFI.

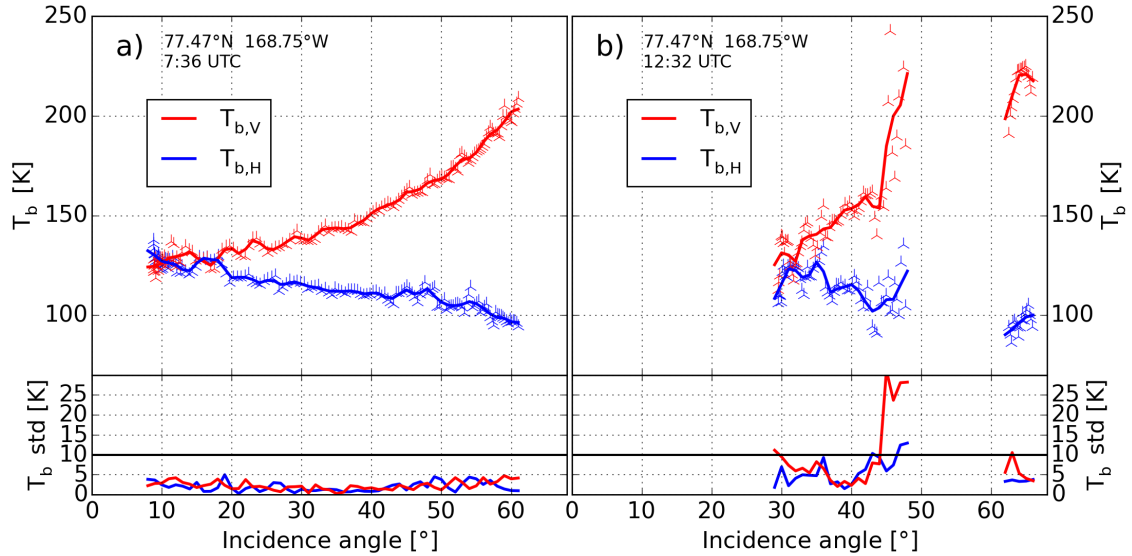


Figure 5.2: $T_{b,H}$ and $T_{b,V}$ versus incidence angle on 1 Oct 2010 7:36 UTC (a) and 12:32 UTC (b) for a location on thin sea ice. Blue ($T_{b,H}$) and red ($T_{b,V}$) λ are single observations while lines show the mean over $\pm 1^\circ$. Lower parts show the standard deviation with the black horizontal line marking the 10 K threshold.

Figure 5.3 shows the comparison of the binning method between single overflight and all overflights of one day. Plots a and b show the binning method on a sample open water point in the Laptev Sea. The RMSD is shown in the lower left of each plot. A pair of small γ (red and blue) shows an individual ($T_{b,H}, T_{b,V}$) pair. Single overflights on each surface condition (plots b,d,f) look consistent with small variations for each incidence angle bin. All overflights of one day (plots a,c,e) show a strong variation of brightness temperatures for incidence angles covered by multiple overflights. In some cases the standard deviation is above 10 K, so that no valid binned value would be returned, even though there are enough measurements like in plot c at 21°. This incidence angle regime of 15° to 25° is rather unstable in all shown plots, even within a single overflight. Another unstable incidence angle regime is around 38° to 48°. This results from the sensor geometry as discussed earlier in Section 2.3.

By only keeping average and standard deviations of the incidence brightness binned temperatures we have the potential to save storage space without losing much information.

For a daily product of binned brightness temperatures compared to the original data, we would reduce the amount of required disk space by factor of around 6.

A high frequent variability of brightness temperatures with incidence angle is not expected as the Fresnel equations do not predict such behavior for plane or statistically rough surfaces as that of young sea ice. We expect features of highly variable brightness temperatures with incidence angle to not contain geophysical information but rather originating from the MIRAS image reconstruction process. Therefore, in the next sections, we will use fit functions to represent the overall behavior of the brightness temperatures to incidence angle relation, disregarding the not geophysical small scale variations.

5.1.2 Exponential fit function

To have an accurate representation of the data, without losing much information, and in addition complete missing incidence angle segments, especially in the lower incidence angle range, we introduce an exponential fit function

$$T_{b,p}^{\text{exp}}(\theta, I_0, a, b) = I_0 - a_p \cdot \exp\left(-\frac{\theta}{b_p}\right). \quad (5.1)$$

The index p is the polarization (h or v), I_0 is the intensity in nadir observations, a_p and b_p are parameters defining the slope and curvature of the fit, θ is the incidence angle, I_0 is determined by averaging the mean of $T_{b,H}$ and $T_{b,V}$ up to incidence angles of 30° . The a_p and b_p parameters are determined minimizing the RMSD between the single observations and the curve. Except for a common I_0 , the fits of $T_{b,H}$ and $T_{b,V}$ are independent, so that a set of fit parameters for each polarization is obtained. Note that the parameters a_p and b_p of the fit function do not represent completely independent features of the brightness temperature incidence angle dependence, i.e., many combinations can fit the brightness temperatures if a limited set of observations is available as it happens for single overflights. This ambiguity makes it impossible to extract a direct physical meaning from these parameters.

Figure 5.4 is analogous to Figure 5.3, and shows in three rows from top to bottom fits of open water, thin sea ice, and thick sea ice as daily fit (left) and single overflight fit (right). The fit function performs well in all shown cases with RMSD between 3.74 and 6.59. High frequent variation of brightness temperatures with incidence angle cannot be reflected within the fit and are smoothed out (cf. $T_{b,V}$ in Figure 5.3 f and Figure 5.4 f). Therefore, the RMSD is always higher than in the incidence angle binning method. The RMSD can be higher in the early freeze up when the ice grows several cm per day or when the sea ice concentration of the observed grid point changes within one day (not shown).

For incidence angles higher than the observed ones, the fit function tend to generate

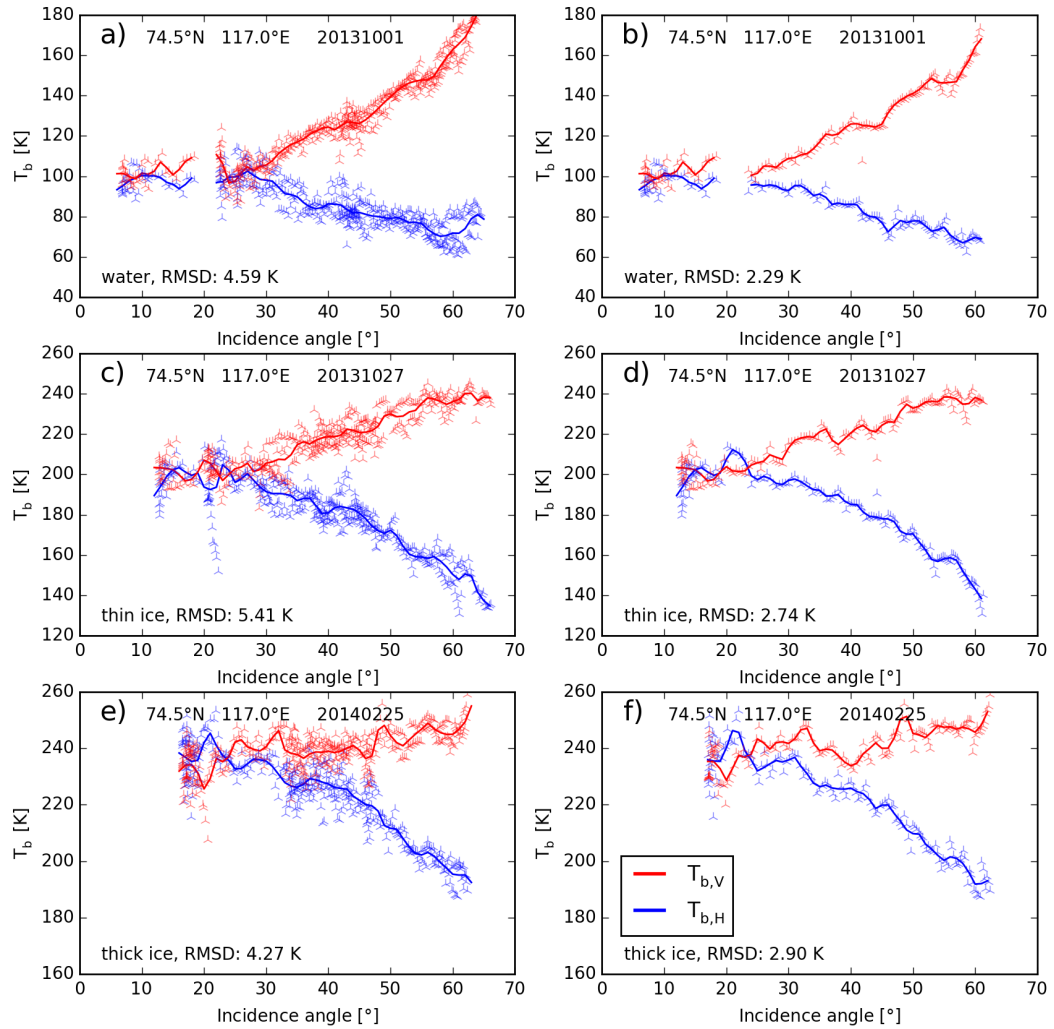


Figure 5.3: Comparison of the performance of the binning method on different surface conditions. The left column (plot a,c,e) shows the binning on daily data, while the right column (plot b,d,f) shows the binning on individual overflights of the same day. The rows show the binning on open water, thin sea ice and thick sea ice from top to bottom.

much higher polarization differences than we expect from physical understanding.

For RFI removal it is assumed that most observations are not RFI contaminated, so that fit of all data points is just slightly bent by outliers in the data. We remove 20% of the data with the highest deviation from the fit, which often hits most of the outliers and RFI influenced data points, and then perform the fit again. We repeat this procedure until a desired RMSD of 5 K is reached or the RMSD decreases by less than 1 K compared to the last iteration. This filter is not applied in Figure 5.4.

A daily product using this fit to represent the brightness temperatures - incidence angle dependence would reduce the amount of required disk space by a factor of about 100, compared to the original data.

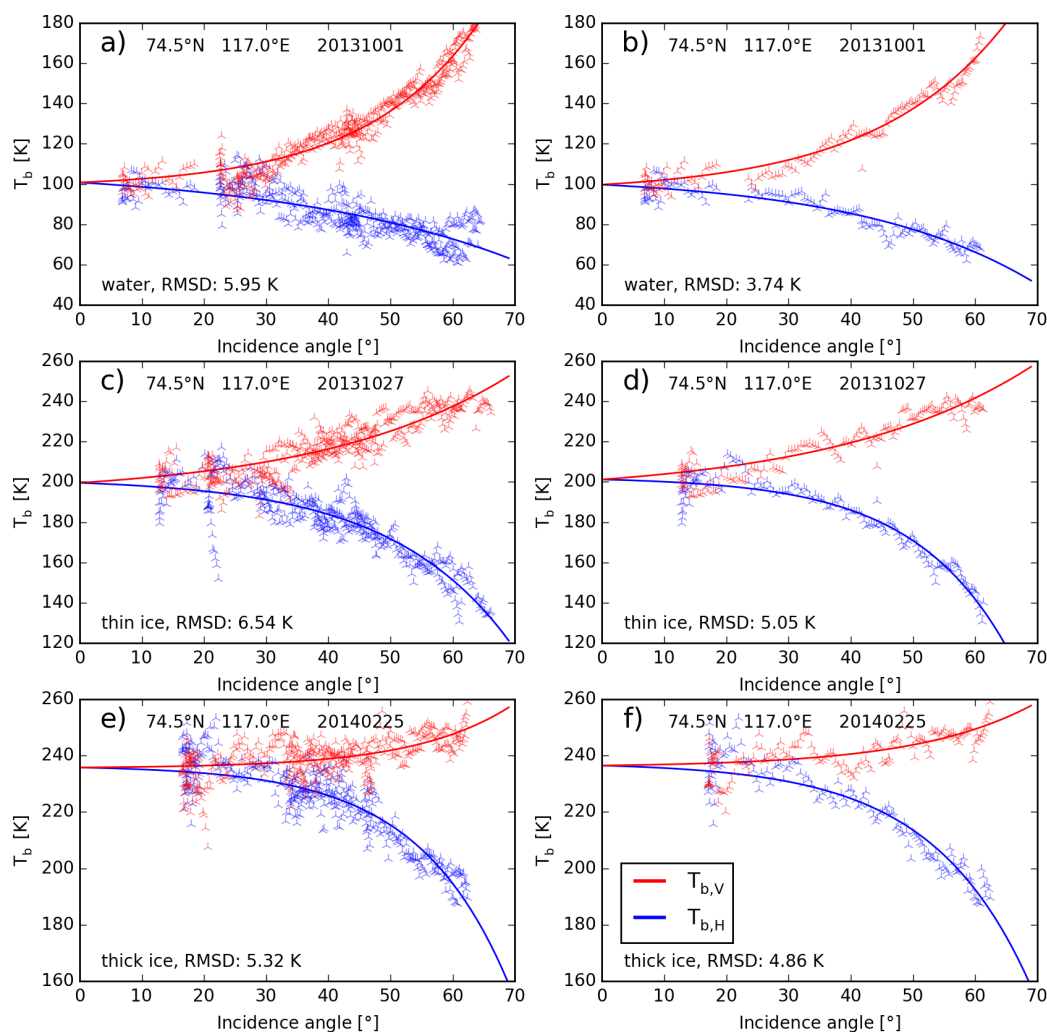


Figure 5.4: Comparison of the performance of the exponential fit on different surface conditions. The left column (plots a,c,e) shows the binning on daily data, while the right column (plots b,d,f) shows the binning on individual overflights of the same day. The rows show the exponential fit on open water, thin sea ice and thick sea ice from top to bottom.

5.1.3 Fresnel fit function

A more physical fit function than the exponential fit, would be the Fresnel equation for non-magnetic media (see Equations (2.11)). In case of many subsequent layer, we have for the transition between layers m and $m + 1$

$$R_{pm}(\theta_m, N_m, N_{m+1}) = \|r_p(\theta_m, N_m, N_{m+1})\|^2. \quad (5.2)$$

The index p here stands for the polarization, either h or v . For the transmission we have

$$\tau_{pm} = 1 - R_{pm}. \quad (5.3)$$

The product of the transmissions through the layers result in the final direct transmission¹

$$\tau_p = \prod_m \tau_{pm}. \quad (5.4)$$

As of Equation (5.2) potential coherence effects are neglected by only taking the total transmission into account. In the simplest case we have three layers: air, snow and sea ice (Figure 5.5).

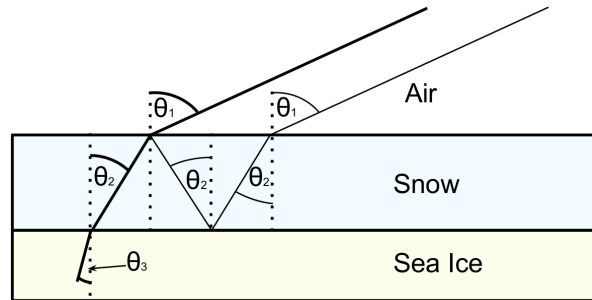


Figure 5.5: Illustration of sea ice and snow interfaces and propagation angles.

The major contribution to the measured intensity in the air medium is shown in a thick black line. The thinner line illustrates a small indirect contribution which has undergone two more reflections before transmission to the air. This results in

$$\tau_{p+}(\theta_1, N_1, N_2, N_3) = \tau_{p1}\tau_{p2}(1 + R_{p1}R_{p2}). \quad (5.5)$$

The angle θ_1 is defined by the incidence angles of the instrument. N_1 , N_2 and N_3 are then the refractive indices of the air, snow, and sea ice respectively and are addressed as N_{air} , N_{snow} , N_{ice} in the following discussion. The idea is to fit the refractive indices N_{snow}

¹we use the τ symbol instead of commonly used T for transmission to avoid confusion with temperature T

and N_{ice} for the horizontal and vertical reflection simultaneously with a nadir intensity I_0 , while $N_{\text{air}} = 1$. The nadir intensity I_0 is needed to relate the transmission coefficient for all incidence angles to the brightness temperatures to finally get the fit as

$$T_{b,p}^{\text{fr}}(\theta_1, I_0, N_{\text{snow}}, N_{\text{ice}}) = \frac{\tau_{p+}(\theta_1, N_{\text{air}} = 1, N_{\text{snow}}, N_{\text{ice}})}{\tau_{p+}(\theta = 0, N_{\text{air}} = 1, N_{\text{snow}}, N_{\text{ice}})} \cdot I_0. \quad (5.6)$$

So we have to minimize

$$\sum_{i=0}^M \left[\sum_p \left(T_{b,p}^i - T_{b,p}^{\text{fr}}(\theta_1^i, I_0, N_{\text{snow}}, N_{\text{ice}}) \right)^2 \right], \quad (5.7)$$

with respect to N_{snow} , N_{ice} , and I_0 . The outer sum goes over all measurements M to fit for one SMOS grid point, i.e., one day or one overflight, while the inner sum goes over both polarizations. As an attempt to find the global minimum in the error function the Levenberg-Marquardt method [Marquardt, 1963] is used.

Note that this is not a complete emission model and only used to fit brightness temperatures measured by MIRAS. The resulting refractive indices are considered as fit parameters in this section. The physical interpretation and analysis of these refractive indices will be discussed in Section 5.1.6.

Figure 5.6 is analogous to Figures 5.3 and 5.4, and shows in three rows from top to bottom fits of open water, thin sea ice, and thick sea ice as daily fit (left) and single overflight fit (right). The Fresnel fit gives in general similar results to the exponential fit function. At higher incidence angles and vertical polarization the results differ as a consequence of the fit function characteristics. In the thin and thick ice cases (plots c,d,e,f) the $T_{b,V}$ has a clear maximum in the fit. Compared to the exponential fit (Figure 5.4) I_0 seems shifted for the open water cases (plots a,b) towards higher brightness temperatures. The inconsistency of brightness temperatures from different overflights (plot a) in $T_{b,H}$ at 60° incidence angles promote this offset as it is not so strong in the single overflight fit. The high incidence angle observations may also contain more of atmospheric influences because of the longer path through the atmosphere [Zine et al., 2008, Maaß et al., 2013]. However, the open water case is not the target of the presented fit functions in this study. In addition, observations at higher than 60° incidence angle are close to the border of the snapshot and thus are potentially effected by other sensor related error influences [Corbella et al., 2005, Martín-Neira et al., 2002, Zine et al., 2008].

For RFI removal with the Fresnel fit we use the same method as for the exponential fit. We perform a fit, remove 20% of the data with the highest difference iteratively until a desired maximum RMSD is reached or until the RMSD difference between two consecutive iterations is less than 1 K. As expected, also for the Fresnel fit a reasonable desired maximum RMSD is turned out to be 5 K. This filter is not applied in Figure 5.6.

In a daily product using the Fresnel fit to represent the brightness temperatures - incidence angle dependence, the amount of required disk space would be reduced by a factor of about 180, compared to the original data. This is slightly more efficient than the exponential fit as the determined N_{snow} and N_{ice} are fitted for both polarizations while the exponential fit requires determination of a and b for each polarization.

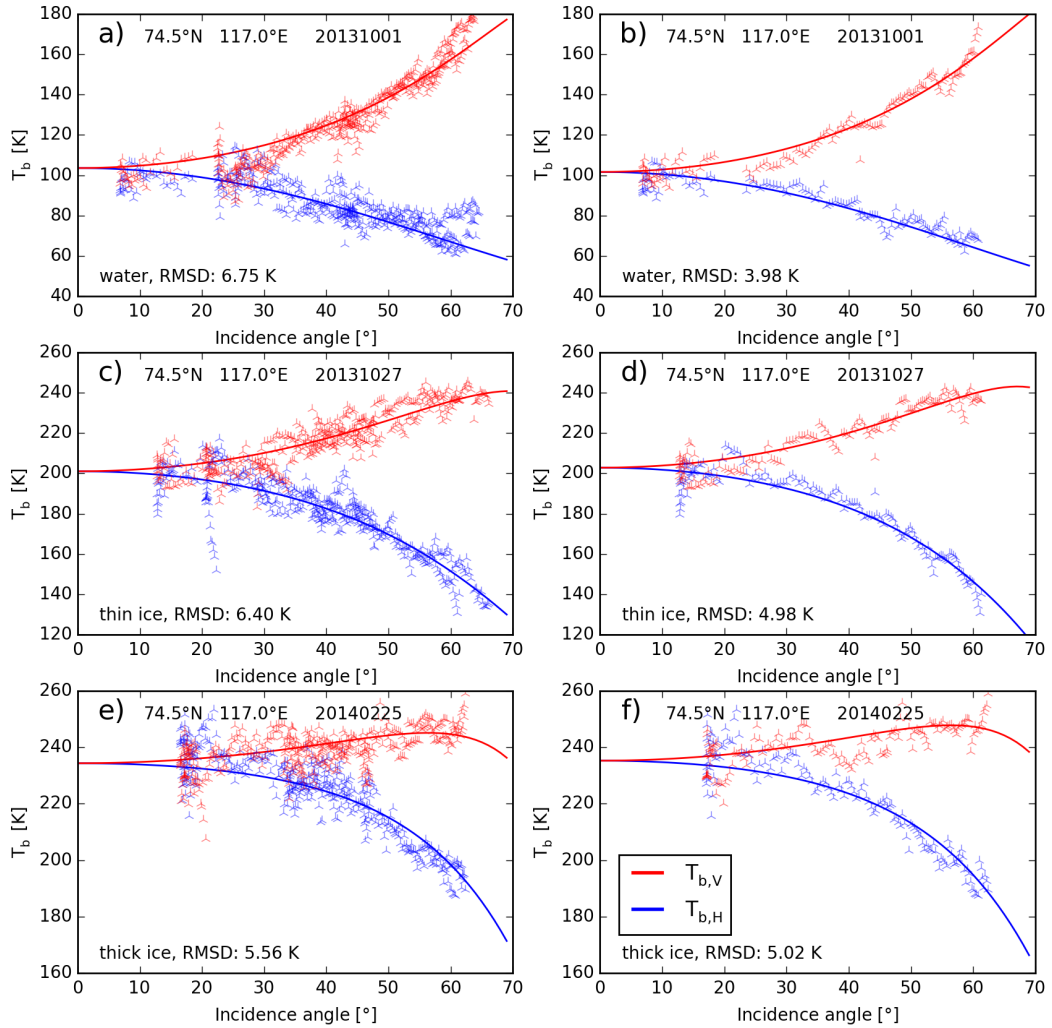


Figure 5.6: Comparison between Fresnel fit on different surface conditions. The left column (plot a,c,e) shows the binning on daily data, while the right column (plot b,d,f) shows the binning on individual overflights of the same day. The rows show the Fresnel fit on open water, thin sea ice and thick sea ice from top to bottom.

5.1.4 Comparison of fit accuracy and data consistency

To have an estimate of the quality of the different fit methods, we perform several sample fits and summarize the accuracy characteristics. We chose 1000 random grid points with

100 % sea ice concentration (according to the ASI algorithm derived from AMSR2 data) on the 28 October 2013. All areas lie between 70°N and 75°N and are at least 50 km away from the coast. For these points we perform the exponential fit (Section 5.1.2) and the Fresnel fit (Section 5.1.3) with the outlier- and RFI filter for each fit method. To estimate the spread of the $T_{b,H}$ and $T_{b,V}$ within one day, we also derive the standard deviation for each 1° incidence angle bin (see Section 5.1.1). The grid points are divided into two classes by their SMOS brightness temperature at nadir observations, $140\text{ K} < I_0 < 230\text{ K}$ and $I_0 > 230\text{ K}$, and call them thin ice and thick ice respectively (see also [Kaleschke et al., 2012, Tian-Kunze et al., 2014]).

The results for thin ice are shown in Figure 5.7. Here, the mean biases are defined as average difference from the mean value for each incidence angle bin, i.e., $T_{B,\text{mean}} - T_{B,\text{fit}}$. Hence, negative values mean that the brightness temperature at this incidence angle bin is higher in the fit function and vice versa for positive values. The half transparent tubes around the lines mark the standard deviation from the mean difference between fit and the binned values and indicates the consistency of the bias. In this investigation the RFI filtering procedure for both fit functions are used with the $< 1\text{ K}$ criterion for the RMSD difference between the iterations. The Fresnel fit (Figure 5.7(a)) yield brightness temperatures in the lower incidence angle regime by about 2 K to 5 K while at higher incidence angles from 60° the Fresnel fit yield too low brightness temperatures for both $T_{b,H}$ and $T_{b,V}$ by up to 5 K. The exponential fit function (Figure 5.7(b)) has a similar pattern as the Fresnel fit in terms of the mean deviation but the bias is slightly smaller with about +2 K at lower incidence angles and is slightly more accurate over the whole incidence angle range than the Fresnel fit. Figure 5.7(c) shows the standard deviation of the mean binning as a measure of spread of the individual observations, i.e., the daily variations and the spread of brightness temperatures within one overflight for each incidence angle bin. It shows values of 3 K to 6 K over the whole incidence angle range with little variation. Small local minimums at 20° to 30° and 50° in both $T_{b,H}$ and $T_{b,V}$ indicate higher accuracy in this incidence angle range. This agrees well with Figure 5.1 where we find lower standard deviations on average around these incidence angles. The number of data points containing data in the given incidence angle bin is shown as a histogram (Figure 5.7 (d)) in green, while the average number of data points within each incidence angle bin per grid point is shown in blue. The incidence angle range of 25° to 60° is observed most often within a day while towards the lower and higher incidence angles there are fewer observations. The blue area in (d) can be interpreted as weight for the incidence angle range in the fits, e.g., at the broader peak around 38° to 43° both fits show a small bias. Note the maximum in average number of observations in (d) coincide with the highest standard deviation per incidence angle bin in (c). This is a consequence from the snapshot geometry as there can be single overflights covering geographic locations only with the snapshot borders where the radiometric accuracy is lower in the extended alias free field of view (see Section 2.3).

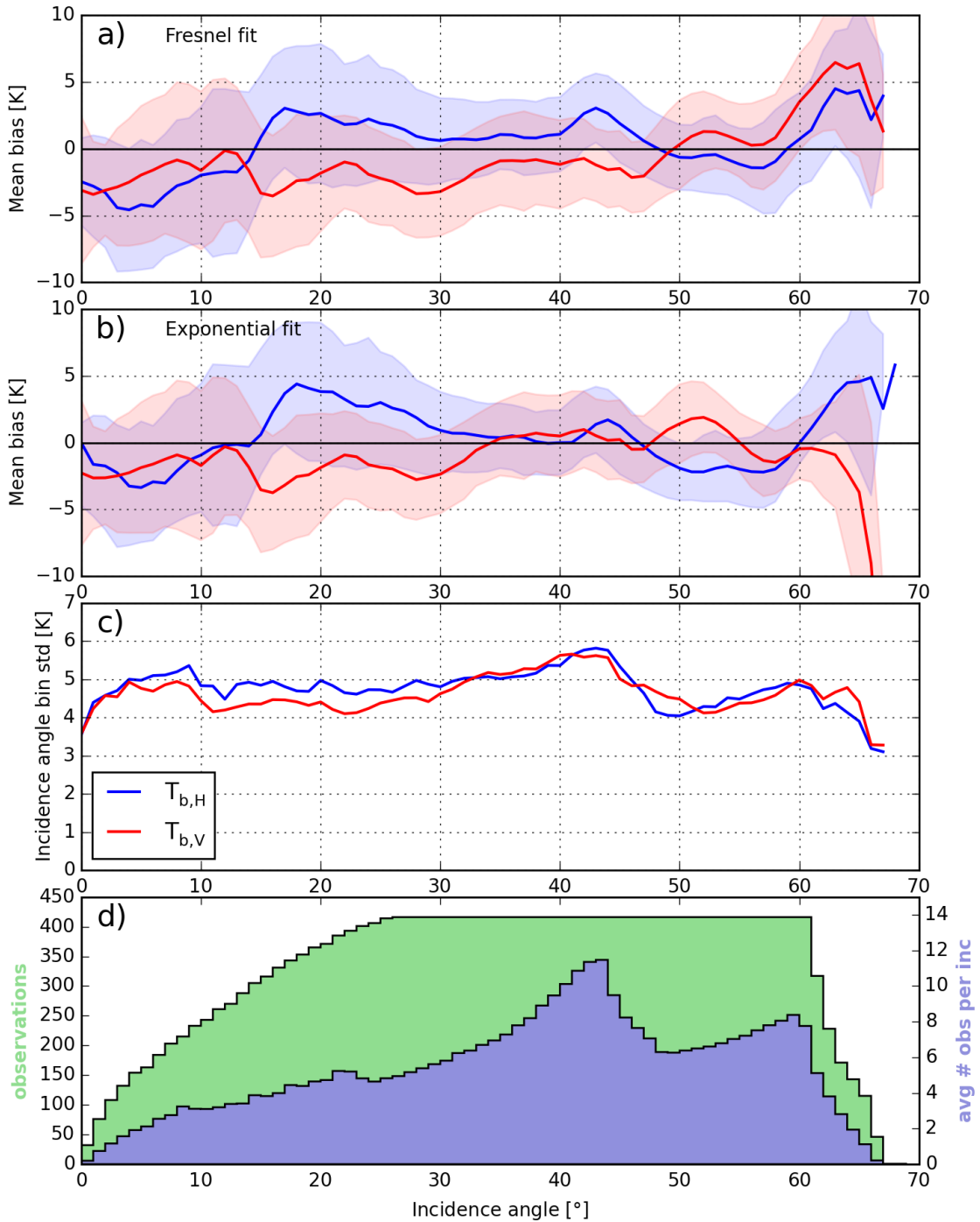


Figure 5.7: Thin ice ($140 \text{ K} < I_0 < 230 \text{ K}$); comparison of mean deviations of the Fresnel fit (a) and the exponential fit (b) to estimate the fit quality. (c) shows the standard deviation of the calculated mean for each incidence angle bin. The colored shades in (a) and (b) indicate the consistency of the mean bias as standard deviation of the mean difference between fit and binned incidence angle average. (d) number of binned and fitted data points for each incidence angle. Data from 416 fully sea ice covered regions on 28 October 2013.

Table 5.1: Mean deviations of fit functions

	Thin ice		Thick ice	
	$T_{b,H}$	$T_{b,V}$	$T_{b,H}$	$T_{b,V}$
binning std [K]	4.83	4.70	4.52	4.29
exponential fit mdev [K]	2.99	2.80	2.76	2.58
Fresnel fit mdev [K]	3.10	3.29	3.03	3.01

Figure 5.8 shows the fit performances on thick ice cases analogous to Figure 5.7. The general picture of the mean biases of the fits an (a) and (b) is similar to that of the thin ice behavior. Local minimums and maximums occur at the same incidence angles for thin and for thick ice and $T_{b,H}$ and $T_{b,V}$ show similar biases within the Fresnel and the exponential fit functions.

Table 5.1 summarizes the mean deviations from the fit functions from the incidence angle binning averaged over all incidence angles. The thin ice cases show higher deviations for the binning and also higher deviations in the fit functions. Thin ice can grow quite fast with several cm per day so that these deviations possibly result from thickness variations within one day. For thick ice, the brightness temperatures are more stable, so that smaller standard deviations and mean deviations from the binned values are expected. The mean deviations of the Fresnel and the exponential fit are similar and within the average standard deviation from the binning. Figures 5.7 and 5.8 show that both fits lie mostly within the standard deviation of the incidence angle bins, especially from 20° to 50° .

At nadir and high incidence angles the fits differ slightly from the binned values. However, we do not expect this small deviations to originate from an anisotropic dielectric constant of sea ice. At nadir up to 20° it is likely that the deviation stem from the lower accuracy of MIRAS in the extended alias free field of view (see Section 2.3). At higher incidence angles of 50° to 65° slight differences in the observed areas for same Discrete Global Grid (DGG) are expected depending on the azimuth angle as the footprints have more elliptical shape [Castro, 2008] which may cause higher variability in the brightness temperatures. The highest incidence angles observed by MIRAS at around 65° also yield lower accuracy as they are on the border of the snapshot (see Figure 2.5).

We conclude that both fit functions are an accurate way of representing SMOS brightness temperatures for all incidence angles in a more condensed format and are well suited to create a database of daily SMOS observations for sea ice applications. A complete time series of 5 Years of daily SMOS observations for the Arctic and Antarctic including error estimates would require less than 6 gigabytes (uncompressed) disk space².

²for comparison: one day of L1C sea data for the global ocean surface takes about 8 gigabytes (compressed)

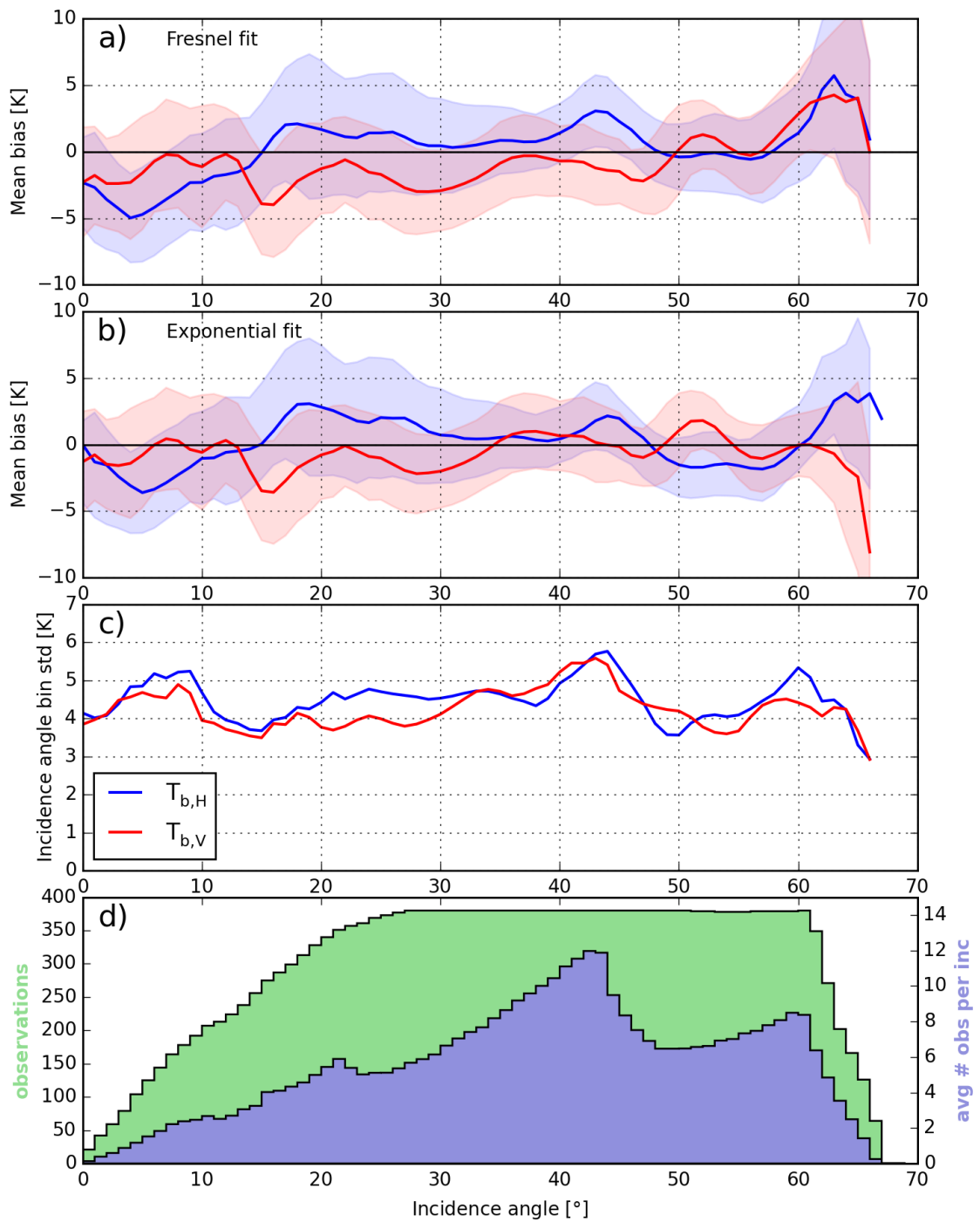


Figure 5.8: Same as Figure 5.7 but for 380 fully sea ice covered regions with thick ice ($I_0 > 230$ K)

5.1.5 Fit performance in RFI conditions

To remove the influence of unphysical angular noise as also caused by RFI, both fit methods employ an iterative method as shortly described in Sections 5.1.2 and 5.1.3. Each iteration, 20% of the data with the highest RMSD is removed and another fit is performed until a desired RMSD is reached. This method is assuming that the first fit was already close to the data. As the RMSD gets less after consecutive removal of data with the highest deviation the RMSD is not a good criterion to compare the quality between the fits. With the assumption that most data is not influenced by RFI, the tracking of the fit quality is possible using the change of the RMSD per iteration. If the RMSD change is less than 1 K between two iterations, the last fit is taken as result. This way each fit has to be performed at least twice for checking the RMSD change.

RFI was particularly strong in the beginning of the SMOS mission [Oliva et al., 2012] so that we found examples for an RFI case in the Kara Sea on 25 December 2010. In Figure 5.9 the exponential fit (a) and the Fresnel fit (b) are shown. The dashed line shows the fit without RFI filter and the solid line shows the fit for the filtered data. Single observations of $T_{b,H}$ and $T_{b,V}$ are the blue and red \wedge respectively, which cover the whole incidence angle range. Note that some observed brightness temperatures are out of the range shown here. Both unfiltered results (dashed lines) show biased brightness temperatures by about 3 K compared to the filtered results (full line). After the first few iterations most of the outliers got removed and the filtered fit is closer to data. At about 55° $T_{b,V}$ changed only little, while $T_{b,H}$ is about 4 K lower and fit better to the data just under the curve in both fit functions. We conclude that for both fit functions the iterative method works well as RFI filter.

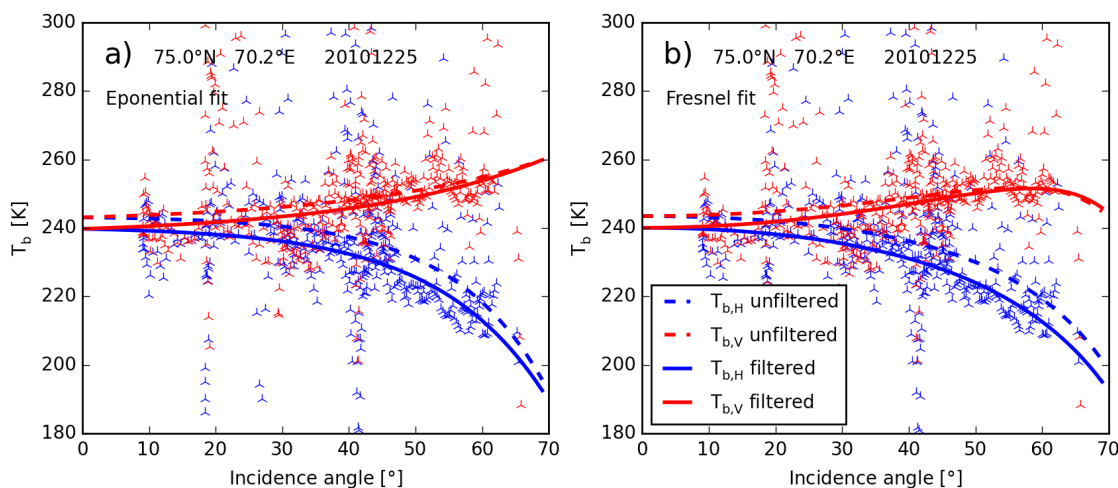


Figure 5.9: Comparison of RFI filter qualities of exponential fit function (a) and the Fresnel fit (b) on strongly RFI contaminated data in the Kara Sea from 25 December 2010.

5.1.6 Physical discussion of the multilayer Fresnel fit

In this section a physical interpretation to the Fresnel fit and the obtained refractive index parameters is given. We can introduce a physical restriction to refractive index parameters for snow and sea ice by modeling their permittivities at L-band. Previous model studies suggested that the emission of snow is negligible at L-band, i.e., the signal penetrates arbitrary thick snow covers as the imaginary part of the refractive index is negligibly small (see Figure 2.4). Recent studies also found that the thermal insulation effect of the snow layer may influence the emitted radiation [Kaleschke et al., 2013, Maaß et al., 2013]. However, the refractive index of snow in L-band is still different from that of air and therefore the snow modifies the radiation passing the ice-air interface (See also Figure 4.16).

For the fit we take into account the air, snow, and sea ice, with refractive indices N_{air} , N_{snow} , and N_{ice} , respectively. The ranges of the refractive indices of snow and sea ice are taken from the permittivity discussed in Section 2.2.4.

With $1.5 < \Re(N_{\text{ice}}) < 6.0$ and $0.0 < \Im(N_{\text{ice}}) < 2.0$, we find restrictions for the sea ice layer based on Figures 2.1 and 2.2. Here, as within our MEMLS modification (see Section 4.3), we allow complex permittivities for the calculation of the reflection coefficients for the saline sea ice top. Some values allowed here for N_{ice} correspond to rather unlikely situations for freezing conditions of first year ice like the high temperature cases. However, as we cannot be sure that the refractive index relation correspond to the observed sea ice conditions, we keep the broad range of possible refractive indices for sea ice.

For the refractive index of dry snow we use $1.0 < \Re(N_{\text{snow}}) < 1.5$ from Figure 2.4. In case of bare ice without snow cover N_{snow} can take the value of $N_{\text{air}} = 1.0$ so that the interface between N_{snow} and N_{air} disappears and N_{ice} still yield the refractive index of the sea ice top. The Fresnel equations remain valid and the reflection coefficient from N_{snow} to N_{air} for any incidence angle will be 0 while the propagation angle remains the same. Thus, in case of bare ice we expect the Fresnel fit to converge to a solution with $N_{\text{air}} = N_{\text{snow}} = 1.0$.

The specific restrictions for the refractive indices expected for each layer type is summarized in Table 5.2.

The uppermost layer of first-year ice is the most saline and therefore has the highest refractive index in both, real and imaginary parts as calculated for the frazil ice dielectric model also used in MEMLS (See Figure 2.1). Radiation reaching MIRAS at high incidence angles stem from steeper angles within the sea ice according to Snell's law (Equation (2.10)). As a consequence we expect the radiation to be practically unpolarized before leaving the sea ice medium. In this case all angular dependence of the polarized radiation measured outside of the ice is caused by the transition through the uppermost sea ice and

Table 5.2: Modeled restrictions for refractive indices

ref idx	layer type	ref min	ref max	ref init
N_{air}	air	-	-	1.0
N_{snow}	snow	1.0	1.5	1.2
$\Re(N_{\text{ice}})$	sea ice	1.5	6.0	3.0
$\Im(N_{\text{ice}})$	sea ice	0.0	1.5	0.2

snow layer and can be described by effective refractive indices of snow and sea ice. We will provide further evidence for this assumption later in Section 5.2.1 for most first year ice cases.

Retrieving refractive indices

In this section we evaluate the fit parameters of the Fresnel fit function and discuss their physical meaning. As the fit parameters are basically refractive indices of snow (N_{snow}) and sea ice (N_{ice}) we will speak of them as retrieved refractive indices. The additional parameter of the intensity I_0 is also retrieved but it exclusively adjusts the nadir intensity and does not influence the angular dependence of $T_{b,H}$ and $T_{b,V}$. However, in reality I_0 is still related to the refractive indices especially at higher temperatures near the freezing point where the contrast in refractive index is the main restriction of the emission as discussed in Section 4.4.

The imaginary part of N_{ice} was negligibly small in all retrievals. Higher $\Im(N_{\text{ice}})$ only introduces a negative offset in the brightness temperatures which is nearly incidence angle independent in the considered range of 0° to 68° (see Figure 4.16). This introduces an ambiguity with the parameter of the nadir intensity I_0 . Instead of that the fit converges at higher $\Im(N_{\text{ice}})$, the Fresnel fit may converge at lower I_0 . We therefore fix $\Im(N_{\text{ice}}) = 0$ for the following investigation.

To estimate if our retrieved refractive indices realistically describe snow and sea ice, we use the Fresnel fit on two consecutive days in both the Arctic and Antarctic during the freeze up period. We exclude points closer to 25 km to the coast and open water points as it is not subject of this study. We define water as where the I_0 is below 120 K (See Figures 3.1 and 4.16). Furthermore, we exclude cases where the iterative solver converged against values of N_{snow} and N_{ice} near the limits defined in Table 5.2. Figure 5.10 shows a 2d histogram from all three fit parameters against each other in the Arctic (top row) and in the Antarctic (bottom row). Note that the color scale is logarithmic so that a single data point appears as gray pixel, while densely populated black pixels contain several hundred data points. A pronounced linear structure is visible in the relation of N_{snow} and N_{ice} in a) and d) which can be described as $N_{\text{ice}} = 1.6 + 8 \cdot (N_{\text{snow}} - 1.1)$. The range of the parameters show that N_{ice} yields much lower values than even the refractive index of fresh

water ice with about $N = 1.78$ (See Figures 2.1 to 2.3 at low salinity and corresponding discussion). In the Antarctic in d) the N_{ice} values are higher on average. This can be explained by the ice type distribution. Even though we chose a freeze up period for our investigation, the Arctic area contains a large fraction of multi-year ice which tends to be more rough, less saline, and less dense compared to freshly formed first-year ice [Thomas and Dieckmann, 2009, Shokr and Sinha, 2015]. Here, scattering at the surface may affect the emitted radiation at L-band and the interface cannot be considered as plane. In the Antarctic most ice is little deformed first year ice where the interface is mostly plane. The Antarctic N_{ice} show realistic refractive indices for first year frazil ice in the range of $1.6 > N_{\text{ice}} > 2.4$ for various salinities and temperatures (Figure 2.1, Table 5.2). However, the values for N_{snow} are lower than expected. $N_{\text{snow}} = 1.1$ indicate very loose snow with a density of about 120 kg m^{-3} while we expected more dense snow of around 300 kg m^{-3} resulting in $N_{\text{snow}} = 1.25$ (Figure 2.4). In the fits, retrieved refractive indices $N_{\text{snow}} > 1.2$ occur seldom. Cases without snow cover, which we expected at $N_{\text{snow}} = 1.0$, are sparsely populated which we think is realistic. However, we did not expect to see that pronounced relation of N_{snow} to N_{ice} as we found in both the Arctic and Antarctic. Comparing I_0 and N_{snow} in b) for the Arctic and e) for the Antarctic we see that for $N_{\text{snow}} = 1.0$, i.e., no snow cover, the nadir intensity I_0 is lower than for $N_{\text{snow}} = 1.1$. While in the Arctic I_0 tend to have higher values with a pronounced density maximum at $I_0 \approx 250 \text{ K}$ and $N_{\text{snow}} \approx 1.1$ the Antarctic values show mostly lower I_0 and a broader peak between $1.1 < N_{\text{snow}} < 1.2$ and $220 \text{ K} < I_0 < 245 \text{ K}$. Here again, the large amount of multi-year-ice in the Arctic may explain this difference. The relation between I_0 and N_{ice} is shown in c) and f). Only the lower N_{ice} which we relate to multi-year ice yields the highest brightness temperatures. With increasing N_{ice} the I_0 gets lower in general.

In case of thick plane ice, I_0 is mostly determined by the transmission through these upper layers, i.e., their dielectric properties. The transmission coefficients at nadir for all combinations of N_{snow} and N_{ice} determined using the Fresnel Equations (2.11) is shown in Figure 5.11 a). For $N_{\text{snow}} = 1$, i.e., sea ice without snow layer, we find the minimum transmissivity for any given N_{ice} . At 50° incidence angle the transmissivity for horizontal and vertical polarized radiation is shown in b) and c). The τ_v dependence on the snow layer is weak at this incidence angle close to the Brewster angle for the transition from snow to air. We therefore expect to find vertical polarized brightness temperatures to be nearly snow independent at 50° incidence angle. τ_h in contrast has a strong dependence on both N_{snow} and N_{ice} , e.g., at a fixed $N_{\text{ice}} = 2.5$, τ_h varies from 0.65 to 0.85 and at a fixed $N_{\text{snow}} = 1.2$ we find τ_h from 0.6 to 0.9. In d) the transmissivity difference is shown which is a measure similar to the polarization difference when speaking in terms of brightness temperatures. However, in contrast to brightness temperature, the transmissivity difference does not scale directly with temperature. The highest values in the transmissivity difference occur at the combination of low N_{snow} and high N_{ice} corresponding to warm first year ice

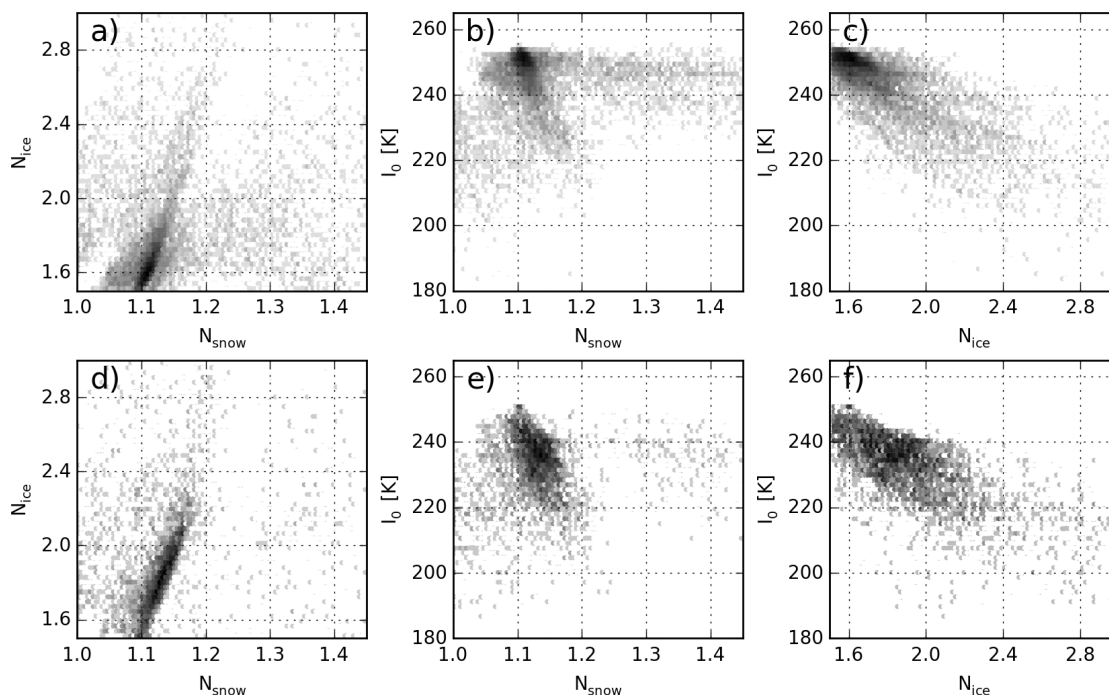


Figure 5.10: Comparison of the relation of Fresnel fit parameters during freeze up in the Arctic (a,b,c) and Antarctic (d,e,f).

without snow cover, while with increasing N_{snow} and decreasing N_{ice} the transmissivity difference decreases.

The findings allow establishing a relation of the transmissivities to our empirical retrieval (Chapter 3). Firstly when ice starts to grow it has no snow cover ($N_{\text{snow}} = 1$) and is warm while it is thin which leads to high N_{ice} (See Figure 2.1). With growing ice, the surface becomes colder (decreasing N_{ice}) and also snow may accumulate and densify (increasing N_{snow}). Following this path Figure 5.11 d) the transmissivity difference decreases and thus the polarization difference does. Even though these effects have no direct connection to the ice thickness, they are statistically correlated, so that the brightness temperature difference may serve as an indicator of ice thickness as it is used in Chapter 3.

Accuracy and consistency of retrieved refractive indices

The Levenberg-Marquardt method used for the Fresnel fit requires many evaluations of the cost function Section 5.1.2. From the intermediate results between the iterations an error estimation of the fitted parameters is possible. In the following, we will discuss the accuracy as measured by the uncertainties of the parameters estimated during the fit.

The most stable of the parameters is the nadir intensity I_0 where the uncertainty is less than 1 K in all cases. The relation between N_{snow} and N_{ice} to their uncertainties calculated

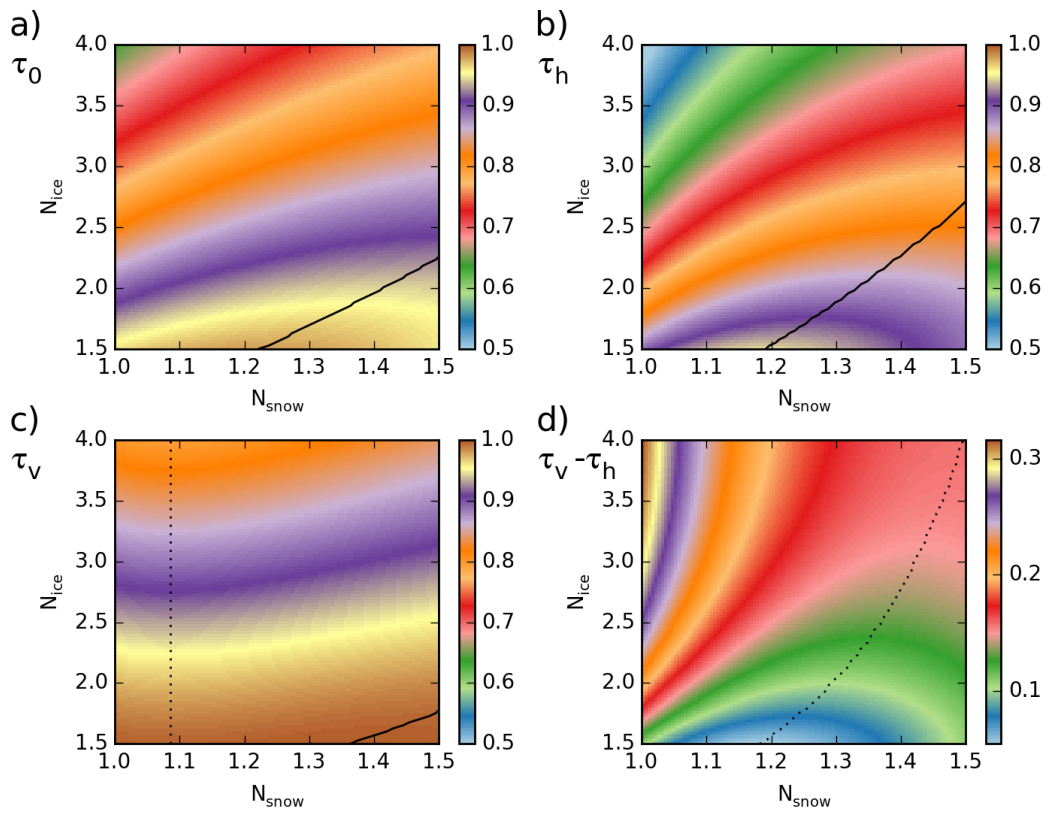


Figure 5.11: Illustration of transmissivity for given combinations of N_{snow} and N_{ice} . a) nadir transmissivity, b) and c), transmissivity at 50° incidence angle. d) difference vertical and horizontal transmissivities at 50°. The maximum transmissivity for a given N_{ice} is shown as black solid line. The minimum is shown as a dotted black line.

during the fitting procedure is shown in Figure 5.12 (a) and (b) respectively. For small N_{snow} , the uncertainty of N_{snow} is small, while it has a maximum at $N_{\text{snow}} = 1.1$ for small $N_{\text{ice}} \approx 1.6$ which shifts to higher N_{snow} with increasing N_{ice} . The uncertainty of N_{ice} grows mainly with N_{snow} and at $N_{\text{snow}} > 1.15$ and $N_{\text{ice}} > 2$ it takes its highest values of 0.7 to 1.0.

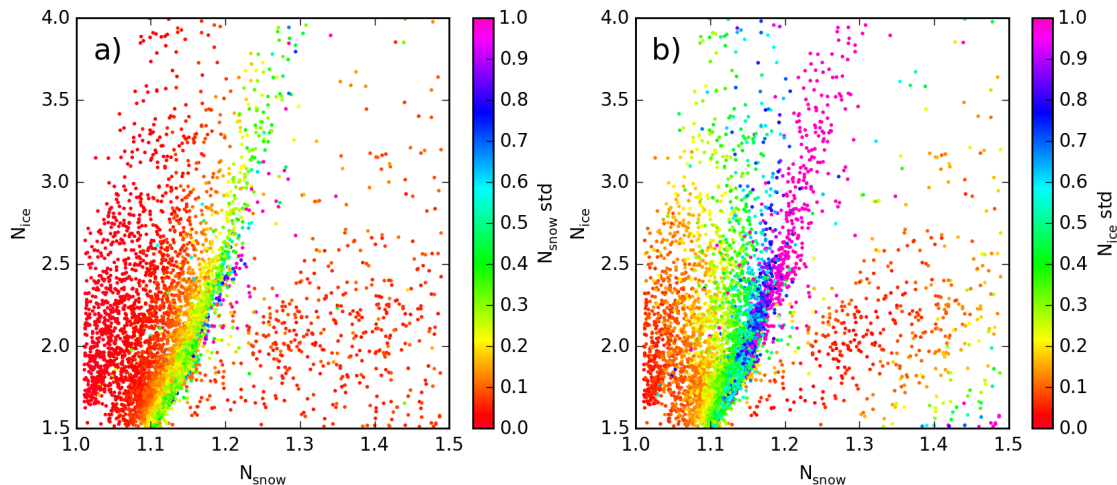


Figure 5.12: Relation of standard deviations of N_{snow} a) and N_{ice} b) to the retrieved refractive indices N_{snow} and N_{ice} for the 20 March 2013 in the Antarctic.

This relation shows that we face an ambiguity along the relation of N_{snow} and N_{ice} described in the previous section as $N_{\text{ice}} \approx 1.6 + 8 \cdot (N_{\text{snow}} - 1.1)$. To support this conclusion, we show an example map of the Ross Sea and the Weddell Sea of two consecutive days during the Antarctic freeze up period in Figure 5.13. These regions were chosen because of good convergence of the Fresnel fit and spacial consistency of the parameters. In the Weddell Sea N_{ice} looks relatively stable especially close to the peninsula and ranges mostly from 1.5 to 2.25. In the center both, N_{snow} and N_{ice} decreases from one day to the next, N_{snow} from about 1.15 to 1.12 and N_{ice} from about 2.0 to 1.75. This variation however, is on the line with the previously found linear structure in Figures 5.10 and 5.12. In the Ross Sea in the center N_{ice} drops from about 1.8 to 1.5 while N_{snow} decreases from about 1.13 to 1.08. A bit eastern in the Ross Sea image we see N_{ice} increases from about 1.5 to about 1.8 which is connected to an increase in N_{snow} from about 1.09 to about 1.13. This is an opposite change in refractive indices of two regions only few hundred kilometers apart. As most regions show spatially consistent refractive indices while individual grid points are fitted completely independently, a geophysical change, e.g., temperature, is indicated. However, NCEP temperature data shows only a mild increase in temperature. Another possible explanation can be that different satellite observing geometries or the characteristics of the Fourier like reconstruction for the snapshot are influencing the fitted

parameters.

Conclusion on retrieval of refractive indices

The current retrieval of refractive indices retrieves the nadir intensity I_0 independently of the refractive indices while these quantities are related through the Fresnel equations (Equation (2.9)). The shape of the brightness temperature dependence with the incidence angle relative to the nadir intensity is apparently not unique, so that different combinations of refractive indices can give similar low RMSD for the fit. The situation can be taken as ill posed considering the uncertainties.

For the connection of the nadir intensity I_0 to the transmissivity a consideration of the internal sea ice structure and the open water interface is required. This however would turn the simple Fresnel fit into the inversion of a complete emission model.

Another potential source of uncertainty of the current approach is the assumption that the snow is a single layer with a single refractive index. As we discussed in Section 2.2.4, the refractive index of snow is in the microwave regime mostly dependent on the snow density. The snow cover on sea ice undergoes an aging process which includes densification by gravity and accumulation of new snow on top, as well as brine uptake from the sea ice. Therefore, the assumption of snow being a single layer described by the single parameter of density and thus by a single refractive index, is probably too simplified. It was shown in Figure 4.20 that for an ensemble of snow densities the emissivity and thus the brightness temperatures show coherent oscillation with the snow depth using the MEMLS model. At first glance, this may invalidate the assumption of incoherent power propagation which is the basis for the multilayer Fresnel fit. However, in nature the snow depth has a spacial variability which leads to a distribution of snow depth values, especially on the scale of a SMOS footprint of 50 km [Haapala et al., 2013]. These variations in snow depth and ice thickness may average out coherence effects and justify the assumption of incoherent power propagation. We will quantify this effect using snow depth data from Operation IceBridge (OIB) and an emission model for layer thickness distributions in Section 5.2.6.

5.2 Revision of modeling

In this section we present models based on simple physical relations that give results comparable to MEMLS but are much simpler, faster, easier to implement, and easier to use.

These simple models introduced in Section 2.1 are applied to investigate in problems and opportunities that arise from the simplifications and assumptions. First the consequences of choice for one of the dielectric models and the assumption of plane parallel smooth layer are investigated. The power propagation of the radiation is discussed using a

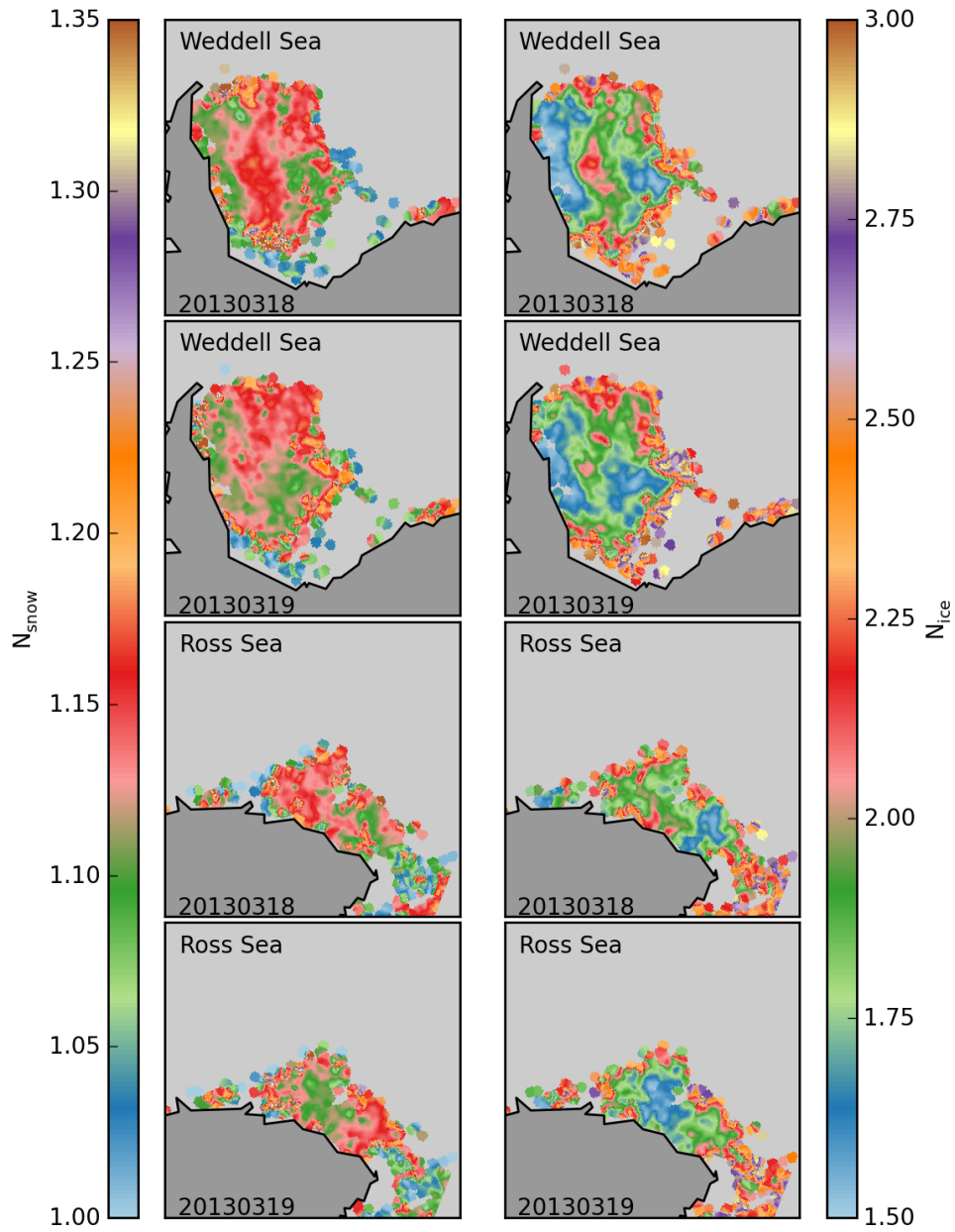


Figure 5.13: Retrieved refractive indices N_{snow} (left) and N_{ice} (right) in the Weddell Sea and Ross Sea on 18 March 2013 and 19 March 2013.

simple incoherent radiative transfer model (Equation (2.13)). Afterwards, the conditions for incoherent radiative transfer and the effects from coherent layers of sea ice and snow cover are discussed using a coherent radiative transfer model (Equation (2.14)). For this purpose an ensemble of coherent simulations is incorporated as a third model accounting for ice thickness and snow depth distributions within typical footprint sizes by comparison to OIB data. Finally, the two simple models (incoherent and coherent) are compared with the modified MEMLS (Section 4.3) based on the findings to conclude on the relevant effects for L-band simulations.

5.2.1 Radiation within the ice (incoherent model)

In addition to the complex MEMLS model, we employ the rather simple incoherent model introduced in Equation (2.13) in Section 2.2.

For this analysis we consider sea ice in a constant temperature environment, growing with a linear temperature profile. After the sea ice formation, it is considered as a layer between air and ocean. In this case the amount of radiation leaving the ocean is modified by the change of the interface from water-air to water-ice-air. This is a similar effect as discussed for snow on sea ice in Section 4.3.7. In incoherent models, this modification of the interface is seen as a jump in brightness temperature by about 30 K to 50 K when sea ice first forms (Section 4.2, [Kaleschke et al., 2013, Maaß et al., 2013]). By assuming the interface properties between water and sea ice as constant in first approximation, an increase of sea ice thickness cause an increase in the emitted radiation due to absorption and emission in the ice. When the intensity, measured in units of the brightness temperatures, within the ice reaches the physical temperature, the radiation within the ice reaches its maximum. From this point, an increase of ice thickness lowers the radiation in the ice as the ice gets colder towards the ice-air interface. The radiation leaving the ice, which can be measured as brightness temperature, is then completely defined by the dielectric properties, i.e., the refractive index of the ice surface and its snow cover. The dielectric properties of sea ice can vary depending on the growth conditions influencing the shape and orientation of the brine inclusions inside the ice (Section 2.2.4, [Shokr, 1998]).

In the following we use a simple thermodynamic ice growth model based on the CFDD (Equation (2.16)) with linear temperature gradient and salinity modeled from ice growth rate (Equation (2.17)) to generate layers on an hourly basis. These layers are defined by their key properties of thickness, salinity and temperature and serve as input for the simple radiative transfer model (Equation (2.13)). The model is based on the dielectric properties of the layers to model the power transmission, absorption and emission from the layers while ignoring scattering and second order reflection. The model is therefore incoherent. Firstly, only the radiation emitted from the water, traveling through the ice towards the sky ignoring all backwards propagations reflected radiation is taken into account. This allows an illustration of the evolution of the radiation within the ice.

In Section 2.2.4 we introduced three different models for the dielectric properties of sea ice, the model by Vant et al. [1978], and two dielectric mixture models for frazil and columnar ice by Polder and van Santeen [1946], Shokr [1998] which are compared here within the radiative transfer model. Here again, what we call *columnar* is modeled with spherical inclusions as oriented inclusions leads to birefringence and cannot be addressed with this simple radiative transfer approach.

The sea ice growth is simulated at -20°C air temperature, assuming a vertical linear temperature gradient in the ice. For hourly sampling, i.e., each hour a layer is created, this result in 2277 layers for 1 m thick ice grown in about three months. The CFDD based model (Equation (2.16)) is for a snow layer of $0.08 \cdot d_{\text{ice}}$ which is not accounted for in this analysis as it only modifies the interface and does not influence the radiation inside the ice. However, in reality a snow layer would increase the surface temperature of the sea ice through thermal insulation. For this discussion, the snow layer is not important, so that -20°C is the fixed ice surface temperature of the ice. Figure 5.14 shows the radiation emerging from the sea water evolving along its way through the sea ice. The brightness temperature shown in Figure 5.14 is the radiation which would be measured within the ice looking downwards. In this illustration, the downwelling radiation emitted by the ice and reflected back upwards at the sea ice bottom is ignored. At -100 cm and 0 cm the vertical solid black lines line shows the water to sea ice, and sea ice to air interface respectively. The cyan line shows the physical temperature at each height, means the water temperature below -100 cm, the ice temperature from -100 cm to 0 cm, and the air temperature above 0 cm. The values shown for each model above 0 cm are the brightness temperatures which can be measured by an instrument outside of the ice. At the transition from water into the sea ice, a fraction of radiation is transmitted depending on the refractive index modeled for the lowest sea ice layer. The frazil ice model provides the lowest contrast in refractive index of the three dielectric models (Section 2.2) to water and therefore a higher amount of radiation penetrate through the water-ice interface while the highest contrast is modeled using the Vant model resulting in the lowest transmission. Within the ice, the contrast of the real parts of refractive indices between the layers is negligible especially when many layers are modeled with only gradually changing temperatures and salinities. Therefore, only the imaginary part of the refractive index influences increase and decrease in terms of absorption and emission according to Kirchhoff's law.

The columnar ice type (red in Figure 5.14) shows a higher increase of the radiation close to the sea ice bottom around -100 cm to -80 cm and at the sea ice top around -10 cm to 0 cm, while the increase is lower in between. This can be explained by the high temperature at the sea ice bottom and the high salinity at the sea ice top. In both cases the brine volume fraction is increased which leads to higher imaginary part of the refractive index, thus to higher absorption and emission. This also applies to the Vant and the frazil ice dielectric model. However, the effects are not visible in Figure 5.14 due to saturation

of the radiation. With *saturation* we mean in this context that the brightness temperature reaches the physical temperature of the layer, so that about the same amount of radiation is absorbed as it is emitted. The columnar dielectric model does not reach saturation in this simulated sea ice situation with 1 m thickness.

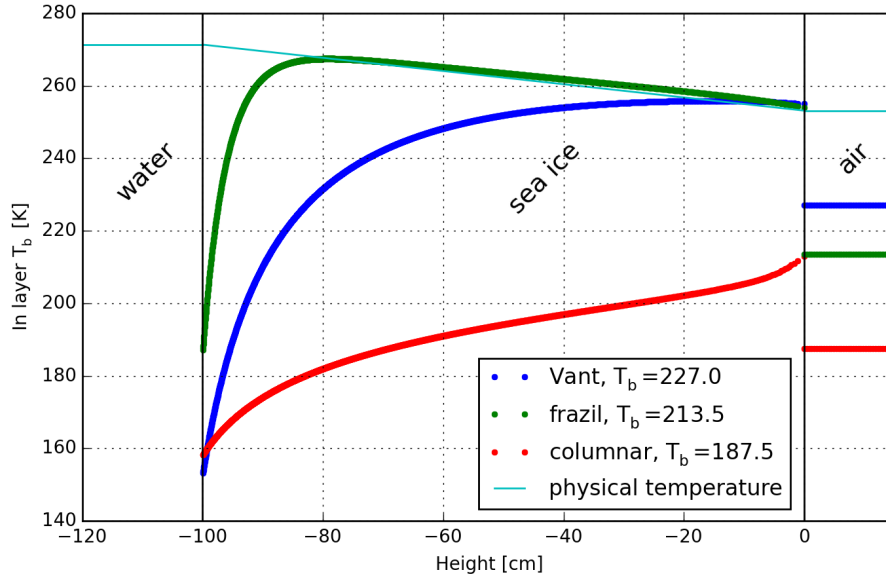


Figure 5.14: Brightness temperature which would be measured inside a 1 m thick sea ice from the direction of interface of water to sea ice for three different dielectric sea ice models. Sea ice growth simulated by a CFDD based model.

The frazil ice dielectric model (green) shows a strong increase in radiation within the first few centimeters which reaches the maximum at -80 cm depth where the brightness temperature meets the physical temperature of the ice layer. From this point the radiation follows the linear temperature profile due to the strong absorption and emission within the ice. The frazil ice dielectric model suggests that the emitted L-band radiation is mostly sensitive to the ice surface properties of salinity and temperature. This is consolidated from the wide range of refractive indices and high sensitivity of the frazil ice model to salinity and temperature changes (See Figure 2.1). The frazil ice model was also used within MEMLS to model the dielectric constant of the ice which lead to a correlation of brightness temperature to ice thickness because of decrease in average surface temperature for the input from the energy balance model (see Section 4.4.3).

The radiation for the Vant dielectric model shows also a strong increase after the drop from the transition between water and ice. From -40 cm on the radiation slowly goes into saturation and at the ice-air interface the intensity is similar to the frazil dielectric model. Both, frazil and Vant dielectric model show slightly higher brightness temperatures in the uppermost layers than the physical temperature.

Comparing at the brightness temperatures which would be measured in the air for each dielectric model reveals a wide spread result over a range of nearly 40 K. The lowest brightness temperature is modeled for the columnar model as expected since the intensity did not reach the saturation within the 1 m of sea ice for the columnar model. Even though the brightness temperatures simulated for the Vant and frazil dielectric model are as close as 2 K within the sea ice top, once leaving the ice they show a large difference due to their difference in refractive index for the same salinity and temperature combination of the top layer.

The three models show in this particular case of 1 m thick ice in Figure 5.14 all three possible cases of

- **strong absorption** (frazil model)
shows early saturation and the emission is determined by surface temperature and salinity conditions, practically no sensitivity to variation in ice thickness.
- **medium absorption** (Vant model)
saturates at sea ice top, the emission follows middle layer temperatures and is influenced by the surface properties. It has low sensitivity to ice thickness at this stage.
- **weak absorption** (columnar model)
no saturation reached; emission proportional to ice thickness, but influenced by the interface properties, mainly the water-ice interface.

Note that these cases are relative to the ice thickness, e.g., for 30 cm thick ice, the Vant model does not reach saturation and is strongly influenced by the interface conditions and thus falls in the weak absorption category (not shown here).

By the term of *interface conditions* we mean the transmissivity through the interface between water to sea ice and the transmissivity between the ice and air. Modeling the sea ice salinity for each layer using the ice growth rate (Section 2.2) introduces some uncertainty regarding the interfaces. Firstly, the initial ice formation happens at an enormous growth rate, so that the salinity of the uppermost sea ice layers are very high. In addition, with a linear temperature gradient through the ice, the sea ice bottom is warm but has also low salinity. However, measurements taken on sea ice cores show higher salinities at the sea ice bottom [Nakawo and Sinha, 1981, Notz and Worster, 2008]. This is in contrast to the parametrization of salinity with growth rate used here and in Chapter 4, which is meant as a steady-state salinity approximation within the ice. At the sea ice bottom we therefore expect major uncertainty regarding the modeled transmissivity at the interface. However, the down welling radiation and consequent reflection at the sea ice bottom is not modeled in Figure 5.14. Including backwards propagation decreases this uncertainty as will be shown in the next paragraph. In addition, the dielectric models are meant for

condition within the sea ice, and have high uncertainties for warm and saline conditions (Section 2.2). Especially the Vant model is not suitable for saline and warm conditions where the brine volume fraction exceeds about 7% [Vant et al., 1978, Kaleschke et al., 2010, 2013]. Both mixture models should be applicable also at higher brine volume fractions. However, such high brine volume fractions result in highly porous sea ice conditions, where a distinct inclusion geometries like randomly oriented needles or spherical inclusions are rather unlikely to represent the inclusions adequately [Petrich and Eicken, 2010, Golden et al., 2007].

Propagation direction

In the analysis above we only considered radiation coming from the sea water propagating through the ice while undergoing absorption and emission. In reality, the thermal emission by the sea ice also propagates downwards while a part of it is reflected back upwards and may reach the instrument. In the general incoherent case the emission and absorption of all layers have to be considered together with all reflections from all interfaces including multiple reflections [Orfanidis, 2014, Ulaby et al., 1981]. This can be computationally expensive even though many terms are negligible for the calculation of the emitted radiation by sea ice. As a simplification some models take into account less reflection terms like the model by Burke et al. [1979] used by Maaß et al. [2013]. However, when it comes to many layer structures the model underestimates the emitted radiation as a result of negligence of downward radiation propagation transmitted through layer boundaries (See also Maaß et al. [2013] and open discussion of Maaß et al. [2013]). In multilayer sea ice structures, the layers are similar in dielectric properties and therefore yield small reflection terms and most radiation is transmitted between adjacent sea ice layers. A simple but relatively accurate approach in these structures is to simply neglect all boundaries inside the sea ice. The snow-air, snow-ice, and ice-water boundaries have to be considered as they yield stronger dielectric contrast and thus cause reflection. To calculate the brightness temperatures with these assumptions Equation (2.5) can be employed. Starting from the topmost sea ice layer downwards, the propagating radiation can be determined as absorption and emission of each individual layer. Once reaching the sea ice bottom, the reflected signal and the transmitted radiation coming from the underlying ocean water form the upward radiation. This upward radiation again undergoes absorption and emission for each sea ice layer on the way to the sea ice top. The rather small contribution from the directly reflected cosmic background or atmospheric contribution from the air-snow interface and from the snow-sea ice interface may be added in the end. This way the calculation is rather simple and more accurate than using the model by Burke et al. [1979] in this multi-layer environment.

For the following discussion this procedure is employed. As we just pointed out the importance of the reflection coefficients at the interfaces we have to reconsider the assumption

of plane parallel interfaces and uncertainties regarding the transmission and reflection at these interfaces. At this point we have to underline the major difference between a multi layer model for sea ice, considering only refraction at sea ice bottom and sea ice top, and employing a single layer model for sea ice. Considering sea ice as a single layer with bulk temperature and salinities leads to a single refractive index for the sea ice. However, the refractive index depends on temperature and salinity and yields strong variations in the case of high salinity or high temperatures as we expect close to the sea ice top and bottom (Figures 2.1 to 2.2). Therefore, we consider multi layer models as more accurate even though the variability of the reflectivities at the layer boundaries are very high. This variability is increased in addition by roughness effects which we investigate in the next section.

5.2.2 Interface roughness effects

One effect which modifies the ice-water and ice-snow interface the is the small scale roughness. The assumption of negligible roughness at the interfaces at L-band due to the long wavelength is a strong simplification especially at the sea ice bottom. To investigate in this effect a small correction for the Fresnel reflection for rough surfaces from Choudhury et al. [1979] is introduced as

$$R_{p,\text{rough}}(\theta) = R_p(\theta) \cdot \exp(-4\sigma^2(2\pi/\lambda)^2 \cdot \cos^2 \theta), \quad (5.8)$$

with σ as standard deviation, R and R_{rough} as Fresnel reflection and modified Fresnel reflection respectively and p as the polarization. The exponent of the cosine term of the incidence angle dependence is critically discussed in literature and also the standard deviation was found to not adequately represent roughness effects properly. It is suggested to use the autocorrelation of the roughness (correlation length) to improve the modification of the transmitted radiation through the rough interface [Mätzler, 2006, Choudhury et al., 1979]. However, as first approximation we are mainly interested in the characteristics of a surface roughness on the brightness temperatures. Figure 5.15 shows different combination for surface and bottom roughnesses for each dielectric model (rows) for three different ice thicknesses (columns) for a surface temperature of -20°C at nadir. For $d_{\text{ice}} = 50\text{ cm}$, for the frazil and Vant models, the main sensitivity is found along the surface roughness axis because all effects emerging from the bottom roughness are hidden due to emission and absorption along the propagation path through the ice. Changes in the bottom roughness are still visible in the brightness temperatures for the weak absorbing columnar dielectric model. In case of thin ice at $\text{SIT}=2\text{ cm}$ the Vant model shows a strong sensitivity to the bottom roughness because most radiation emerging from the water is reaching the surface as the absorption within the ice is small. The columnar model which also has a weak absorption shows higher brightness temperatures than the Vant model at small bottom

roughnesses at $SIT=2$ cm. In the frazil model the strong absorption is dominating and no sensitivity to bottom roughness is visible regardless of the ice thickness. In addition, the frazil ice model shows lower variability of brightness temperatures.

Figure 5.15 shows that the brightness temperatures using the frazil ice model and the Vant model (at higher bottom roughnesses) become smaller with increasing ice thickness. The surface layer has the same temperature at all ice thicknesses, thus have the same transmissivity through this layer independent of the ice thickness. However, the layers below are warmer at smaller ice thicknesses which increases the resulting brightness temperatures. Therefore, in case of rough sea ice bottom conditions, where most radiation from the water is penetrating through the water-ice boundary further ice growth can only lower the resulting brightness temperatures in this simulation. With the columnar ice we see an exception which needs further explanation. For the discretization of sea ice thicknesses, different intervals are chosen, but the 2 cm case should be an earlier ice development stage which can lead to the 10 cm and finally to the 50 cm case. This also means that the salinity of the bottom of the 2 cm case is very high due to the fast ice growth. High salinity at high temperatures, however lead to large brine volume fraction and thus to higher refractive indices and eventually to a higher transmissivity through this interface. The absorption and emission in the columnar model is so small that the increase of bottom roughness is the dominating effect for the resulting brightness temperatures. The Vant model seems not affected because its valid range of brine volume fraction is exceeded for such a saline warm sea ice case and returned refractive indices by the Vant model are somewhat smaller than expected.

In reality we expect the water to ice interface to be more structured rather than containing statistical roughness as shown in previous studies [Kovacs, 1996, Assur, 1960]. In addition, the structure will be oriented along the direction of the current, often called C-axis [Petrich and Eicken, 2010, Untersteiner, 1986]. It was also shown that this oriented structure can cause anisotropic effects in lower microwave frequencies [Golden and Ackley, 1981].

Most investigations the roughness of the sea ice surface focus on large scale roughness with respect to microwave emission either as deviation of orientation, i.e. the incidence angle, or even distribution of thicknesses Apinis and Peake [1976], Menashi et al. [1993], Stroeve et al. [2006]. For the small scale surface roughness only few in-situ measurements were taken [Paterson et al., 1991, Manninen, 1997, Drinkwater, 1989] even though it is an important quantity for SAR and other Radar based methods [Drinkwater and Crocker, 1988, Nghiem et al., 1995]. The small-scale roughness is quite variable for different ice types and is mainly within the range of 5 mm to 30 mm [Paterson et al., 1991, Nghiem et al., 1995].

When considering higher incidence angles the effect of surface roughness on $T_{b,V}$ is

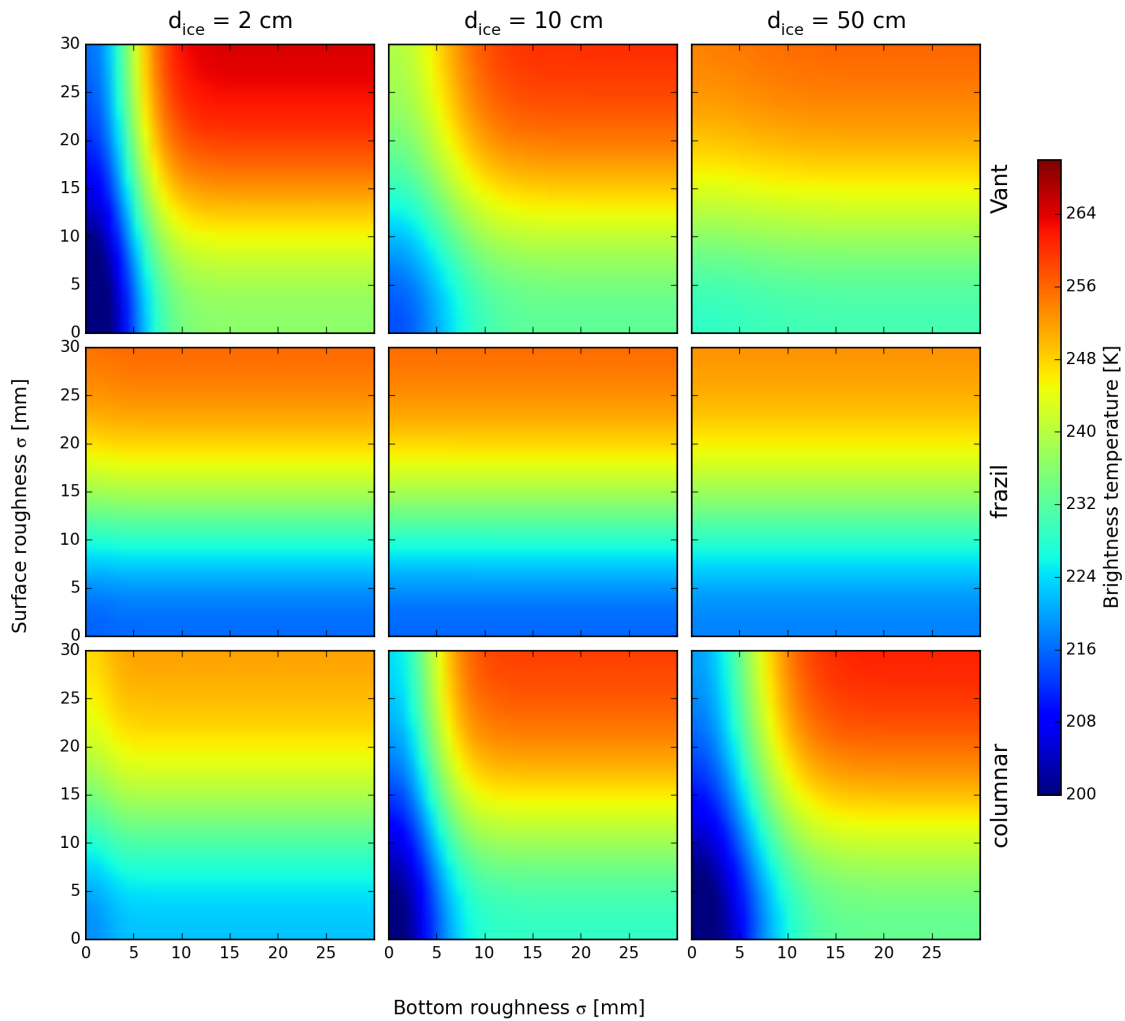


Figure 5.15: Brightness temperature for different combinations of bottom roughness and surface roughness for sea ice (without snow cover). Sea ice growth simulated with a CFDD based model.

much less than on $T_{b,H}$. Therefore, at high incidence angles, the polarization difference Q is also influenced by the surface roughness in addition to the influence from the snow cover as discussed (see Figures 4.16 and 4.20).

5.2.3 Origin of polarization effects

To follow up on the discussion from the Fresnel fit (Section 5.1.3) if polarization effects may reach the surface layer we discuss $T_{b,H}$ and $T_{b,V}$ at high incidence angles. As at the interface between ice and air, we expect the interface between water and sea ice to have a polarizing effect on the radiation according to the Fresnel Equations (2.11). However, inside the sea ice, absorption and emission have a depolarizing effect as polarized radiation is absorbed but unpolarized (thermal) radiation is emitted. Therefore, during the propagation through the sea ice, the $T_{b,H}$ and $T_{b,V}$ equalize along the propagation path towards the physical temperature of the ice.

A simulation of $T_{b,H}$ and $T_{b,V}$ at 60° incidence angle is shown in Figure 5.16 analogous to Figure 5.14 for 20 cm thick sea ice. Here, in contrast to Figure 5.14 the contribution of the backwards propagating radiation reflected at the sea ice bottom is included. $T_{b,H}$ and $T_{b,V}$ are the upper and lower occurrence of the γ and λ symbols respectively. In the frazil ice model, no split of polarization is visible as the absorption and emission is high within the sea ice so that $T_{b,H}$ and $T_{b,V}$ are practically equal close to the sea ice bottom. The refraction at the interface of sea ice to water has no influence in case of the frazil ice model as the absorption close to the sea ice bottom is large and the temperatures are similar. As a consequence, the difference in ratio of transmitted and reflected between horizontal and vertical polarized radiation is small at the water to ice interface. Using the Vant model a small split between horizontal and vertical polarization at 20 cm depth decreasing towards the sea ice surface. The split in polarization is even smaller at the sea ice surface as a result of absorption and emission and thus has practically no influence the brightness temperatures outside of the sea ice. The split of $T_{b,H}$ and $T_{b,V}$ in the Vant and frazil model therefore originate entirely from reflectivity, i.e., the dielectric properties and consequently on the salinity and temperature conditions of the surface in this simulation. For the columnar dielectric model, the absorption and emission is weak compared to the frazil and Vant model. The split of the polarizations after the transition from water to ice (plus the reflected down welling radiation) is visible along the complete profile. Therefore, the polarization difference still exists at the sea ice top and the transition through the ice-air-interface splits $T_{b,H}$ and $T_{b,V}$ even further. In case of thin ice or weakly absorbing ice like the less saline ice in the Baltic we therefore expect this effect to be observed in nature. At the incidence angle of 60° the $T_{b,V}$ is almost completely transmitted into the air layer as this transitions is close to the Brewster angle. For the frazil ice model, the Brewster angle is slightly higher as it yields higher refractive index than the other models,

so that less radiation is transmitted at 60° . The simulated brightness temperatures $T_{b,H}$ and $T_{b,V}$ which would be measured in the air is mentioned in the legend of Figure 5.16. With the transmissivity close to unity, the $T_{b,V}$ from the Vant model is slightly higher than the air temperature of 254.2 K. The $T_{b,V}$ of the columnar model is lower even though the transmissivity is high, because it did not reach saturation during its path through the ice. The columnar and frazil ice model brightness temperatures are very different as the frazil ice model reaches saturation and have therefore higher $T_{b,V}$. Even though the columnar ice model shows a polarization difference before leaving the sea ice layer, the frazil ice model still show higher polarization differences in the air. This is due to the higher contrast in refractive index for the transition from ice to air in the frazil ice model. $T_{b,H}$ simulated outside of the ice is below the scale in Figure 5.16.

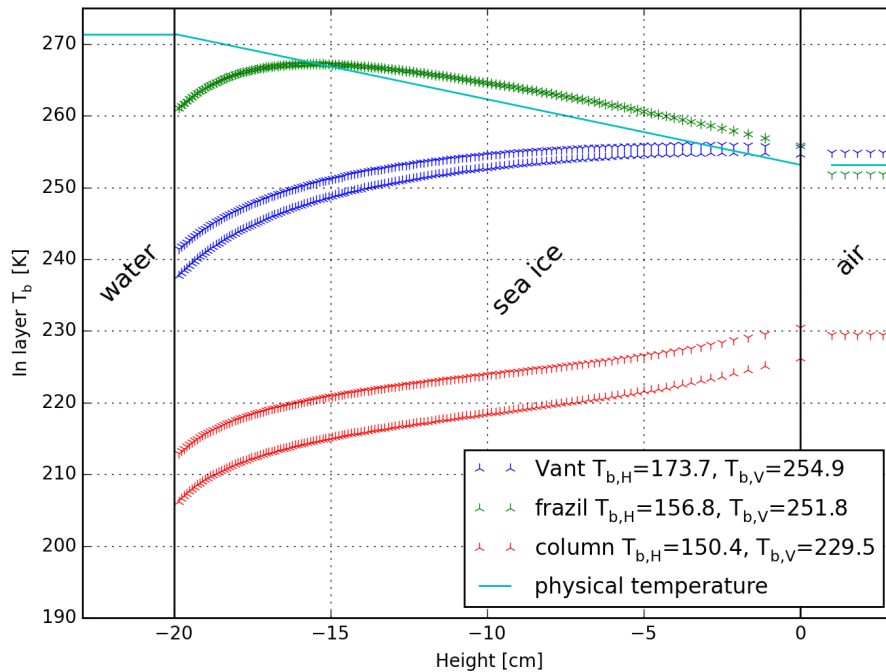


Figure 5.16: Brightness temperature at vertical (γ) and horizontal (λ) polarization inside 20 cm thick sea ice at 60° incidence angle (in air). From water, the transmitted upwelling radiation plus the contribution from the downwelling radiation which is reflected at the ice-water interface is shown. Sea ice growth simulated by a CFDD based model. $T_{b,H}$ in the air is not displayed as it is below the brightness temperature scale. The values of $T_{b,H}$ and $T_{b,V}$ which would be measured in the air are in the legend for the snow-free case.

In nature the sea ice has a snow cover in most cases. The transition between air and snow has a different Brewster angle than the transition between air and sea ice, because of the difference in refractive index of snow compared to sea ice. Therefore, the maximum $T_{b,V}$ in dependence of the incidence angle comes from a layer combination of snow and sea ice and is in general not identical to the Brewster angle of any of the involved

transitions of sea ice N_{ice} to snow N_{snow} and snow to air N_{air} . In addition, the vertical transmissivity through the double layer boundary is not equal to one which is the case for the Brewster angle for a single boundary transition. This angle is calculated using the Fresnel Equation (2.9) for different sea ice and snow refractive indices in Figure 5.17 a). The angle of maximum transmissivity for vertical polarized radiation varies from about 53° to 70° . The transmissivities at vertical polarization corresponding to the double layer interface Brewster angles are shown in Figure 5.17 b). Note that what we call Brewster angle in case of multilayer transition is strictly speaking not the Brewster angle but only the angle where the most radiation in vertical polarization passes the multilayer interface. The formal definition of Brewster angle requires all vertically polarized radiation passing the interface, which is not possible for a multilayer transition. For all temperature and salinity conditions in the Vant and columnar model and for cold conditions $T < 260$ K for the frazil ice model we find approximately $1.8 < N_{\text{ice}} < 2.5$ while typical snow conditions yield $N_{\text{snow}} = 1.25$ (See also Figures 2.1 to 2.4).

There we find Brewster angles of 57° to 60° and transmissivities from 0.96 to 0.99. For an ice temperature of 268 K a change of transmissivity of 0.01 is effectively 2.7 K difference in vertical polarized brightness temperatures. Thus, in vertical polarization, a change in surface transmissivity can cause variations of up to $0.04 \cdot 268 \approx 10$ K regardless of the physical temperature at the angle of highest transmissivity. Thus, even $T_{b,V}$ at 57° to 60° cannot be considered as unaffected by surface transmissivities through the combined ice-snow layer.

For a fixed incidence angle of 60° , the range of variation of transmissivity of vertical polarization increase only slightly from 0.95 to 0.99 translating into about 12 K in $T_{b,V}$ while for horizontal polarization, the transmissivity varies from 0.73 to 0.85 at 60° translating into more than 30 K in $T_{b,H}$ (not shown here).

The higher N_{ice} values correspond to higher physical temperatures and salinities as discussed in Section 2.2 so that the effects of increasing physical temperature and decreasing transmissivity partly compensate. A concrete estimate of this effect cannot be given here due to the high variation in dielectric properties among the different dielectric models (See also [Mills and Heygster, 2011b, Golden, 1995]).

In conclusion, the high transmissivity in vertical polarization at higher incidence angles, make $T_{b,V}$ the most stable parameter to changes in dielectric properties, snow cover and roughness. As a result, we expect the physical temperature just below the vertical polarized brightness temperature. This was also exploited by Comiso et al. [2003] for an ice surface temperature retrieval from 6.9 GHz at 55° incidence angle assuming a transmissivity of 0.98 using the AMSR-E instrument.

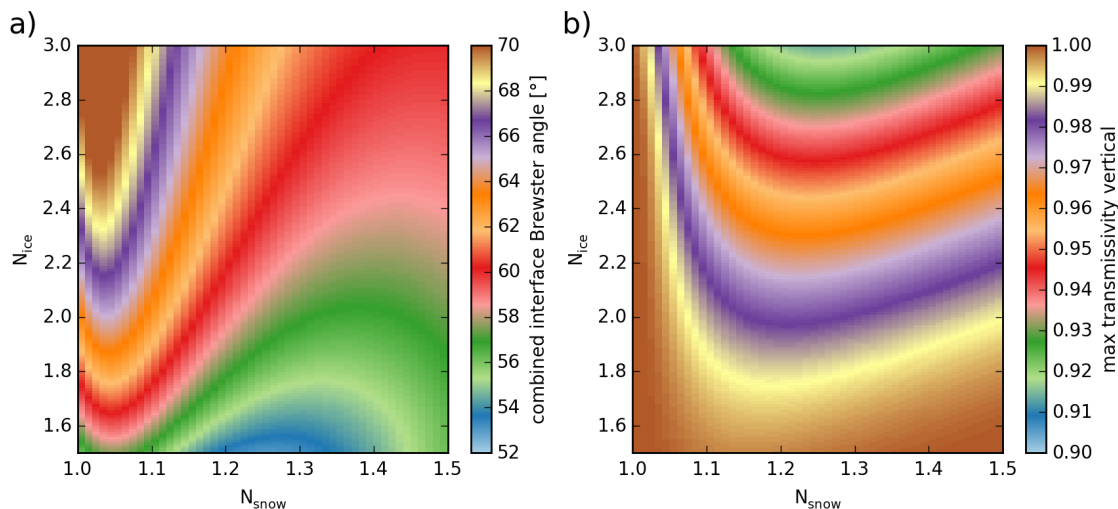


Figure 5.17: a) shows Brewster angle for double layer of snow and sea ice with refractive indices N_{snow} and N_{ice} respectively with fixed $\Im(N_{\text{ice}}) = 0$. b) shows the maximum transmissivity at vertical polarization occurring at the incidence angle shown in a).

5.2.4 Layer thickness for an incoherent radiation model

In modeling of sea ice emissivity using a layer based radiative transfer model, the challenge of choosing appropriate layering for the input sea ice profile remains. As discussed in Section 4.3, the energy balance model in combination with MEMLS led to unreasonable results caused by a layer averaging within MEMLS. In this section we discuss the input layer thickness and the role of contrast in dielectric properties between layers.

Typical snow and sea ice profiles show layering in terms of some physical properties. However, especially within sea ice the dielectric properties depend on temperature and salinity which are changing more continuously with depth. With small changes in temperature and salinity between the layers, the dielectric properties also just vary slightly (Section 2.2.4). With this small dielectric contrast between the different layers, practically no reflection within the sea ice occurs. The propagation of the radiation is then only influenced by absorption and emission as we exploited in our simple incoherent model in the last section. In Figure 4.16 we discussed that for an incoherent radiation model the influence of the reflection at the layer interfaces does not depend on the thickness of the layer. This is intuitive for a thick layer but for a layer thickness $\lim_{d \rightarrow 0}$ we expect the radiation to converge to same amount as without the thin layer.

This can only be achieved taking the phase difference (Equation (2.15)) into account. The coherent solution for a multilayer reflection (Equation (2.14)) together with the Fresnel Equations (2.11) will serve as base for this discussion.

For a fixed wavelength and refractive index, the phase $P = 2\pi N\lambda^{-1}d \cos \theta$ only depends on the propagation angle and the layer thickness. For our purpose the propagation angle is

small due to the refractive index inside the sea ice, e.g., a refractive index of 1.8 (very cold sea ice or freshwater ice, Section 2.2.4), and incidence angle of 67° the cosine term takes the minimum with 0.8 within sea ice. The real part of the reflectivity (Equation (2.14)) varies with the cosine of the doubled phase. Layers much thinner than the wavelength cause only a small phase change and thus do not influence the reflectivity of the double layer interface.

By using an incoherent model (ignoring the phase), the reflectivity of a thin multilayer structure can therefore differ considerably from real measurements. We will discuss the phase and further consequences from these coherence effects in the next section.

5.2.5 Coherence effects and thickness modes

Until now in the simple incoherent model we assumed that coherence effects do not occur as they average out over footprint distances or due to spectral width of the radiometer. However, in Section 2.2 and we discussed that coherence can occur and that especially for weakly absorbing media like the snow cover, coherence can play an important role at long wavelength as the L-band. SMOS has a quite narrow receiver bandwidth of only 19 MHz (less than 2%). This makes coherence effects possible from the instrument side. For comparison, the 6.925 GHz channel of the AMSR-E instrument has a receiver bandwidth of 350 MHz (about 5%) which makes coherence effects less likely to be observed.

Kaleschke et al. [2013] and Maaß et al. [2013] used a matrix method to model brightness temperatures after Ulaby et al. [1981] for certain snow and sea ice cases in a coherent way. Here we use a recursive method described in Section 2.1 to simulate the coherence effect as modification of the reflection coefficient of a system of coherent layers. We chose a sea ice refractive index of $N_2 = 1.833 + 0.047i$ which is returned by the Vant model for sea ice salinity of 8 ppt and temperature of -15°C to be comparable to results of Kaleschke et al. [2013] and Maaß et al. [2013]. The sea water refractive index is calculated as described in Section 2.2 to $N_{\text{water}} = 9.1 + 2.3i$ for a Temperature of -1.8° and salinity of 30 ppt. We start with a single coherent layer of thin sea ice on top of the water surface. The transmissivity at nadir and at 50° incidence angle are shown in Figure 5.18. As expected, strong oscillations of the transmissivity with the ice thickness dominate over the transmissivity increase with ice thickness. For very thin ice, the transmissivity is the same as for open water. This is because the way through the ice is just a small fraction of the wavelength, so that the phase shift is negligible and the absorption and emission within the ice has no effect on the emitted radiation (Section 5.2.4). The transmissivity at vertical polarization is less affected by the coherence effects, as the 50° incidence angle is close to the Brewster angle where vertical polarized radiation passes without reflection. In horizontal transmissivity, stronger coherence effects are visible as oscillations. At nadir the effect is smaller than the effect on horizontal transmissivity but stronger than on the vertical transmissivity at 50°

incidence angle. In addition, we note a slight shift between the transmissivities at nadir and at 50° incidence angle increasing with ice thickness. This is caused by the slightly different path length within the ice between nadir and 50° observations. From looking at the phase term in Equation (2.14) we expect a phase shift of π at an ice thickness of $d = \pi \cdot (\cos(\theta_2) - 1)^{-1} = 34.2 \text{ cm}$ which can be confirmed from the figure. In addition, the transmissivity at horizontal polarization is higher than the transmissivity at vertical polarization for certain ice thickness periodically up to 30 cm thickness.

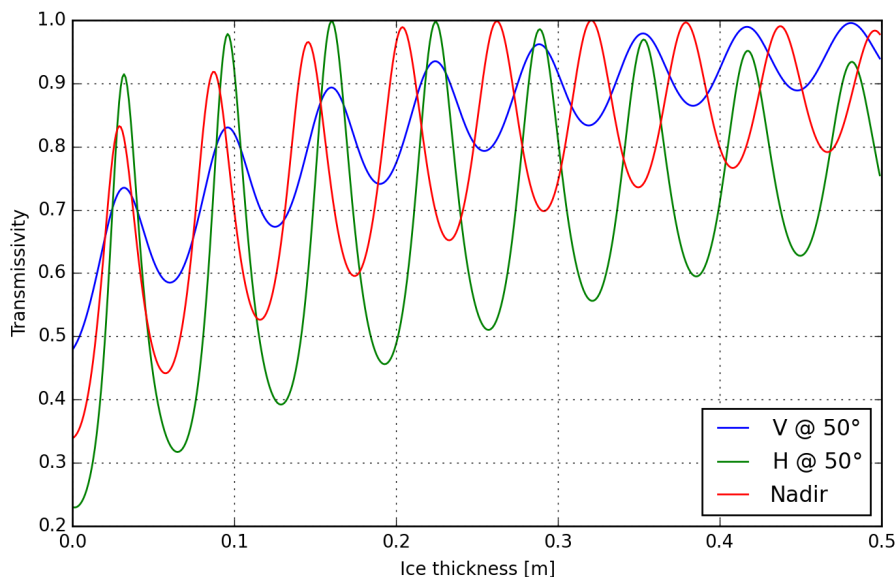


Figure 5.18: Coherent transmissivity for different thicknesses of a single sea ice layer over sea water at nadir and 50° incidence angle at both polarizations. Sea ice has -15°C and salinity of 8 ppt, Water has -1.8°C and salinity of 30 ppt.

To investigate these phenomena, we have a closer look at the incidence angle dependence of the coherence effects for thin and slightly thicker ice in Figure 5.19 a) and b), respectively. For the first few centimeter ice growth, we see increasing transmissivities up to 3 cm while 4 cm and 5 cm show lower transmissivities at nadir. For 3 cm the transmissivity is consistently higher in horizontal than in vertical polarization. At the Brewster angle marked by a gray vertical line, the vertical transmissivity increases with ice thickness. At 4 cm ice thickness, horizontal and vertical transmissivity are close together and cross at about 51° . In b) we see that with increasing ice thickness, more local maximums and minimums appear in both polarizations. The difference in transmissivity between 44 cm and 47 cm is very pronounced as they evolve in opposite directions with increasing incidence angle. However, in case of thicker ice in reality it is likely to have a much broader thickness distribution over the footprint so that we expect such effects to be averaged out entirely. At 200 cm no coherence effects are visible anymore as along the travel distance within the

ice emission and absorption dominates. Up to the 64 cm line (red) the relation between $T_{b,V}$ at the Brewster angle and the ice thickness is maintained.

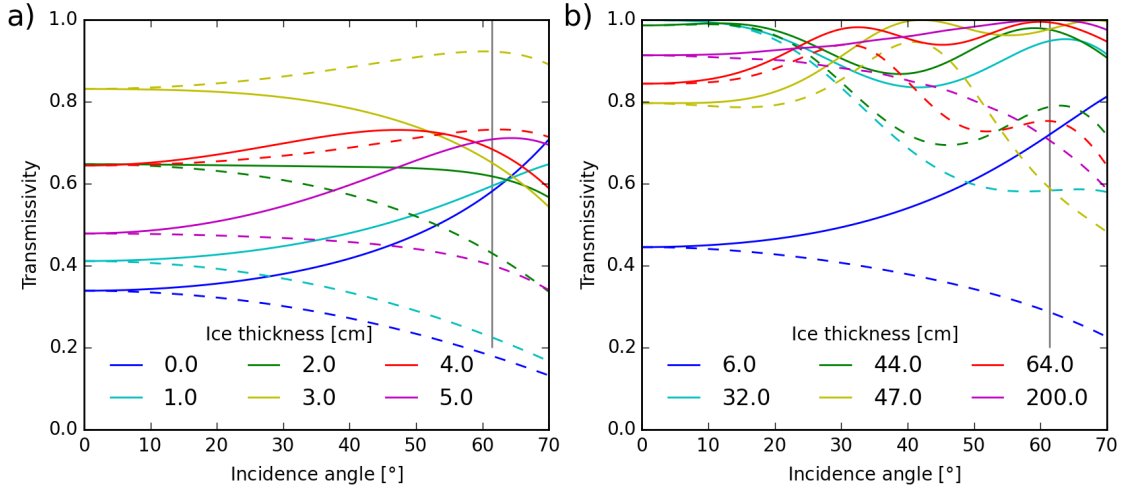


Figure 5.19: Coherent transmissivity versus incidence angle for different ice thicknesses of thin ice a) and thicker ice b). Solid line: vertical polarization, dashed line: horizontal polarization. The gray vertical line marks the Brewster angle. Same ice and water conditions as in Figure 5.18.

This variation of thicknesses within the footprint is addressed by Kaleschke et al. [2010], Menashi et al. [1993], Swift et al. [1986], Apinis and Peake [1976] using an approximation of the coherent solution for a thickness distribution for sea ice which the authors refer to as sea ice *roughness*. This roughness in terms of thickness distribution is the large scale roughness not to be confused with the small scale roughness we investigated in the Section 5.2.1 to modify the Fresnel reflection coefficients. A variable thickness as a thickness distribution in a coherent model will result in the incoherent solution, as long as the width of the distribution is in the order of the wavelength within the ice. However, for thin sea ice with $\frac{d_{ice} N_{ice}}{\lambda} \ll 1$ where the phase difference is still smaller than the wavelength within the ice the above models converge to the emissivity of open water. This semi-coherent solution is simple and fast to calculate and can be used together with other approximations for retrieval of ice thickness from SMOS data [Kaleschke et al., 2012, Tian-Kunze et al., 2014]. However, the model does not include a snow layer and is limited regarding the temperature and salinity profile. As a consequence other models were employed to investigate the influence of a snow cover on sea ice [Maaß et al., 2013, Maaß, 2013]. While we also discovered unrealistic brightness temperature changes in our incoherent MEMLS runs in Section 4.3, Maaß et al. [2015a] compared MEMLS to the model of Maaß et al. [2013] with similar results and insensitivity to snow depth. There, the same energy balance model is used so that the layer reduction within MEMLS probably joined snow and sea ice layers together as in our initial simulations. As an attempt to treat the snow and sea ice layers

separately, to address for thin coherent layers, and to discuss the influence of thickness distributions of snow and sea ice, we use an ensemble of coherent simulations in the next section.

Even though for the analysis with MEMLS in Section 4.4 we employed the frazil ice dielectric model, for the illustration of coherence it has too high absorption and emission, so that no coherent oscillation would be visible.

5.2.6 An ensemble emission model

With the experience from the previous sections with the coherent and incoherent model we compose a new model to compensate for their weaknesses. The basic idea is to calculate a massive amount of coherent simulations of slightly varying conditions within given borders employing a random number generator. We refer to this model as Combined Coherent Emission Simulations (CCES).

Basics and model requirements

Our requirements to the model are:

- broad thickness distributions should agree with incoherent models
- convergence for thin sea ice layers towards brightness temperature of open water
- show coherence effects for narrow thickness distributions
- convergence for thin snow layers on top of sea ice towards brightness temperatures of sea ice without snow
- covering SMOS incidence angle range
- taking multilayer input to reflect dielectric and temperature profile
- strong absorbing sea ice top should return the ice surface temperature at the Brewster angle in $T_{b,V}$
- consistency of results

Even though the last point seems logical as requirement to a model, as the model employs random numbers, the results can vary to some extent. In the following we will step through above list and provide examples and explanations of CCES behavior.

The physics of the model is given by the recursive Equation (2.14) which makes the model layer based. For each layer, a temperature, a refractive index, and a thickness variation is required as input. The thickness variations can be given as standard deviation of the mean thickness of each layer or as custom layer thicknesses. The latter can be useful for the input of other distributions like the log normal distribution which is sometimes

used describing ice thickness distributions [Haas et al., 2009, Tian-Kunze et al., 2014]. The method allows also multivariate input, like ice thickness depending on snow thickness, to be used.

With fixed layer thicknesses, the model converges to the solution of the normal coherent model. For determination of the brightness temperature the layer temperature weighted with the imaginary part of the refractive index is considered as in the incoherent model. This is only an approximation as the consideration of real contribution of each layer would require a more sophisticated approach because the contribution from the amplitude of the radiation emitted by each layer may differ [Wilheit, 1978]. However, the small difference in amplitude contribution of the different layers justifies this simplification.

For each individual layering, the coherent emission is modeled using Equation (2.14). From all individual modeled brightness temperatures the average is returned. If the layering input is already a thickness distribution, like SMOS would observe within its large footprint of 30 km to 50 km in diameter, The returned brightness temperatures are already weighted accordingly.

Functionality and results

The first step is to ensure the convergence to an incoherent model in case of a broad thickness distribution. The incoherent model used for comparison here accounts for all multiple reflection terms which is important for the thin ice case. We investigate the model performance for Arctic conditions for a single ice layer of -10°C with 8 ppt salinity using the Vant dielectric model. The relation of brightness temperatures to ice thickness with different thickness variations are shown in Figure 5.20. For single thickness ($\sigma_d = 0$ cm), the model shows the typical coherence effects which are stronger in $T_{b,H}$ than in $T_{b,V}$ due to the Brewster angle (Section 5.2.5). For a standard deviation of $\sigma_d = 3$ cm the CCES agrees well with the incoherent model as expected. $T_{b,H}$ of CCES with $\sigma_d = 3$ cm deviates in ice thicknesses around 20 cm only about 2 K from the incoherent model but agrees well in the lower and upper limits. $T_{b,V}$ shows larger discrepancies of up to 5 K from the incoherent model at 20 cm agrees well at thin and thick ice cases like $T_{b,H}$. In $\sigma_d = 0.1d_{\text{ice}}$ the brightness temperatures start with that of open water and show oscillations vanishing with growing ice thickness more rapidly compared to $\sigma_d = 0$ cm.

The difference between $\sigma_d = 3$ cm and the incoherent model is mostly because the incoherent model does not show the brightness temperature for an average of thicknesses but considers only the intensity at a single thickness. In this way, the slope of the brightness temperature to thickness relation introduces lower brightness temperatures from the CCES compared to the incoherent model.

For thin ice, the CCES with a $\sigma_d = 3$ cm does not converge to the brightness temperature of sea water while a fixed thickness with $\sigma_d = 0$ cm does. The normal distribution is mathematically not limited to positive ice thicknesses so that negative ice thicknesses occur

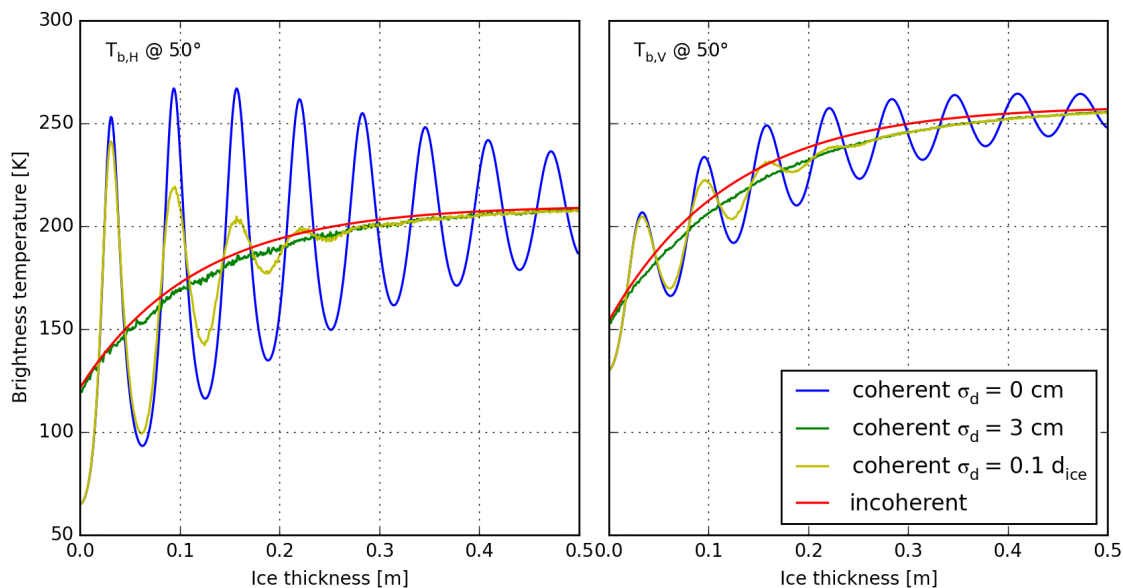


Figure 5.20: Brightness temperatures for variation of ice thickness for one ice layer with coherent, coherent with $\sigma_d = 3$ cm, thickness dependent coherent with $\sigma_d = 0.1 d_{ice}$, and incoherent radiation model using the Vant dielectric model. Left: $T_{b,H}$, right: $T_{b,V}$

which have the same oscillation with thickness as the positive ice thicknesses. Therefore, the coherent model with a distribution of ice thicknesses is close to the incoherent model at thin ice, rather than converging to the brightness temperatures of open water. Another method, which is closer to nature would be to use a log normal distribution as employed by Tian-Kunze et al. [2014]. In a log normal distribution no negative values occur but the parameters are less descriptive. We will employ a log normal distribution to ice and snow thicknesses from ice bridge data later in this section. Figure 5.20 also shows that for sea ice a normal distribution with $\sigma_d = 3$ cm sufficiently wide to smear out any coherence effects. In most cases in nature the ice thickness is expected to have a broader distribution as the ice grows while undergoing statistical processes like ridging and rafting [Thorndike et al., 1975, Wadhams, 1992, Untersteiner, 1986]. In this discussion, a single layer is used for an undistorted illustration of the coherence effects and for a better evaluation the model performance.

The snow depth on Arctic sea ice is smaller and slightly more restricted in terms of absolute scale of the snow depth distribution compared to the ice thickness distribution. However, the spacial variability of snow depth should be considered especially on ridged ice [Haapala et al., 2013]. In Figure 5.21 the model sensitivity to dry snow is shown for a thick sea ice layer of 2 m with a fixed ice temperature of $T = -10$ °C and salinity of $S = 8$ ppt using the Vant dielectric model. At this ice thickness the brightness temperatures are independent of the ice thickness distribution, due to absorption and emission within

the ice pack, as long as it does not reach into the thinner ice thickness were the emitted radiation in L-band is still sensitive to thickness variation. This means also that the phase is extinct at the sea ice top so that only the snow cover may cause coherence effects. Therefore, no dielectric profile but only a single layer is used to represent the sea ice in this particular case. In this sensitivity study of the effect from the dielectric properties and thickness of the snow, no thermodynamic implications are made regarding the ice temperature due to thermal insulation by the snow cover. Thus, the temperature and dielectric properties of the ice are independent of the snow cover.

$T_{b,V}$ is practically constant and independent of the snow cover in this simulation for an incidence angle of 50° where the vertical polarized radiation passes the snow-air interface without reflection near the Brewster angle. It can be seen from the green curve that for snow a normal distribution with $\sigma_d = 3$ cm still show oscillation in $T_{b,H}$ in the order of 10 K. With a distribution width as function of snow thickness, the coherence effects smear out with growing thickness and converge to a fixed value which is about 25 K higher than the bare ice case at 0 cm snow depth. The incoherent model gives a fixed value for the snow covered case close to the coherent snow depth dependent σ_d for thick snow covers. For a fixed snow depth ($\sigma_d = 0$ cm) and small snow depth independent variations ($\sigma_d = 3$ cm) the oscillation of $T_{b,H}$ with snow depth does not vanish as the imaginary part of the refractive index of dry snow is negligibly small (see Figure 2.4). The small ripples in the brightness temperature along the snow depth axis are caused by the averaging of the 4000 discrete coherent simulated cases for each thickness step of 0.001 m to achieve the snow depth distribution.

Maaß et al. [2013] and Maaß et al. [2015a] propose a snow depth retrieval on thick multi year ice by using a thermal equilibrium assumption. We here use the same assumption and formulation to investigate in the influence of the snow cover on top of first year ice on the brightness temperatures. This means that for a fixed ice thickness the ice temperature is determined by the snow depth. For the same conditions as in Figure 5.21 with insulation by the snow cover, the results are shown in Figure 5.22. For thin snow, the insulation effect is small and $T_{b,H}$ is similar to that of Figure 5.21. With growing snow cover, the temperature of the ice layer increases which also increases the brightness temperatures $T_{b,H}$ and $T_{b,V}$. In the incoherent model, $T_{b,H}$ shows a flat maximum at a snow depth of about 0.1 m while also the coherent oscillations become stronger with an overall decreasing trend with further increasing snow depth. $T_{b,V}$ increases up to a snow depth of about 0.2 m and then saturates. The effect of the thermal insulation of the snow cover on $T_{b,H}$ and $T_{b,V}$ is different as they result from the horizontal and vertical transmissivities through the ice and snow. The vertical transmissivity through the snow only changes slightly with a small change in dielectric contrast close to the Brewster angle while the influence on the horizontal transmissivity is stronger (see also Figure 5.17). As a consequence, $T_{b,H}$ is more sensitive to the snow cover. This effect is less pronounced when considering multi year

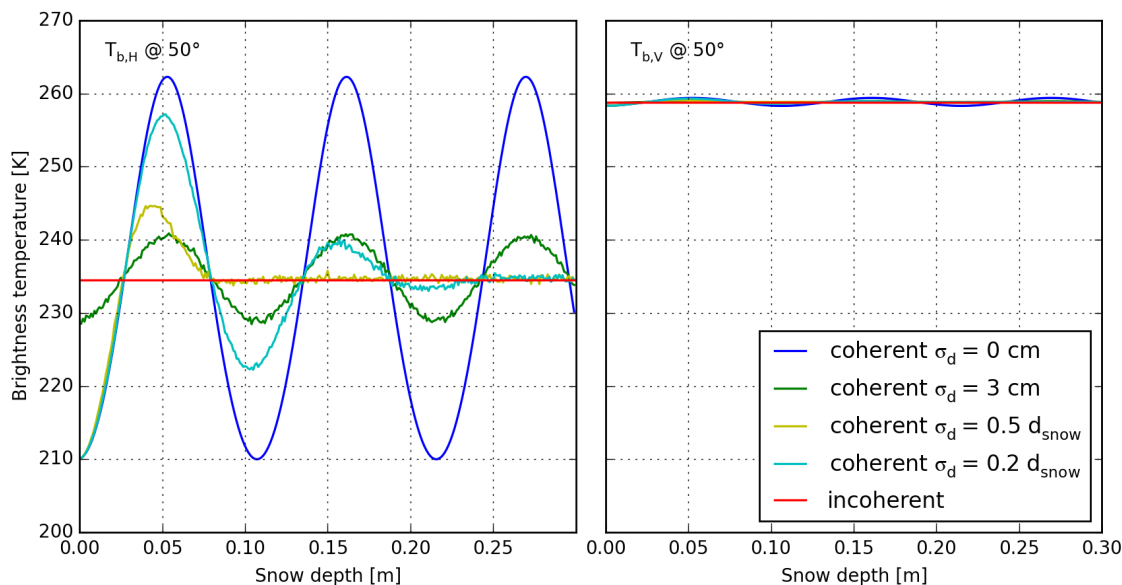


Figure 5.21: Brightness temperatures for variation of snow thickness for one ice layer of 2 m thickness. Coherent radiative transfer with snow thickness distribution of $\sigma_d = 0$ cm, 3 cm, $0.5 d_{snow}$, $0.2 d_{ice}$. Left: $T_{b,H}$, right: $T_{b,V}$.

ice, or less saline ice because the change of ice temperature causes less change of dielectric properties of the ice (not shown here). The $T_{b,V}$ in this simulation is slightly higher by about 5 K to 10 K than observed in nature over sea ice (see Figure 3.1). A possible explanation is the underestimation of the dielectric properties by the Vant dielectric model as discussed in Section 5.2.1 and the consideration of the sea ice as a single layer with bulk properties.

The CCES simulations underline that the distribution of snow thickness has to be considered, as also broad distributions relative to the mean snow thickness generate coherence effects. We will present an example of a real snow thickness distribution from NASA IceBridge data in the next paragraph.

Comparison to IceBridge data

To compare CCES to real sea ice scenarios, we obtained the IDCSI2 dataset of Operation IceBridge (OIB) from the OIB data portal <http://nsidc.org/data/idcsi2.html>. The dataset contains airborne measurements of free board, sea ice thickness, and snow depth retrieved from an airborne snow radar and a topographic mapper. From 2012 onwards most OIB flights also have surface temperature data available from infrared sensor [Kurtz, 2012, Kurtz et al., 2013]. The OIB measurements were collocated to the SMOS grid for a distance up to 25 km from each grid point center like in the EM-bird comparison (Chapter 3). We found the snow depth measurements as discrete values with unequal

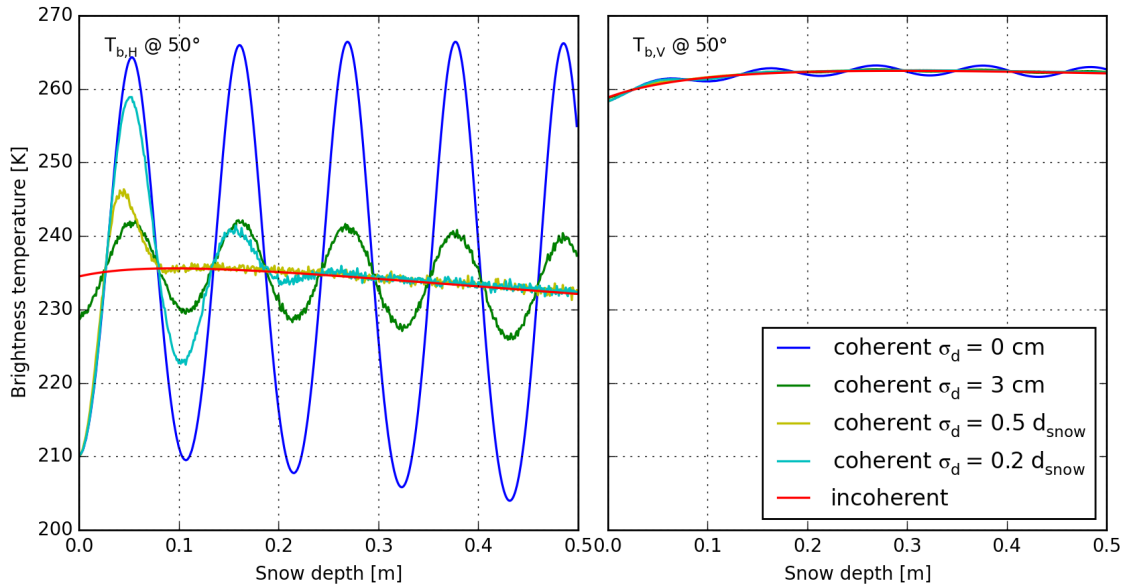


Figure 5.22: Same as Figure 5.21 but the thermal insulation is considered, so that the temperature of the ice layer is a function of snow depth.

spacing of about 2 cm on average in the OIB dataset. Discrete snow depth values together with a limited number of OIB observations for each SMOS footprint limit the conclusions to be drawn from the CCES. To overcome this restriction of limited and discrete data, several intermediate steps are performed. Firstly random noise with standard deviation of 1 cm to the data to achieve a gapless distribution. Now as the data is more evenly distributed without change of the whole distribution, we fit a log normal distribution to both, the sea ice thickness and the snow depth data. The fit turned out unstable with the original discrete data, so that the addition of small random noise was necessary. With knowledge of the parameters of the distributions of snow and ice thicknesses within the footprint, random data following this distribution can be generated. With this method, more data points can be generated aligning with the real measurements from the OIB data as input to CCES. As air temperature for the calculation of dielectric properties and brightness temperatures, the average of the infrared data from all observations within the SMOS footprint is used as the variability turned out to be rather small. The thermodynamic equilibrium temperatures of ice and snow cover was assumed to be constant over the SMOS footprint size, so that a fixed ice temperature and resulting refractive index for the ice is used.

Figure 5.23 shows an example from a single SMOS grid point, for a total of 224 OIB observations on 17 March 2014 from the Chukchi Sea. The histograms of snow depth and ice thickness are shown at the top together with the median values (red) and the fitted log-normal distributions (green). The black line shows the incoherent model result with

the median of ice thickness and snow depth, while the red and blue lines show the CCES result. The colored shaded areas show the standard deviation returned by the CCES model. These standard deviations are a measure of variability among the individual coherent simulations.

The CCES shows higher $T_{b,H}$ with increasing incidence angle and also slightly higher brightness temperatures at nadir compared to the incoherent model. The variability of the coherent simulations are also largest in $T_{b,H}$ at high incidence angles and lowest in $T_{b,V}$ for the Brewster angle for the transition from snow to air as there are no coherent oscillations as discussed before. The difference between the CCES and the incoherent model is a result from the distribution of the snow depth. Considering the peak snow depth in the histogram of around 5 cm, the comparison to Figure 5.21 reveals that many observations are in the region of highest $T_{b,H}$ while fewer observations are at low $T_{b,H}$ compared to the incoherent model. Even though the distribution is relatively broad, the coherence effect still influence the simulated brightness temperatures using CCES. Note that in Figure 5.23 in contrast to the previous figures, the frazil ice dielectric model was found to be most appropriate for the comparison to SMOS observations. As the imaginary part of the refractive index in the frazil model is high, most radiation is coming from close to the surface, therefore we set the ice temperature to the interface temperature between sea ice and snow. However, the choice of the dielectric model of the ice does not influence the coherent contribution to the brightness temperature by the snow depth distribution. Employing the Vant dielectric model mainly shifts both, $T_{b,H}$ and $T_{b,V}$ towards higher brightness temperatures (not shown here) as both, real and imaginary part of the refractive index are smaller in the Vant model (Figures 2.1 and 2.3). This leads to less reflection at the ice-snow interface and to higher penetration depth into the ice. The Vant model therefore fits the $T_{b,H}$ at high incidence angles with the incoherent model, while all other values are overestimated by the model or are inaccurate in the SMOS data (See Maaß et al. [2013]).

Repeating above procedure for all ice bridge observations from 2011 to 2014, comparing each result of CCES to the incoherent model allows us to make an estimate of the impact of coherence effects from snow to the microwave emission from sea ice at L-band. As expected $T_{b,V}$ is only little affected by these coherence effects, only 1.52 %, 0.06 %, and 0.03 % show deviations of more than 2 K, 5 K, and 10 K, respectively. For $T_{b,H}$ the effect is stronger with 12.37 %, 7.19 %, and 2.09 % show deviations of more than 2 K, 5 K, and 10 K, respectively. However, this means that most of the snow depth distributions from the OIB data are wide enough to smear out coherence effects from snow depth distributions. On the other hand most of the OIB data is taken in the Canadian Arctic in regions typical for multiyear ice with rough topography which facilitates broadening of the snow depth distribution. For level young- and first-year ice the coherence effect by snow may be stronger. Comparing SMOS observations to OIB data still follows the strong assumption that the area covered by the flight track (width in the order of ~ 10 m) is statistical representative for the entire

SMOS footprint (diameter of 30 km to 50 km).

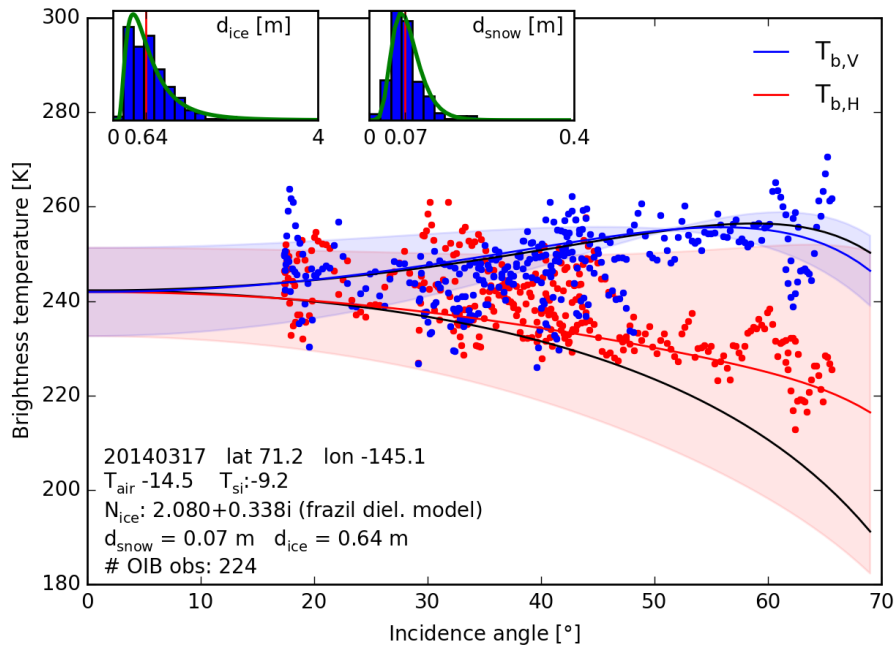


Figure 5.23: Comparison of modeled brightness temperatures (lines) for specific sea ice, snow, and temperature conditions from OIB for comparison with SMOS data (points). The black line is from the incoherent model, the blue and red lines are $T_{b,V}$ and $T_{b,H}$ from CCES, respectively. Shaded areas show standard deviations from the CCES. The histograms in the upper left show the sea ice thickness distribution (left) and the snow depth distribution (right) in blue. Median values are indicated by the red line. Green curve shows the fitted lognormal distribution which is used again as input for the CCES (for details, see text).

5.2.7 MEMLS versus simple models

To be able to compare the model performances of MEMLS and the simple incoherent and coherent models (Sections 5.2.1 and 5.2.5), an interface for the simple models was implemented for the output of the energy balance model. As the characteristics of the models differ, the direct comparison of the model outputs for each input seems meaningless, especially due to the coherent oscillations. For this reason we perform a qualitative comparison between the models by using again average relations of ice thickness versus intensity and polarization difference on the binned mean values. For MEMLS the coherent behavior is used in this comparison as in Section 4.4. Figure 5.24 shows the comparison of the modeled averages for all three models together with the empirical fit from SMOS data for the MEMLS default combination of ocean salinity and first layer salinity of 34 ppt and 22 ppt, respectively. All three models are close in both, intensity and polarization

difference along the entire ice thickness range. The largest discrepancy is seen at about 20 cm where MEMLS show higher intensity values by about 10 K while it is still lower than the empirical fit from SMOS. However, the SMOS fit was obtained in unknown surface salinity conditions which has a major influence on the brightness temperatures as discussed in Section 4.4. At high thicknesses MEMLS show slightly lower intensities compared to the simple coherent and incoherent model. The polarization difference is very similar in all three models, but is oscillating in the coherent model run. The individual results from all simulations using the coherent model is also shown in the background of Figure 5.24. Here, a strong scatter is seen in the individual coherent model results, which also explains the variability in the coherent model average.

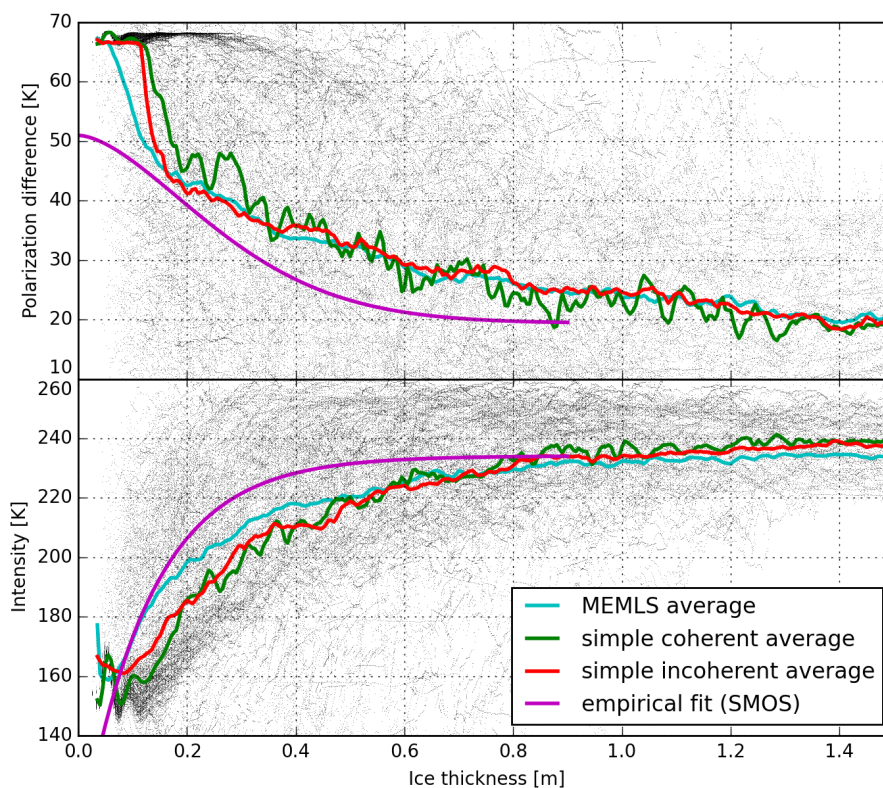


Figure 5.24: Comparison of MEMLS, the simple coherent and incoherent models (using the frazil dielectric model) and the empirical retrieval from SMOS. Ocean and first layer salinity is 34 ppt, 22 ppt, respectively. Background shows the data from the simple coherent model run.

6 | Conclusions

In this chapter we will summarize the main findings and work done in this study, namely

- (i) development and validation of an empirical thickness retrieval of thin sea ice for the Soil Moisture and Ocean Salinity (SMOS) satellite [Huntemann et al., 2014]
- (ii) adaptation and modification of an energy balance model and the sea ice version of the Microwave Emission Model of Layered Snowpacks (MEMLS) by Tonboe et al. [2011] to L-band emission
- (iii) statistical sensitivity analysis with the modified MEMLS based on more than 100.000 sea ice and snow profiles for Arctic first-year ice using the modified energy balance model and MEMLS
- (iv) development of effective representations of SMOS data using binning [Huntemann and Heygster, 2015] and two different fitting techniques
- (v) implementation of two simple (coherent and incoherent) and one ensemble (CCES) emissivity models considering only major influences on brightness temperatures and comparison to results from MEMLS

Each of these points is described in more detail below.

(i) In this study, we developed an empirical retrieval for the thickness of thin sea ice of up to 50 cm for observations of the SMOS satellite [Huntemann et al., 2014]. The retrieval was validated using AWI EM-bird measurements [Haas et al., 2009] taken from a helicopter in the Laptev Sea in March 2012. In addition, the results were compared with a MODIS ice thickness product based on nighttime thermal imagery [Mäkynen et al.,

2013]. As not much real validation data for thin ice during the Arctic freeze-up exist, a stability test over three months of retrieved ice thicknesses was performed by comparing the day-to-day fluctuations in the whole Arctic. For this product an operational daily processing chain was developed producing daily ice thickness maps of the Arctic- and Antarctic-regions. The sea ice thickness data and maps are provided to everyone under <http://www.iup.uni-bremen.de:8084/smos>. The ice thickness product is used within many projects, e.g, for the comparison to climate models within the BMBF project MiKliP, and the sensitivity study for the influence of thin ice on passive microwave based ice concentration retrieval algorithms within the ESA project SICCI.

(ii) The thermodynamic development of sea ice and the corresponding microwave emission at L-Band was modeled using an energy balance model and the sea ice version of the Microwave Emission Model of Layered Snowpacks (MEMLS) [Tonboe et al., 2011, Tonboe, 2005]. Here the sea ice formation and evolution of 18 selected first year ice regions within the Arctic was modeled from atmospheric data from the European Centre for Medium-Range Weather Forecasts (ECMWF) ERA-40 atmospheric model [European Centre for Medium-Range Weather Forecasts, 2004]. For the resulting 283 usable time series, more than 100.000 sea ice and snow cover profiles were extracted and passed to MEMLS. The limited agreement with the empirical retrieval enforced a review of the modeling of physical processes within the energy balance model and MEMLS. Several modifications and improvements were made to both models, starting from correction of small errors in the source code, over correcting too much simplified assumptions, up to the revision of the layer management within MEMLS. The MEMLS simulations after these corrections show better agreement with the empirical retrieval from SMOS even though with a considerably large spread between individual model runs. The details of the modifications made to the energy balance model and MEMLS are reported back to the authors of this model combination [Tonboe et al., 2011].

(iii) From the simulations with the energy balance model and MEMLS, it turned out that the sensitivity to ice thickness at L-band does not have to originate from the deep penetration but also can arise from the physical correlation of surface temperature and snow depth to the ice thickness. Also, the salinity of the surface layer was found to have a major influence on the emitted radiation. For saturation of the radiation with ice thickness at about 1 m, the difference between a surface salinity 10 ppt and 22 ppt made a difference of more than 5 K and shows even higher differences of up to 30 K for ice for smaller thicknesses from 5 cm to 20 cm (Section 4.4.1). In these simulations a strong correlation of ice thickness to air temperature and thus to surface temperature appeared. This correlation was found to be the major reason for the relation of ice thickness to brightness temperature in our simulated scenarios. The comparison of snow depth to brightness temperatures re-

vealed coherent oscillations at small snow depth. These oscillations were found to cause a maximum difference in intensity and polarization difference over a mean of all simulations of more than 30 K between snow depth of 4 cm and 8 cm (Section 4.4.2). This explained also the large spread in the relation of ice thickness to brightness temperature among the individual profiles (Sections 4.3.7 and 4.4.2).

(iv) From experience with SMOS data processing and from the findings during the modification of MEMLS and the energy balance model, more sophisticated methods for SMOS data handling were developed. These include the binning of brightness temperatures to single incidence angle bins [Huntemann and Heygster, 2015], as well as two fit functions for the dependence of brightness temperature to incidence angle. An exponential fit function, fitting horizontal and vertical polarized brightness temperatures ($T_{b,H}$ and $T_{b,V}$) independently, and a fit function based on the physical relation of the Fresnel equations, fitting $T_{b,H}$ and $T_{b,V}$ simultaneously. Even though the fit quality of the Fresnel fit shows satisfying results, the fit parameters which effectively representing the refractive indices of snow and sea ice showed strong fluctuations for two test regions in the Antarctic. Both fit functions were found to be applicable in the incidence angle range of up to about 55° . To eliminate unphysical outliers due to the SMOS image reconstruction or due to Radio Frequency Interference (RFI) we employ an iterative approach of fitting and outlier removal for both fit methods. Reconstructing the brightness temperatures from the incidence angle dependence saves space so that resulting internal data containers require more than 200 times less space on hard drives compared to already compressed raw data.

(v) As the modeled results from the rather complex MEMLS model were understandable with considering only few simple physical processes, two simple models, one coherent and one incoherent were implemented for comparison. These models served as basis for further investigation of yet unconsidered effects like variations of dielectric properties of the ice and the influence of the interface roughness. With the incoherent model three different dielectric models to connect the dielectric properties of ice with its microphysical structure, i.e., small brine inclusions, were investigated: two mixture models, with random oriented needles and spherical inclusions [Shokr, 1998], and one empirical model [Vant et al., 1978] (Section 2.2). The differing characteristics of the dielectric models were found to translate directly to the modeled brightness temperatures. Thus, the choice of the dielectric model is crucial for the relation of brightness temperatures to ice thickness. Even in case of saturation of the brightness temperatures with ice thickness, the model results differ considerably (Section 5.2.1).

Thin layers cause unrealistic jumps in the brightness temperatures in incoherent models (Section 4.3.7, [Maaß et al., 2013, Kaleschke et al., 2013]), so that a second model was used to investigate in coherence effects by including the phase information for the propagation

of the radiation. $T_{b,V}$ was found to be much less influenced by coherence effects, especially close to the Brewster angle. Nevertheless, coherent oscillations of the brightness temperatures with increasing thickness make the coherent model not representing observations adequately. Homogeneous ice thicknesses are not expected to be observed within the scale of a SMOS footprint and in combination with individual snow depth, the coherent simulations are even less representative [Maaß, 2013, Kaleschke et al., 2013]. As an attempt to treat thickness distributions of snow and sea ice without ignoring the phase information, a third model was set up. The Combined Coherent Emission Simulations (CCES) model in principle simulates each case of snow and ice thickness of the distribution and returns the mean brightness temperatures which would be seen by the instrument observing the distribution. The CCES results were compared to incoherent simulations on real snow depth and ice thickness distributions obtained from airborne Operation IceBridge (OIB) observations from 2010 to 2014. While $T_{b,V}$ showed nearly no difference between the CCES and the incoherent model, $T_{b,H}$ yield higher discrepancies of up to more than 10 K in some cases (Section 5.2.6).

A comparison of the mean intensities and polarization differences to ice thickness between MEMLS, the coherent, and the incoherent model showed good agreement with all input profiles from the energy balance model. The empirical relation from SMOS was found to give slightly higher intensities and lower polarization differences for medium ice thickness of 15 cm to 40 cm, but agreed well in the saturation at higher ice thicknesses with the models (Section 5.2.7).

The different dielectric models investigated in this study showed different features and signs of applicability to certain types of models.

The empirical *Vant* dielectric model shows good agreement when used as a single ice layer in previous studies, suggesting a moderate sensitivity to ice thickness [Maaß et al., 2013, Maaß, 2013, Kaleschke et al., 2013]. *Single layer* means in this context that the ice has a uniform temperature and salinity through the ice column. Due to the high contrast in permittivity at the sea ice bottom, only a small amount of radiation penetrates from the water into the ice. Emission and absorption cause an increase of the radiation propagating through the ice towards the ice-air interface. The emitted radiation is partly transmitted through the ice top layer depending on the polarization. The water-ice and ice-air interfaces do not change much (only due to temperature change of the whole ice layer), so that a direct sensitivity to ice thickness is suggested by the absorption and emission in the ice. As the ice-air interface has similar conditions in the single layer model independent of the ice thickness, the resulting polarization difference does not vary much. The *Vant* dielectric model is supposed to work in cold and not too saline conditions so that for a dielectric profile of sea ice, the model is out of its valid range at the saline sea ice top and the warm sea ice bottom. In these cases the model gives too small permittivities, so that results

are similar to that, when modeled a single ice layer with bulk properties (Sections 5.2.1 and 5.2.2, Maaß [2013], Kaleschke et al. [2013]).

For the random *frazil* dielectric model, a single layer approach gives nearly no sensitivity to ice thickness due to much stronger absorption and emission compared to the Vant model. However, the random frazil dielectric model is used in MEMLS with a temperature and salinity profile modeled by the thermodynamic energy balance model. It agrees well with the empirical fit of ice thickness to intensity and polarization difference developed in this study (Chapter 3, Section 4.3, and Figure 4.19).

The *columnar* dielectric model, where the inclusions are modeled as spherical, showed unrealistic small absorption for typical ice temperatures and salinities. It suggests a penetration depth into the ice of several meters which we consider not representative for the saline first year ice (Section 5.2.1).

Considering only variations of transmissivities through the ice-snow-air boundary, the variations of temperature, salinity and inclusion geometry (in terms of choice of a dielectric model), strong variations in modeled brightness temperatures for a given ice thickness occur. The effect is more pronounced $T_{b,H}$ (up to 30 K) and less pronounced in $T_{b,V}$ (up to 10 K) for temperatures below 260 K. The variability increases when considering higher temperatures or include the effect of surface roughness mainly for $T_{b,H}$ (Sections 5.2.2 and 5.2.3).

Within the energy balance model used in this study, snow and sea ice are modeled as a profile of several layers. As a result, the sea ice bottom has a temperature similar to that of water. This results in a higher fraction of liquid brine, which in turn increase the permittivity of the lower layers. The permittivity of sea water is higher that of cold sea ice, so that the contrast in permittivity at the water-ice boundary is lower compared to the contrast when the sea ice is modeled as a single layer. Thus, more radiation is penetrating from the water into the ice. The sea ice top is then the main valve for the emitted radiation. For warmer surface conditions, the permittivity contrast between ice and air is higher so that less radiation can penetrate through this interface.

For thin ice, the ice-air interface is warmer compared to thick ice and is cooled as the ice grows. The snow accumulating on top introduces a step between the permittivity of sea ice and that of air, which increases the radiation penetrating through this interface. The decrease of the temperature of the uppermost sea ice layer and the snow accumulation on top is found to be the major cause of the increase in brightness temperature during the ice growth phase, when using the energy balance model and MEMLS (Section 4.4.3). Furthermore, the snow cover causes an increase of the brightness temperature in the incoherent mean but also causes coherent oscillations at smaller snow depth.

The following, yet unconsidered, effects in the energy balance model and MEMLS, may support the relation of brightness temperatures to ice thickness: The water-ice-interface

(Figure 5.14) becomes more rough during ice grows due to brine expulsion [Petrich and Eicken, 2010] so that more radiation from the water can enter the sea ice layer. In addition, at the ice-snow-air interface the brine gets soaked from the ice surface into the snow cover due to capillary effects, which further lowers the dielectric contrast at the surface and thus increases the emitted radiation.

The interface conditions at the sea ice bottom are discussed to mainly modify the emitted radiation, whereas the surface properties have a stronger influence on the polarization of the emitted radiation (Section 5.2.3).

For accurate modeling of the brightness temperatures, the thermodynamic ice growth and resulting profile properties should be taken into account. The transmissivity through the bottom of the sea ice was found to be a big uncertainty which requires more investigation in terms of roughness, permittivity contrast, and thickness of transitional layers (Sections 5.2.2 and 5.2.4).

Another source of uncertainty in current modeling approaches, is the assumption of the inclusion geometry for the mixture models for the formulation of dielectric properties of sea ice. Temperatures variations within the ice are promoting the formation of brine channels which leads to desalination and change of inclusion geometry which is not modeled in the thermodynamic model used in this study. As a consequence, the brine inclusions may also have more oriented structures such as vertically oriented needles or ellipsoids. This is often not represented in emissivity models (also not in this study). Oriented inclusion geometries requires a special treatment as the ice becomes a birefringent medium. In this case, the propagation direction of the radiation within the ice depends on the polarization. Birefringence together with varying sea ice properties along the profile requires a more complex model like a Dense Media Radiative Transfer (DMRT) or Strong Fluctuation Theory (SFT) approach [Mätzler, 1998, Picard et al., 2013, Stogryn, 1987, Johnsen, 1998]. Even though, the dielectric models used in this study cover a wide range of permittivities, in nature the permittivities may vary continuously within certain borders, depending on temperature, salinity and geometry of the inclusions [Shokr, 1998, Golden, 1995].

In this study the initiation of the ice growth for the thermodynamic model from the atmospheric conditions turned out to be another uncertainty. The sea ice flag in the ECMWF ERA 40 data seems not a sufficient indicator as in some cases positive air temperatures are present during first occurrence of sea ice. Even with an additional requirement of -8°C air temperature for ice formation, the ice surface temperature increased in most cases during the first time steps of the thermodynamic energy balance model (Section 4.4.3). This indicates that either the initiating sea ice conditions, the initial time of the sea ice formation, or the energy balancing contributions need further investigation.

For future studies we suggest a review of the thermodynamic model coupling with the emission model to include certain processes of the ice formation. For example the ice type

and the way the dielectric properties of the ice layers are calculated could be coupled with the wind speed, so that in windy condition more frazil ice is forming while calm conditions producing more columnar ice. For a better general representation of sea ice within the energy balance model, an integration of a more sophisticated sea ice evolution model, such as the model by Bitz and Lipscomb [1999] or the HIGHTSI model [Cheng et al., 2013], is suggested.

Within the more than five years of operational SMOS observations, more and more data sets of sea ice thickness from in situ measurements became available. With the knowledge about the possible influences on the brightness temperatures we also presented in this study, a new retrieval may be developed taking these influence into account.

Another approach is a statistical parameter estimation based on the available SMOS data. Evolutions of brightness temperature over a longer time period can be analyzed and compared to the expected variabilities and influences estimated in this study. This is meant as an extended approach of the day-to-day ice thickness difference analysis which we performed for the empirical ice thickness retrieval (Section 3.2.3). With the methods presented in Section 5.1 this investigation may be simplified.

In this analysis, the limited features of the thermodynamic model did not allow a detailed investigation of the different geophysical influences on the brightness temperatures. With an improvement of the thermodynamic model, a large amount of input data from climate models may be used in order to simulate proper sea ice profiles. The resulting database may provide statistical information on certain sea ice and snow conditions and corresponding brightness temperatures. This way, the sensitivities of individual parameters, cross correlations, and requirements, can be studied.

SMOS were found to have higher uncertainties in certain incidence angle ranges and also shows slight ringing effects in the snapshots in case of RFI or in areas with high brightness temperature contrasts like close to the coast Zine et al. [2007, 2008], Camps et al. [2010]. In addition to SMOS, data from other instruments on board satellites such as Aquarius or SMAP, which are supposed to have a higher accuracy for single observations, may be used. Synergies with external data like ice surface temperature or snow depth from AMSR2 may also be beneficial for future investigations and improvement of ice thickness retrievals from SMOS.

The presented empirical retrieval of thin sea ice thickness from SMOS [Huntemann et al., 2014] is expected to work on Arctic sea ice on statistical prevailing situations with the expected relative uncertainty of 30% (Chapter 3). In the Antarctic, more turbulent conditions lead to more frazil ice so that the emitted radiation is reduced and the retrieval may underestimate the ice thickness. For ice without snow cover, the retrieval will also underestimate the ice thickness. For sea ice cases with a narrow snow depth distribution with a standard deviation of up to 5 cm, a higher uncertainty is expected due to coherence effects.

To summarize, the retrieval of sea ice thickness in L-band is a challenging topic due to lack of understanding of how various macro and micro physical properties of sea ice and snow affect the measured SMOS signal. The extensive sea ice modeling performed in this study helped to understand the effect of some of these parameters and thus are a step towards a physical and not purely empirical retrieval of sea ice thickness. To advance in the direction of such a new retrieval, further investigation and modeling of the effect of temperature profile, surface roughness, desalination and snow properties are needed. Another yet unresolved issue is the lack of in situ data on thin sea ice which makes the development of sea ice thickness retrievals even more challenging.

A | Appendix

A.1 Dielectric constant of brine

Below are the detailed formulations of brine dielectric properties how it is approximated. The formulas below are also summarized in [Ulaby et al., 1986, Shokr and Sinha, 2015]. Corrections for the calculation of the dielectric constant mentioned in Section 4.3 are highlighted.

The dielectric constant of brine is a function of the brine normality and temperature. The brine normality N_b can be derived from the brine salinity S_b as

$$N_b = 1.707 \times 10^{-2} S_b + 1.205 \times 10^{-5} S_b^2 + 4.058 \times 10^{-9} S_b^3 \quad (\text{A.1})$$

for NaCl solutions, while for the normality of sea water a factor of 0.9141 may be applied. Equation (A.1) is valid for salinities up to 260 ppt according to Ulaby et al. [1986], Klein and Swift [1977]. The dielectric constant of brine is then

$$\epsilon'_b = \epsilon_{b\infty} + \frac{\epsilon_{b0} - \epsilon_{b\infty}}{1 + (2\pi f \tau_b)^2} \quad (\text{A.2})$$

$$\epsilon''_b = \frac{\sigma_b}{2\pi f \epsilon_0} + (2\pi f \tau_b) \frac{\epsilon_{b0} - \epsilon_{b\infty}}{1 + (2\pi f \tau_b)^2} \quad (\text{A.3})$$

with ϵ_{b0} as low-frequency limit of ϵ_b , $\epsilon_{b\infty} = 4.9$ as high-frequency limit of ϵ_b , σ_b as the ionic conductivity of brine, f as the frequency in GHz, τ_b as the relaxation time of brine and ϵ_0 as the free space permittivity ($8.854 \times 10^{-2} \text{ F m}^{-1}$). ϵ_{b0} , τ_b , and σ_b are a function of the

temperature and normality given by

$$\epsilon_{b0}(T, N_b) = \epsilon_{b0}(T_0)a_1(N_b) \quad (\text{A.4})$$

$$\tau(T, N_b) = \tau_{b0}(T, 0)b_1(T, N_b) \quad (\text{A.5})$$

$$\sigma_b(T, N_b) = \sigma_b(25, N_b)c_1(\Delta, N_b) \quad (\text{A.6})$$

$$(\text{A.7})$$

with $\Delta = 25 - T$ (in °C) and ϵ_{b0} as static dielectric constant of brine with zero normality, i.e., of pure water. Which was determined by Klein and Swift [1977] using a regression to

$$\epsilon_{b0} = 88.045 - 0.4147T + 6.295 \times 10^{-4}T^2 + 1.075 \times 10^{-5}T^3. \quad (\text{A.8})$$

$\tau_b(T, 0)$ was obtained by a fit by Stogryn [1971] with

$$2\pi\tau_{b0}(T) = 1.1109 \times 10^{-10} - 3.824 \times 10^{-12}T + 6.938 \times 10^{-14}T^2 - 5.096 \times 10^{-16}T^3 \quad (\text{A.9})$$

The other functions are given by

$$\sigma_b(25, N_b) = N_b(10.39 - 2.378N_b + 0.683N_b^2 - 0.135N_b^3 + 1.01 \times 10^{-2}N_b^4), \quad (\text{A.10})$$

$$a_1(N_b) = 1.0 - 0.255N_b + 5.15 \times 10^{-2}N_b^2 - 6.89N_b^3, \quad (\text{A.11})$$

$$b_1(T, N_b) = 1.0 + 0.146 \times 10^{-2}TN_b - 4.89 \times 10^{-2}N_b - 2.97 \times 10^2N_b^2 + 5.64 \times 10^{-3}N_b^3, \quad (\text{A.12})$$

$$c_1(\Delta, N_b) = 1.0 - 1.96 \times 10^{-2}\Delta + 8.08 \times 10^{-5}\Delta^2 - N_b\Delta (3.02 \times 10^{-5} + 3.92 \times 10^{-5}\Delta + N_b(1.75 \times 10^{-5} - 6.58 \times 10^{-6})) \quad (\text{A.13})$$

The green + in Equation (A.12) was a - and the red parenthesis in Equation (A.13) were missing in the sea ice version of MEMLS which led to higher loss values before the correction in Section 4.3.

A.2 Collection of dielectric mixture models

If the dielectric properties of a host an inclusion is known, then dielectric mixture formulas may describe the dielectric properties of the mixture. Here the most common dielectric mixture models for brine inclusions are listed [Shokr, 1998]. The notation follows literature convention with the following meanings: V_i is the volume fraction of the inclusions, ϵ_h and ϵ_i are the permittivity of the host and the inclusion respectively, ϵ_m is the dielectric constant of the mixture. For small volume fractions $V_i < 0.1$ is $\epsilon_m^* = \epsilon_h$ while for $V_i > 0.1$ the mixture formulas are used recursively with $\epsilon_m^* = \epsilon_m$ of the previous iteration, starting with

$\epsilon_m^* = \epsilon_h$. For sea ice and resulting mixtures, these formulas converge after a few iterations.

A.2.1 Random needle inclusions

Random needle inclusions can be found in ice formed in rough weather conditions. This model is referred to as the *frazil* dielectric model within this document.

$$\epsilon_m = \epsilon_h + \frac{V_i}{3} \left(\frac{\epsilon_i - \epsilon_h}{\epsilon_i + \epsilon_m^*} \right) (5\epsilon_m^* + \epsilon_i) \quad (\text{A.14})$$

Equation (A.14) leaves the dielectric constant of the mixture isotropic, i.e., independent of the propagation direction of the radiation.

A.2.2 Spherical inclusions

Spherical inclusions may be found in frazil, granular and columnar structures and also suits the shape of air bubbles in multi year ice. This model is referred to as the *columnar* dielectric model within this document. The dielectric constant of the mixture with spherical inclusions can be described as

$$\epsilon_m = \epsilon_h + 3V_i\epsilon_m^* \left(\frac{\epsilon_i - \epsilon_h}{\epsilon_i + 2\epsilon_m^*} \right) \quad (\text{A.15})$$

The Equation (A.15) also leaves the dielectric constant of the mixture isotropic.

A.2.3 Vertically oriented needle inclusions

Commonly found in sea ice are brine inclusions forming vertical oriented needles. In this case, the mixture becomes anisotropic so that the dielectric constant depends on the propagation direction of the radiation. Defining the $X - Y$ -plane as the ice surface plane, then the Z -axis is the needle orientation and $\epsilon_{m,x} = \epsilon_{m,y}$

$$\begin{aligned} \epsilon_{m,x} &= \epsilon_h + 2V_i\epsilon_m^* \frac{\epsilon_i - \epsilon_h}{\epsilon_i + \epsilon_m^*} \\ \epsilon_{m,z} &= \epsilon_h + V_i(\epsilon_i - \epsilon_h) \end{aligned} \quad (\text{A.16})$$

A.3 Empirical model for dielectric constant of sea ice after Vant

Vant et al. [1978] provided an empirical formulation for the dielectric constant for first-year and multiyear sea ice with a linear fit. For 1.4 GHz the fit parameters may be interpolated.

So that the dielectric constant for first-year ice can be expressed as

$$\begin{aligned}\epsilon' &= 3.1 + 0.0084 V_b \times 10^3 \\ \epsilon'' &= 0.037 + 0.00445 V_b \times 10^3\end{aligned}\tag{A.17}$$

and for multiyear ice

$$\begin{aligned}\epsilon' &= 3.1 + 0.0084 V_b \times 10^3 \\ \epsilon'' &= 0.0028 + 0.00436 V_b \times 10^3\end{aligned}\tag{A.18}$$

Where V_b is the brine volume fraction.

A.4 Dielectric constant of snow

The dielectric constant of snow is derived as within the MEMLS model after [Matzler, 1996]

$$\epsilon' = 1 + 1.5995\rho_s + 1.861\rho_s^3 \quad \text{for } \rho < 400 \text{ kg m}^{-3}\tag{A.19}$$

$$\epsilon' = (1 - \nu)\epsilon_h + \nu\epsilon_s \quad \text{for } \rho > 400 \text{ kg m}^{-3}\tag{A.20}$$

with $\epsilon_h = 1.0$, $\epsilon_s = 3.215$ and $\nu = \rho/917 \text{ kg m}^{-3}$

The imaginary part is after [Tiuri et al., 1984] and [Mätzler, 2006]:

$$\epsilon'' = \epsilon_i''(0.52\rho + 0.62\rho^2)\tag{A.21}$$

with $\epsilon_i'' = \alpha f^{-1} + \beta f$ where

$$\alpha = (0.00504 + 0.0062) \cdot \exp(-22.1 \cdot \theta)\tag{A.22}$$

$$\theta = \frac{300 \text{ K}}{T} - 1\tag{A.23}$$

$$\beta = \frac{B_1}{T} \cdot \frac{\exp(b/T)}{(\exp(b/T) - 1)^2} + B_2 f^2 + \exp(-9.963 + 0.0372 \cdot (T - 273.16 \text{ K}))\tag{A.24}$$

where T is the temperature in K, f is the frequency in GHz, $B_1 = 0.0207 \text{ K GHz}^{-1}$, $b = 335 \text{ K}$ and $B_2 = 1.16 \cdot 10^{-11} \text{ GHz}^{-3}$

A.5 Tables for empirical formulas

Table A.1: Table of coefficients for brine volume fraction from Equation (2.18)

T [°C]	a_1	b_1	c_1	d_1
$0 \geq T > -2$	-0.041221	-18.407	0.58402	0.21454
$-2 \geq T \geq -22.9$	-4.732	-22.45	-0.6397	-0.01074
$-22.9 > T \geq -30$	9899	1309	55.27	0.7160
T [°C]	a_2	b_2	c_2	d_2
$0 \geq T > -2$	0.090312	-0.016111	$1.2291 \cdot 10^{-4}$	$1.3603 \cdot 10^{-4}$
$-2 \geq T \geq -22.9$	0.08903	-0.01763	$-5.330 \cdot 10^{-4}$	$-8.801 \cdot 10^{-6}$
$-22.9 > T \geq -30$	8.547	1.089	0.04518	$5.819 \cdot 10^{-4}$

Table A.2: Table of coefficients for brine salinity from Assur [1960] for Equation (2.19)

T [°C]	a	b	c	d
$-2 \geq T \geq -8.2$	1.725	-18.756	-0.3964	0.
$-8.2 \geq T \geq -22.9$	57.041	-9.929	-0.16204	0.002396
$-22.9 \geq T \geq -36.8$	242.94	1.5299	0.0429	0.
$-36.8 \geq T \geq -43.2$	508.18	14.535	0.2018	0.

List of acronyms

AMSR2	Advanced Microwave Scanning Radiometer 2
AMSR-E	Advanced Microwave Scanning Radiometer - EOS
ARTIST	Arctic Radiation and Turbulence Interaction STudy
ASAR	Advanced Synthetic Aperture Radar
ASI	ARTIST Sea Ice
ASR	Arctic System Reanalysis
AWI	Alfred Wegener Institute
BLAS	Basic Linear Algebra Subprograms
BMBF	Federal Ministry of Education and Research / Bundesministerium für Bildung und Forschung
BUFR	Binary Universal Form for the Representation of meteorological data
CCES	Combined Coherent Emission Simulations
CFDD	Cumulative Freezing Degree days
ClimVal	Climate model Validation
DGG	Discrete Global Grid
DMI	Danish Meteorological Institute

DMRT	Dense Media Radiative Transfer
ECMWF	European Centre for Medium-Range Weather Forecasts
EOS	Earth Observing System
ESA	European Space Agency
ESMR	Electrically Scanning Microwave Radiometer
ESSReS	Earth System Science Research School
FLS	First Layer Salinity
FMI	Finish Meteorological Institute
HIGHTSI	one-dimensional HIGH-resolution Thermo-dynamic Snow/Ice model
HIRLAM	High Resolution Limited Area Model
ISEA	Icosahedron Snyder Equal Area
IUP	Institute für UmweltPhysik
JRA	Japanese ReAnalysis
L-MEB	L-band Microwave Emission of the Biosphere
MEMLS	Microwave Emission Model of Layered Snowpacks
MIRAS	Microwave Imaging Radiometer with Aperture Synthesis
MLT	Maximum Layer Thickness
MODIS	Moderate-resolution Imaging Spectroradiometer
MiKliP	Midterm Climate Prognosis/Mittelfristige Klimaprognose
NASA	National Aeronautics and Space Administration
NCAR	National Center for Atmospheric Research
NCEP	National Centers for Environmental Prediction
NRT	Near Real Time
NSIDC	National Snow and Ice Data Center
NetCDF	Network Common Data Format
OIB	Operation IceBridge

OSI-SAF	Ocean and Sea Ice Satellite Application Facility
OS	Ocean Salinity
PHAROS	PHysical Analysis of RemOte Sensing images
PNG	Portable Network Graphics
RFI	Radio Frequency Interference
RMSD	root mean square deviation
SAC-D	Satelite de Aplicaciones Cientificas-D
SAR	Synthetic Aperture Radar
SFT	Strong Fluctuation Theory
SICCI	Sea Ice - Climate Change Initiative
SIC	Sea Ice Concentration
SIDARUS	Sea Ice Downstream services for Arctic and Antarctic Users and Stakeholders
SIT	Sea Ice Thickness
SMAP	Soil Moisture Active Passive
SMMR	Scanning Multi-channel Microwave Radiometer
SMOS	Soil Moisture and Ocean Salinity
SSMIS	SSM/I / Sounder
SSM/I	Special Sensor Microwave Imager
TOPAZ	Towards an Operational Prediction system for the North Atlantic European coastal Zones

Bibliography

- R. N. Adams and Denman Eugene D. *Wave propagation and turbulent media*. American Elsevier Pub. Co New York, 1966.
- J. J. Apinis and W. H. Peake. Passive microwave mapping of ice thickness. Technical report, Ohio State University, 1976.
- A. Assur. Composition of sea ice and its tensile strength. Technical report, U.S. Army Snow, Ice and Permafrost Research Establishment, Wilmette, Ill., 1960.
- G. I. Belchansky, D. C. Douglas, and N. G. Platonov. Duration of the Arctic sea ice melt season: Regional and interannual variability, 1979-2001. *Journal of Climate*, 17(1):67–80, 2004. ISSN 08948755. doi: 10.1175/1520-0442(2004)017<0067:DOTASI>2.0.CO;2.
- R. Bellman and G. M. Wing. *An Introduction to Invariant Imbedding*, 1975.
- M. Bilello. Formation, growth, and decay of sea-ice in the Canadian Arctic Archipelago. *Arctic*, 1961.
- C. M. Bitz and W. H. Lipscomb. An energy-conserving thermodynamic model of sea ice, 1999. ISSN 0148-0227.
- M. Brown, F. Torres, I. Corbella, and A. Colliander. SMOS Calibration. *IEEE Transactions on Geoscience and Remote Sensing*, 46(3):646–658, mar 2008. ISSN 0196-2892. doi: 10.1109/TGRS.2007.914810.
- E. Brun, P. David, M. Sudul, and G. Brunot. A numerical model to simulate snow-cover stratigraphy for operational avalanche forecasting. *Journal Of Glaciology*, 38(128):13–22, 1992. ISSN 00221430.

- W. J. Burke, T. Schmugge, and J. F. Paris. Comparison of 2.8- and 21-cm Microwave Radiometer Observations Over Soils With Emission Model Calculations. *Journal of Geophysical Research*, 84(C1):287, 1979. ISSN 0148-0227. doi: 10.1029/JC084iC01p00287.
- Byrd Polar Research Center - The Ohio State University. Arctic System Reanalysis (ASR) Project, 2012.
- A. Camps, J. Gourrion, J. M. Tarongi, A. Gutierrez, J. Barbosa, and R. Castro. RFI Analysis in SMOS Imagery. In *Geoscience and Remote Sensing Symposium (IGRASS proceedings 2010)*, pages 2007–2010, 2010.
- R. Castro. Analytical Pixel Footprint. Technical report, DEIMOS Engenharia, 2008.
- C. M. Chang and H. P. D. Shieh. Simple formulas for calculating wave propagation and splitting in anisotropic media. *Japanese Journal of Applied Physics, Part 1: Regular Papers and Short Notes and Review Papers*, 40(11):6391–6395, 2001. ISSN 00214922. doi: 10.1143/JJAP.40.6391.
- B. Cheng, M. Mäkynen, M. Similä, L. Rontu, and T. Vihma. Modelling snow and ice thickness in the coastal Kara Sea, Russian Arctic. *Annals of Glaciology*, 54(62):105–113, jul 2013. ISSN 02603055. doi: 10.3189/2013AoG62A180.
- B. J. Choudhury, T. J. Schmugge, A. Chang, and R. W. Newton. Effect of Surface Roughness on the Microwave Emission From Soils. *Journal of Geophysical Research*, 84(C9):5699, 1979. ISSN 0148-0227. doi: 10.1029/JC084iC09p05699.
- J. Comiso, D. Cavalieri, and T. Markus. Sea ice concentration, ice temperature, and snow depth using AMSR-E data. *IEEE Transactions on Geoscience and Remote Sensing*, 41(2):243–252, feb 2003. ISSN 0196-2892. doi: 10.1109/TGRS.2002.808317.
- I. Corbella, F. Torres, A. Camps, A. Colliander, M. Martin-Neira, S. Ribo, K. Rautiainen, N. Duffo, and M. Vall-llossera. MIRAS end-to-end calibration: application to SMOS L1 processor. *IEEE Transactions on Geoscience and Remote Sensing*, 43(5):1126–1134, may 2005. ISSN 0196-2892. doi: 10.1109/TGRS.2004.840458.
- G. F. N. Cox and W. F. Weeks. Equations for determining the gas and brine volumes in sea ice samples. *Journal of Claciology*, 29(102):306–316, 1983. ISSN 0022-1430.
- A. Denoth. The pendular-funicular liquid transition in snow. *Journal of Glaciology*, 5(9):980, 1980.
- M. Drinkwater and G. B. Crocker. Modelling changes in the dielectric and scattering properties of young snow covered sea ice. *Journal of Glaciology*, 34(118), 1988.

- M. R. Drinkwater. LIMEX '87 ice surface characteristics: Implications for C-band SAR backscatter signatures. *IEEE Transactions on Geoscience and Remote Sensing*, 27(5): 501–513, 1989. ISSN 01962892. doi: 10.1109/TGRS.1989.35933.
- S. D. Drobot and M. R. Anderson. An improved method for determining snowmelt onset dates over Arctic sea ice using scanning multichannel microwave radiometer and Special Sensor Microwave/Imager data. *Journal of Geophysical Research*, 106(D20):24033, 2001. ISSN 0148-0227. doi: 10.1029/2000JD000171.
- European Centre for Medium-Range Weather Forecasts. ERA40 Model Resolution Gridded Surface, Vertical Integrals, and Other Single Level Fields from ECMWF, 2004.
- J. A. Fleck, Jr. and M. D. Feit. Beam propagation in uniaxial anisotropic media. *Journal of the Optical Society of America*, 73(7):920, jul 1983. ISSN 0030-3941. doi: 10.1364/JOSA.73.000920.
- J. Font, A. Camps, A. Borges, M. Martín-Neira, J. Boutin, N. Reul, Y. H. Kerr, A. Hahne, and S. Mecklenburg. SMOS: The Challenging Sea Surface Salinity Measurement From Space. *Proceedings of the IEEE*, 98(5):649–665, may 2010. ISSN 0018-9219. doi: 10.1109/JPROC.2009.2033096.
- R. Fuhrhop, T. Grenfell, and G. Heygster. A combined radiative transfer model for sea ice, open ocean, and atmosphere. *Radio Science*, 33(2):303–316, mar 1998. ISSN 00486604. doi: 10.1029/97RS03020.
- K. Golden. Bounds on the complex permittivity of sea ice. *Journal of Geophysical Research*, 100(C7):13699, 1995. ISSN 0148-0227. doi: 10.1029/94JC03007.
- K. Golden and S. Ackley. Modeling of anisotropic electromagnetic reflection from sea ice. *Journal of Geophysical Research: . . .*, 86:8107–8116, 1981.
- K. M. Golden, H. Eicken, a. L. Heaton, J. Miner, D. J. Pringle, and J. Zhu. Thermal evolution of permeability and microstructure in sea ice. *Geophysical Research Letters*, 34(16):2–7, 2007. ISSN 00948276. doi: 10.1029/2007GL030447.
- J. Haapala, M. Lensu, M. Dumont, A. H. H. Renner, M. a. Granskog, and S. Gerland. Small-scale horizontal variability of snow, sea-ice thickness and freeboard in the first-year ice region north of Svalbard. *Annals of Glaciology*, 54(62):261–266, 2013. ISSN 02603055. doi: 10.3189/2013AoG62A157.
- C. Haas, J. Lobach, S. Hendricks, L. Rabenstein, and A. Pfaffling. Helicopter-borne measurements of sea ice thickness, using a small and lightweight, digital EM system. *Journal of Applied Geophysics*, 67(3):234–241, mar 2009. ISSN 09269851. doi: 10.1016/j.jappgeo.2008.05.005.

- G. Heygster, S. Hendricks, L. Kaleschke, N. Maaß, P. Mills, D. Stammer, R. T. Tonboe, and C. Haas. L-Band Radiometry for Sea-Ice Applications. Technical Report November, University of Bremen, 2009.
- G. Heygster, M. Huntemann, and H. Wang. Algorithm Theoretical Basis Document (ATBD) for the University of Bremen Polarization-based SMOS sea ice thickness retrieval algorithm (Algorithm II). Technical Report Algorithm II, Institute of Environmental Physics, Bremen, Germany, 2012.
- G. Heygster, M. Huntemann, N. Ivanova, R. Saldo, and L. T. Pedersen. Response of passive microwave sea ice concentration algorithms to thin ice. In *2014 IEEE Geoscience and Remote Sensing Symposium*, pages 3618–3621. IEEE, jul 2014. ISBN 978-1-4799-5775-0. doi: 10.1109/IGARSS.2014.6947266.
- M. Huntemann and G. Heygster. A New Method to Filter Out Radio-Frequency Interference (RFI) from SMOS Level 1C Data for Sea Ice Applications. In G. Lohmann, H. Meggers, V. Unnithan, D. Wolf-Gladrow, J. Notholt, and A. Bracher, editors, *Towards an Interdisciplinary Approach in Earth System Science*, pages 91–98. Springer International Publishing, 2015. doi: 10.1007/978-3-319-13865-7{_}_}11.
- M. Huntemann, G. Heygster, L. Kaleschke, T. Krumpfen, M. Mäkynen, and M. Drusch. Empirical sea ice thickness retrieval during the freeze-up period from SMOS high incident angle observations. *The Cryosphere*, 8(2):439–451, mar 2014. ISSN 1994-0440. doi: 10.5194/tc-8-439-2014.
- M. Ingham, D. Pringle, and H. Eicken. Cross-borehole resistivity tomography of sea ice. *Cold Regions Science and Technology*, 52(3):263–277, 2008. ISSN 0165232X. doi: 10.1016/j.coldregions.2007.05.002.
- N. Ivanova, L. T. Pedersen, R. T. Tonboe, S. Kern, G. Heygster, T. Lavergne, a. Sørensen, R. Saldo, G. Dybkjær, L. Brucker, and M. Shokr. Satellite passive microwave measurements of sea ice concentration: an optimal algorithm and challenges. *The Cryosphere Discussions*, 9(1):1269–1313, 2015. ISSN 1994-0440. doi: 10.5194/tcd-9-1269-2015.
- Japan Meteorological Agency. JRA-55: Japanese 55-year Reanalysis, Daily 3-Hourly and 6-Hourly Data, 2013.
- K.-P. Johnsen. Radiometrische Messungen im arktischen Ozean - Vergleich von Theorie und Experiment, 1998.
- K. A. Jones, M. Ingham, D. J. Pringle, and H. Eicken. Temporal variations in sea ice resistivity: Resolving anisotropic microstructure through cross-borehole DC resistivity tomography. *Journal of Geophysical Research: Oceans*, 115(11):1–14, 2010. ISSN 21699291. doi: 10.1029/2009JC006049.

- K. A. Jones, M. Ingham, and H. Eicken. Modeling the anisotropic brine microstructure in first-year Arctic sea ice. *Journal of Geophysical Research: Oceans*, 117(2):1–14, 2012. ISSN 21699291. doi: 10.1029/2011JC007607.
- L. Kaleschke, N. Maaß, C. Haas, S. Hendricks, G. Heygster, and R. T. Tonboe. A sea-ice thickness retrieval model for 1.4 GHz radiometry and application to airborne measurements over low salinity sea-ice. *The Cryosphere*, 4(4):583–592, dec 2010. ISSN 1994-0424. doi: 10.5194/tc-4-583-2010.
- L. Kaleschke, X. Tian-Kunze, N. Maaß, M. Mäkynen, and M. Drusch. Sea ice thickness retrieval from SMOS brightness temperatures during the Arctic freeze-up period. *Geophysical Research Letters*, 39(5), mar 2012. ISSN 0094-8276. doi: 10.1029/2012GL050916.
- L. Kaleschke, X. Tian-kunze, N. Maaß, G. Heygster, M. Huntemann, H. Wang, and C. Haas. ESA Support To Science Element (STSE) SMOS Sea Ice Retrieval Study (SMOSIce) Final Report ESA ESTEC Contract No .: 4000101476 / 10 / NL / CT. Technical report, University of Hamburg, 2013.
- E. Källen. HIRLAM Documentation Manual, System 2.5. Technical report, Swed. Meteorol. and Hydrol. Inst, Norrköping, Sweden., 1996.
- E. Kalnay, M. Kanamitsu, R. Kistler, W. Collins, D. Deaven, L. Gandin, M. Iredell, S. Saha, G. White, J. Woollen, Y. Zhu, A. Leetmaa, R. Reynolds, M. Chelliah, W. Ebisuzaki, W. Higgins, J. Janowiak, K. C. Mo, C. Ropelewski, J. Wang, R. Jenne, and D. Joseph. The NCEP/NCAR 40-Year Reanalysis Project. *Bulletin of the American Meteorological Society*, 77(3):437–471, mar 1996. ISSN 0003-0007. doi: 10.1175/1520-0477(1996)077<0437:TNYRP>2.0.CO;2.
- S. Kern, G. Spreen, L. Kaleschke, S. de La Rosa, and G. Heygster. Polynya Signature Simulation Method polynya area in comparison to AMSR-E 89 GHz sea-ice concentrations in the Ross Sea and off the Adélie Coast, Antarctica, for 2002–05: first results. *Annals of Glaciology*, 46(1):409–418, oct 2007. ISSN 02603055. doi: 10.3189/172756407782871585.
- Y. Kerr, P. Waldteufel, J.-P. Wigneron, J. Martinuzzi, J. Font, and M. Berger. Soil moisture retrieval from space: the Soil Moisture and Ocean Salinity (SMOS) mission. *IEEE Transactions on Geoscience and Remote Sensing*, 39(8):1729–1735, 2001. ISSN 01962892. doi: 10.1109/36.942551.
- A. Khazaal and E. Anterrieu. SMOS image reconstruction algorithm: Extension of the band limited approach to the fully-polarimetric mode of MIRAS. In *2009 International Conference on Advances in Computational Tools for Engineering Applications*, pages 180–185. IEEE, jul 2009. ISBN 978-1-4244-3833-4. doi: 10.1109/ACTEA.2009.5227912.

- L. Klein and C. Swift. An improved model for the dielectric constant of sea water at microwave frequencies. *IEEE Transactions on Antennas and Propagation*, 25(1):104–111, jan 1977. ISSN 0096-1973. doi: 10.1109/TAP.1977.1141539.
- P. Knudsen, O. Andersen, L. Stenseng, L. Moreno, P. a. M. Berry, and P. Thibaut. LOTUS — Preparing Land and Ocean Take Up from Sentinel-3. Technical Report August, 2013.
- A. Kovacs. Sea ice. Part 1, Bulk salinity versus ice floe thickness. Technical Report June, U.S. Army Cold Regions Research and Engineering Laboratory, Hanover, N.H., 1996.
- T. Krumpen, S. Hendricks, and C. Haas. Data report on EM-Bird ice thickness measurements for SMOSIce validation obtained during Transdrift XX, ARK XXVII/3 and SafeWin 2011 campaigns. Technical Report January 2012, AWI, 2011.
- N. Kurtz. IceBridge Sea Ice Freeboard, Snow Depth, and Thickness Quick Look, 2012.
- N. T. Kurtz, S. L. Farrell, M. Studinger, N. Galin, J. P. Harbeck, R. Lindsay, V. D. Onana, B. Panzer, and J. G. Sonntag. Sea ice thickness, freeboard, and snow depth products from Operation IceBridge airborne data. *Cryosphere*, 7(4):1035–1056, 2013. ISSN 19940416. doi: 10.5194/tc-7-1035-2013.
- R. Kwok and G. F. Cunningham. ICESat over Arctic sea ice: Estimation of snow depth and ice thickness. *Journal of Geophysical Research*, 113(C8):C08010, aug 2008. ISSN 0148-0227. doi: 10.1029/2008JC004753.
- R. Kwok, J. C. Comiso, S. Martin, and R. Drucker. Ross Sea polynyas: Response of ice concentration retrievals to large areas of thin ice. *Journal of Geophysical Research*, 112(C12), dec 2007. ISSN 0148-0227. doi: 10.1029/2006JC003967.
- J. Launiainen and B. Cheng. Modelling of ice thermodynamics in natural water bodies. *Cold Regions Science and Technology*, 27(3):153–178, jun 1998. ISSN 0165232X. doi: 10.1016/S0165-232X(98)00009-3.
- T. Lavergne, S. Eastwood, Z. Teffah, H. Schyberg, and L.-a. Breivik. Sea ice motion from low-resolution satellite sensors: An alternative method and its validation in the Arctic. *Journal of Geophysical Research*, 115(C10):C10032, oct 2010. ISSN 0148-0227. doi: 10.1029/2009JC005958.
- S. W. Laxon, K. a. Giles, A. L. Ridout, D. J. Wingham, R. Willatt, R. Cullen, R. Kwok, A. Schweiger, J. Zhang, C. Haas, S. Hendricks, R. Krishfield, N. Kurtz, S. Farrell, and M. Davidson. CryoSat-2 estimates of Arctic sea ice thickness and volume. *Geophysical Research Letters*, 40(4):732–737, feb 2013. ISSN 00948276. doi: 10.1002/grl.50193.
- M. Leppäranta. A review of analytical models of sea-ice growth. *Atmosphere-Ocean*, 31(1):123–138, mar 1993. ISSN 0705-5900. doi: 10.1080/07055900.1993.9649465.

- M. Leppäranta and T. Manninen. The brine and gas content of sea ice with attention to low salinities and high temperatures. Technical report, 1988.
- H. Looyenga. Dielectric constants of heterogeneous mixtures. *Physica*, 31(1):401–406, 1965. ISSN 00318914. doi: 10.1016/0031-8914(65)90045-5.
- N. Maaß. *Remote sensing of sea ice thickness using SMOS data*. PhD thesis, Universität Hamburg, 2013.
- N. Maaß, L. Kaleschke, X. Tian-Kunze, and M. Drusch. Snow thickness retrieval over thick Arctic sea ice using SMOS satellite data. *The Cryosphere*, 7(6):1971–1989, dec 2013. ISSN 1994-0424. doi: 10.5194/tc-7-1971-2013.
- N. Maaß, L. Kaleschke, X. Tian-Kunze, and R. T. Tonboe. Snow thickness retrieval from L-band brightness temperatures: a model comparison. *Annals of Glaciology*, 56(69):9–17, 2015a. ISSN 02603055. doi: 10.3189/2015AoG69A886.
- N. Maaß, L. Kaleschke, X. Tian-kunze, M. Mäkynen, M. Drusch, T. Krumpen, S. Hendricks, M. Lensu, J. Haapala, and C. Haas. Validation of SMOS sea ice thickness retrieval in the northern Baltic Sea. *Tellus A*, 67:1–24, feb 2015b. ISSN 1600-0870. doi: 10.3402/tellusa.v67.24617.
- M. Mäkynen, B. Cheng, and M. Similä. On the accuracy of thin-ice thickness retrieval using MODIS thermal imagery over Arctic first-year ice. *Annals of Glaciology*, 54(62):87–96, 2013. ISSN 02603055. doi: 10.3189/2013AoG62A166.
- A. T. Manninen. Surface roughness of Baltic sea ice. *Journal of Geophysical Research*, 102(C1):1119, 1997. ISSN 0148-0227. doi: 10.1029/96JC02991.
- T. Markus, J. C. Stroeve, and J. Miller. Recent changes in Arctic sea ice melt onset, freezeup, and melt season length. *Journal of Geophysical Research: Oceans*, 114(12):1–14, 2009. ISSN 21699291. doi: 10.1029/2009JC005436.
- D. W. Marquardt. An Algorithm for Least-Squares Estimation of Nonlinear Parameters. *Journal of the Society for Industrial and Applied Mathematics*, 11(2):431–441, jun 1963. ISSN 0368-4245. doi: 10.1137/0111030.
- S. Martin. Improvements in the estimates of ice thickness and production in the Chukchi Sea polynyas derived from AMSR-E. *Geophysical Research Letters*, 32(5), mar 2005. ISSN 0094-8276. doi: 10.1029/2004GL022013.
- M. Martín-Neira, S. Ribo, and A. Martín-Polegre. Polarimetric mode of MIRAS. *IEEE Transactions on Geoscience and Remote Sensing*, 40(8):1755–1768, aug 2002. ISSN 0196-2892. doi: 10.1109/TGRS.2002.802489.

- R. A. Massom, H. Eicken, C. Haas, M. O. Jeffries, M. R. Drinkwater, M. Sturm, a. P. Worby, X. R. Wu, V. I. Lytle, S. Ushio, K. Morris, P. a. Reid, S. G. Warren, and I. Allison. Snow on antarctic sea ice. *Reviews of Geophysics*, 39(2000):413–445, 2001. ISSN 8755-1209. doi: 10.1029/2000RG000085.
- C. Matzler. Microwave permittivity of dry snow. *IEEE Transactions on Geoscience and Remote Sensing*, 34(2):573–581, mar 1996. ISSN 01962892. doi: 10.1109/36.485133.
- C. Mätzler. Improved Born approximation for scattering of radiation in a granular medium. *Journal of Applied Physics*, 83(11):6111, 1998. ISSN 00218979. doi: 10.1063/1.367496.
- C. Mätzler. *Thermal Microwave Radiation: Applications For Remote Sensing*. Institution Of Electrical Engineers, 2006.
- C. Mätzler and U. Wegmüller. Dielectric properties of fresh-water ice at microwave frequencies. *Journal of Physics D: Applied Physics*, 20:1623–1630, 1987. ISSN 0022-3727. doi: 10.1088/0022-3727/20/12/013.
- C. Mätzler and A. Wiesmann. Documentation for MEMLS , Version 3 Microwave Emission Model of Layered Snowpacks. (May):1–25, 2012.
- G. A. Maykut and N. Untersteiner. Some results from a time-dependent thermodynamic model of sea ice. *Journal of Geophysical Research*, 76(6):1550–1575, feb 1971. ISSN 01480227. doi: 10.1029/JC076i006p01550.
- J. D. Menashi, K. M. St. Germain, C. T. Swift, J. C. Comiso, and A. W. Lohanick. Low-Frequency Passive-Microwave Observations of Sea Ice in the Weddell Sea. *Journal of Geophysical Research*, 98(C12):22569–22577, dec 1993. ISSN 0148-0227. doi: 10.1029/93JC02058.
- P. Mills and G. Heygster. Retrieving Ice Concentration From SMOS. *IEEE Geoscience and Remote Sensing Letters*, 8(2):283–287, mar 2011a. ISSN 1545-598X. doi: 10.1109/LGRS.2010.2064157.
- P. Mills and G. Heygster. Sea Ice Emissivity Modeling at L-Band and Application to 2007 Pol-Ice Campaign Field Data. *IEEE Transactions on Geoscience and Remote Sensing*, 49(2):612–627, feb 2011b. ISSN 0196-2892. doi: 10.1109/TGRS.2010.2060729.
- M. Nakawo and N. Sinha. Growth rate and salinity profile of first-year sea ice in the high Arctic. *Journal of Glaciology*, 27(I):315–330, 1981.
- S. V. Nghiem, R. Kwok, S. H. Yueh, and M. R. Drinkwater. Polarimetric signatures of sea ice: 2. Experimental observations. *Journal of Geophysical Research*, 100(C7):13681, 1995. ISSN 0148-0227. doi: 10.1029/95JC00938.

- D. Notz and M. G. Worster. In situ measurements of the evolution of young sea ice. *Journal of Geophysical Research*, 113(C3):C03001, mar 2008. ISSN 0148-0227. doi: 10.1029/2007JC004333.
- R. Oliva, E. Daganzo, Y. Kerr, S. Mecklenburg, S. Nieto, P. Richaume, and C. Gruhier. SMOS Radio Frequency Interference Scenario: Status and Actions Taken to Improve the RFI Environment in the 1400–1427-MHz Passive Band. *IEEE Transactions on Geoscience and Remote Sensing*, 50(5):1427–1439, may 2012. ISSN 0196-2892. doi: 10.1109/TGRS.2012.2182775.
- S. J. Orfanidis. *Waves and Antennas Electromagnetic*. 2014.
- J. S. Paterson, B. Brisco, S. Argus, and G. Jones. In Situ Measurements of Micro-Scale Surface Roughness of Sea Ice where :. *Arctic*, 4(June 1990):140–146, 1991.
- C. Petrich and H. Eicken. Growth, Structure and Properties of Sea Ice. In *Sea Ice: Second Edition*, pages 23–77. Wiley-Blackwell, 2010. ISBN 9781405185806. doi: 10.1002/9781444317145.ch2.
- G. Picard, L. Brucker, a. Roy, F. Dupont, M. Fily, a. Royer, and C. Harlow. Simulation of the microwave emission of multi-layered snowpacks using the Dense Media Radiative transfer theory: the DMRT-ML model. *Geoscientific Model Development*, 6(4):1061–1078, 2013. ISSN 1991-9603. doi: 10.5194/gmd-6-1061-2013.
- D. Polder and J. van Santeen. The effective permeability of mixtures of solids. *Physica*, 12(5):257–271, aug 1946. ISSN 00318914. doi: 10.1016/S0031-8914(46)80066-1.
- P. Sakov, F. Counillon, L. Bertino, K. A. Lisæter, P. R. Oke, and A. Korabelv. TOPAZ4: an ocean-sea ice data assimilation system for the North Atlantic and Arctic. *Ocean Science*, 8(4):633–656, aug 2012. ISSN 1812-0792. doi: 10.5194/os-8-633-2012.
- M. Schwank, C. Matzler, A. Wiesmann, U. Wegmuller, J. Pulliainen, J. Lemmetyinen, K. Rautiainen, C. Derksen, P. Toose, and M. Drusch. Snow Density and Ground Permittivity Retrieved from L-Band Radiometry: A Synthetic Analysis. *IEEE Journal of Selected Topics in Applied Earth Observations and Remote Sensing*, pages 1–14, 2015. ISSN 1939-1404. doi: 10.1109/JSTARS.2015.2422998.
- M. Shokr. Field observations and model calculations of dielectric properties of Arctic sea ice in the microwave C-band. *IEEE Transactions on Geoscience and Remote Sensing*, 36(2):463–478, mar 1998. ISSN 01962892. doi: 10.1109/36.662730.
- M. Shokr and N. Sinha. *Sea Ice*. Geophysical Monograph Series. John Wiley & Sons, Inc, Hoboken, NJ, mar 2015. ISBN 9781119028000. doi: 10.1002/9781119028000.

- G. Singh and G. Venkataraman. Snow density estimation using polarimetric ASAR data. In *International Geoscience and Remote Sensing Symposium (IGARSS)*, volume 2, pages 463–466, 2009. ISBN 9781424433957. doi: 10.1109/IGARSS.2009.5418165.
- D. M. Smith. Observation of perennial Arctic sea ice melt and freeze-up using passive microwave data. *Journal of Geophysical Research*, 103(C12):27753, 1998. ISSN 0148-0227. doi: 10.1029/98JC02416.
- G. Spreen, L. Kaleschke, and G. Heygster. Sea ice remote sensing using AMSR-E 89-GHz channels. *Journal of Geophysical Research: Oceans*, 113(2), jan 2008. ISSN 21699291. doi: 10.1029/2005JC003384.
- T. F. Stocker, D. Qin, G.-K. Plattner, M. Tignor, S. K. Allen, J. Boschung, A. Nauels, Y. Xia, V. Bex, and P. M. Midgley. Climate change 2013: The physical science basis. Technical report, 2013. 1535 pp.
- A. Stogryn. Equations for Calculating the Dielectric Constant of Saline Water (Correspondence). *IEEE Transactions on Microwave Theory and Techniques*, 19(8):733–736, aug 1971. ISSN 0018-9480. doi: 10.1109/TMTT.1971.1127617.
- A. Stogryn. An Analysis of the Tensor Dielectric Constant of Sea Ice at Microwave Frequencies. *IEEE Transactions on Geoscience and Remote Sensing*, GE-25(2):147–158, 1987. ISSN 0196-2892. doi: 10.1109/TGRS.1987.289814.
- A. Stogryn and G. Desargant. The dielectric properties of brine in sea ice at microwave frequencies. *IEEE Transactions on Antennas and Propagation*, 33(5):523–532, may 1985. ISSN 0096-1973. doi: 10.1109/TAP.1985.1143610.
- J. Stroeve, T. Markus, J. Maslanik, D. Cavalieri, A. Gasiewski, J. Heinrichs, J. Holmgren, D. Perovich, and M. Sturm. Impact of Surface Roughness on AMSR-E Sea Ice Products. *IEEE Transactions on Geoscience and Remote Sensing*, 44(11):3103–3117, nov 2006. ISSN 0196-2892. doi: 10.1109/TGRS.2006.880619.
- C. Swift, D. Dehority, A. Tanner, and R. McIntosh. Passive Microwave Spectral Emission from Saline Ice at C-Band During the Growth Phase. *IEEE Transactions on Geoscience and Remote Sensing*, GE-24(6):519–529, 1986. ISSN 0196-2892. doi: 10.1109/TGRS.1986.289698.
- T. Tamura, K. I. Ohshima, T. Markus, D. J. Cavalieri, S. Nishashi, and N. Hirasawa. Estimation of Thin Ice Thickness and Detection of Fast Ice from SSM/I Data in the Antarctic Ocean. *Journal of Atmospheric and Oceanic Technology*, 24(10):1757–1772, oct 2007. ISSN 0739-0572. doi: 10.1175/JTECH2113.1.

- D. N. Thomas and G. S. Dieckmann. *Sea Ice*. Wiley-Blackwell, 2009. ISBN 978-1-4051-8580-6.
- A. S. Thorndike, D. A. Rothrock, G. A. Maykut, and R. Colony. The Thickness Distribution of Sea Ice. *Journal of Geophysical Research*, 80(33):4501, 1975. ISSN 0148-0227. doi: 10.1029/JC080i033p04501.
- X. Tian-Kunze, L. Kaleschke, N. Maaß, M. Mäkynen, N. Serra, M. Drusch, and T. Krumpfen. SMOS-derived thin sea ice thickness: Algorithm baseline, product specifications and initial verification. *Cryosphere*, 8(3):997–1018, may 2014. ISSN 19940424. doi: 10.5194/tc-8-997-2014.
- G. Timco and W. Weeks. A review of the engineering properties of sea ice. *Cold Regions Science and Technology*, 60(2):107–129, feb 2010. ISSN 0165232X. doi: 10.1016/j.coldregions.2009.10.003.
- M. Tiuri, A. Sihvola, E. Nyfors, and M. Hallikaiken. The complex dielectric constant of snow at microwave frequencies. *IEEE Journal of Oceanic Engineering*, 9(5):377–382, dec 1984. ISSN 0364-9059. doi: 10.1109/JOE.1984.1145645.
- R. T. Tonboe. Amass and thermodynamic model for sea ice. Technical report, Danish Meteorological Institute, 2005.
- R. T. Tonboe. The simulated sea ice thermal microwave emission at window and sounding frequencies. *Tellus, Series A: Dynamic Meteorology and Oceanography*, 62(3):333–344, may 2010. ISSN 02806495. doi: 10.1111/j.1600-0870.2010.00434.x.
- R. T. Tonboe, G. Dybkjaer, and J. L. HØYER. Simulations of the snow covered sea ice surface temperature and microwave effective temperature. *Tellus A*, 63(5):1028–1037, oct 2011. ISSN 02806495. doi: 10.1111/j.1600-0870.2011.00530.x.
- F. T. Ulaby, R. K. Moore, and A. K. Fung. *Microwave remote sensing: Active and passive. Volume 1 - Microwave remote sensing fundamentals and radiometry*, volume 1. Artech House Publishers, 1981. ISBN 0890061904.
- F. T. Ulaby, R. K. Moore, and A. K. Fung. *Microwave remote sensing: Active and passive. Volume 3 - From theory to applications*, volume 3. Artech House Publishers, 1986. ISBN 0890061920.
- P. Unden, L. Rontu, H. Järvinen, and P. Lynch. HIRLAM-5 scientific documentation, 2002.
- N. Untersteiner. *The Geophysics of Sea Ice*. New York, Plenum Press. (NATO ASI Series B, 146), 1986. ISBN 978-1-4899-5354-4.

- M. R. Vant, R. O. Ramseier, and V. Makios. The complex-dielectric constant of sea ice at frequencies in the range 0.1–40 GHz. *Journal of Applied Physics*, 49(3):1264, 1978. ISSN 00218979. doi: 10.1063/1.325018.
- P. Wadhams. Sea ice thickness distribution in Fram Strait. *Nature*, 305(5930):108–111, sep 1983. ISSN 0028-0836. doi: 10.1038/305108a0.
- P. Wadhams. Sea ice thickness distribution in the Greenland Sea and Eurasian Basin, May 1987. *Journal of Geophysical Research*, 97(C4):5331, 1992. ISSN 0148-0227. doi: 10.1029/91JC03137.
- S. Warren and I. Rigor. Snow depth on Arctic sea ice. *Journal of ...*, pages 1814–1829, 1999. ISSN 15200442. doi: 10.1175/1520-0442(1999)012<1814:SDOASI>2.0.CO;2.
- W. Weeks. *On Sea Ice*. University of Alaska Press, 2010. ISBN 9781602231016.
- A. Wiesmann and C. Mätzler. Microwave emission model of layered snowpacks. *Remote Sensing of Environment*, 70(3):307–316, 1999. ISSN 00344257. doi: 10.1016/S0034-4257(99)00046-2.
- J.-P. Wigneron, Y. Kerr, P. Waldteufel, K. Saleh, M.-J. Escorihuela, P. Richaume, P. Ferrazzoli, P. de Rosnay, R. Gurney, J.-C. Calvet, J. Grant, M. Guglielmetti, B. Hornbuckle, C. Mätzler, T. Pellarin, and M. Schwank. L-band Microwave Emission of the Biosphere (L-MEB) Model: Description and calibration against experimental data sets over crop fields. *Remote Sensing of Environment*, 107(4):639–655, apr 2007. ISSN 00344257. doi: 10.1016/j.rse.2006.10.014.
- T. Wilheit. Radiative Transfer in a Plane Stratified Dielectric. *IEEE Transactions on Geoscience Electronics*, 16(2):138–143, 1978. ISSN 0018-9413. doi: 10.1109/TGE.1978.294577.
- D. P. Winebrenner, J. Bredow, A. K. Fung, M. R. Drinkwater, S. V. Nghiem, A. J. Gow, D. K. Perovich, T. C. Grenfell, H. C. Han, J. A. Kong, J. K. Lee, S. Mudaliar, R. G. Onstott, L. Tsang, and R. D. West. Microwave Sea Ice Signature Modeling. In *Microwave Remote Sensing of Sea Ice*, volume 68, pages 137–175. 1992. ISBN 0-87590-033-X. doi: 10.1029/GM068.
- P. Yeh. Electromagnetic propagation in birefringent layered media. *Journal of the Optical Society of America*, 69(5):742, 1979. ISSN 0030-3941. doi: 10.1364/JOSA.69.000742.
- Y. Yu and D. A. Rothrock. Thin ice thickness from satellite thermal imagery. *Journal of Geophysical Research*, 101(C11):25753–25766, nov 1996. ISSN 0148-0227. doi: 10.1029/96JC02242.

- B. S. Yurchak. Effect of Snow Density Irregularities on Radar Backscatter from a Layered Dry Snow Pack. *Progress In Electromagnetics Research B*, 59(April):181–191, 2014. ISSN 1937-6472. doi: 10.2528/PIERB14022403.
- T. Zhao, J. Shi, R. Bindlish, T. Jackson, Y. Kerr, Q. Cui, Y. Li, and T. Che. Refinement of SMOS multi-angular brightness temperature and its analysis over reference targets. In *2013 IEEE International Geoscience and Remote Sensing Symposium - IGARSS*, pages 49–52. IEEE, jul 2013. ISBN 978-1-4799-1114-1. doi: 10.1109/IGARSS.2013.6721089.
- T. Zhao, J. Shi, R. Bindlish, T. J. Jackson, Y. H. Kerr, M. H. Cosh, Q. Cui, Y. Li, C. Xiong, and T. Che. Refinement of SMOS Multiangular Brightness Temperature Toward Soil Moisture Retrieval and Its Analysis Over Reference Targets. *IEEE Journal of Selected Topics in Applied Earth Observations and Remote Sensing*, 8(2):589–603, feb 2015. ISSN 1939-1404. doi: 10.1109/JSTARS.2014.2336664.
- S. Zine, J. Boutin, P. Waldteufel, J.-L. Vergely, T. Pellarin, and P. Lazure. Issues About Retrieving Sea Surface Salinity in Coastal Areas From SMOS Data. *IEEE Transactions on Geoscience and Remote Sensing*, 45(7):2061–2072, jul 2007. ISSN 0196-2892. doi: 10.1109/TGRS.2007.894934.
- S. Zine, J. Boutin, J. Font, N. Reul, P. Waldteufel, C. Gabarro, J. Tenerelli, F. Petitcolin, J.-L. Vergely, M. Talone, and S. Delwart. Overview of the SMOS Sea Surface Salinity Prototype Processor. *IEEE Transactions on Geoscience and Remote Sensing*, 46(3): 621–645, mar 2008. ISSN 0196-2892. doi: 10.1109/TGRS.2008.915543.

Acknowledgements

Firstly I would like to express my sincere gratitude to my supervisor Dr. Georg Heygster for plenty of fruitful discussions and continuous support of my work. I also want to thank Prof. Dr. Justus Notholt for giving me the opportunity to do my PhD in the Institute für UmweltPhysik (IUP) and Prof. Dr. Peter Lemke for his interest in my work and time to review my thesis as second referee.

I would like to express my gratitude to my PhD committee members, Dr. Georg Heygster, Prof. Dr. Justus Notholt, Prof. Dr. Rüdiger Gerdes, Prof. Dr. Lars Kaleschke, and Dr. Christian Melsheimer for their valuable suggestions and comments on my work.

The interesting discussions and meetings as part of the SMOSice project from the European Space Agency are highly appreciated. In this context I also want to thank Thomas Krumpen, Stefan Hendricks and Marko Mäkynen for providing validation and comparison data.

I also want to thank again Christian Melsheimer for his patience and for the countless discussions on microwave emission modeling among many other topics.

The support and assistance from the colleagues of my research group PHysical Analysis of RemOte Sensing images (PHAROS) at the IUP are highly appreciated.

For the excellent work and providing a solid basis for my research with SMOS and L-band emission, I want to thank my predecessors Huanhuan Wang and Peter Mills.

I want to thank the SMOS-MODE Cost Action for interesting meetings and connecting people across fields connected via the one satellite and especially for financing my research stay in Copenhagen. Special thanks goes to Rasmus Tonboe and the Danish Meteorological Institute (DMI) for hosting my research stay, for introducing me to Microwave Emission Model of Layered Snowpacks (MEMLS) and the energy balance model, and for valuable hints and suggestions regarding my work. Many thanks go also to Leif Toudal for active discussions and data exchange conceptual and textual hints.

For all the nice time, scientific support and widening of my horizon, I want to thank the members of the Earth System Science Research School (ESSReS) graduate School and their driving forces Klaus Grosfeld, Helge Meggers and Stefanie Klebe.

I want to thank my former office mates and colleagues Gopika Suresh and Alexandra Cherkacheva for the nice inspiring time, laughs and support over the last few years.

Proofreading efforts and suggestions from Georg Heygster and Larysa Istomina are highly appreciated.

I am grateful for the funding from the Federal Ministry of Education and Research / Bundesministerium für Bildung und Forschung (BMBF) project Midterm Climate Prognosis/Mittelfristige Klimaprognose (MiKliP) as part of Climate model Validation (ClimVal) project, without this work would not have been possible.

I also want to thank the European Space Agency for launching the unique research

satellite Soil Moisture and Ocean Salinity (SMOS).

The data provision from European Centre for Medium-Range Weather Forecasts (ECMWF) and National Centers for Environmental Prediction (NCEP) is highly appreciated.

Last but not least, I want to thank my family and friends for their support and care over the years of my PhD project.